Universität Hamburg
DER FORSCHUNG | DER LEHRE | DER BILDUNG

FAKULTÄT
FÜR MATHEMATIK, INFORMATIK
UND NATURWISSENSCHAFTEN

Study of Single Boosted Top-Quark Production at the CMS Experiment

MASTERARBEIT IM STUDIENGANG PHYSIK

VORGELEGT VON

CHRISTOPHER MATTHIES

[redacted]

[redacted]

DEZEMBER 2018

BETREUER & GUTACHTER: PROF. DR. JOHANNES HALLER
ZWEITGUTACHTER: DR. ROMAN KOGLER

UNIVERSITÄT HAMBURG – INSTITUT FÜR EXPERIMENTALPHYSIK
ARBEITSGRUPPE TEILCHENPHYSIK & DETEKTOR-ENTWICKLUNG
LURUPER CHAUSSEE 149 – 22761 HAMBURG – DEUTSCHLAND

Für meine Eltern

Kurzfassung

In dieser Masterarbeit (dt. Titel: *Studie zur Produktion geboosteter Einzel-Top-Quarks am CMS-Experiment*) wird eine erste Machbarkeitsstudie zur Messung von Eigenschaften der Produktion einzelner Top-Quarks im kinematischen Bereich hoher Lorentz-Boosts präsentiert. Der analysierte Datensatz, welcher auf Proton-Proton-Kollisionen bei einer Schwerpunktsenergie von 13 TeV basiert, entspricht einer integrierten Luminosität von 35.9 fb^{-1} und wurde vom CMS-Detektor am Large Hadron Collider der Europäischen Organisation für Kernforschung CERN im Jahre 2016 aufgezeichnet.

Es werden differentielle Wirkungsquerschnitte der assoziierten Produktion eines einzelnen Top-Quarks zusammen mit einem W-Boson als Funktion des transversalen Impulses des Top-Quarks in einem Intervall zwischen 200 GeV und 1,2 TeV gemessen. Die vermessenen Endzustände beinhalten Jets sowie ein einzelnes Elektron oder Myon, wobei die hadronische Zerfallsmode des Top-Quarks vorausgesetzt wird. Aufgrund der kollimierten Endzustandstopologie wird das Top-Quark als ein großer Jet rekonstruiert.

Ein multivariates Verfahren wird benutzt, um zwischen dem Signalprozess und dem dominanten Untergrundprozess, Top-Quark-Paarerzeugung, zu unterscheiden. Die jeweiligen Beiträge einzelner Prozesse in zuvor definierten Intervallen des transversalen Impulses des Top-Jet-Kandidaten werden abgeschätzt, indem die simulierte Vorhersage mit einer Maximum-Likelihood-Methode unter Benutzung der Ausgabeverteilungen von Klassifikationsbäumen an Daten angepasst wird. Die differenziellen Wirkungsquerschnitte auf Partonenebene werden mit einer vereinfachten Entfaltungsmethode extrahiert.

Abstract

In this master's thesis, a first feasibility study for the measurement of single top-quark production in the highly Lorentz-boosted kinematic regime is presented. The analysed data set corresponds to an integrated luminosity of 35.9 fb^{-1} and was recorded by the CMS detector at the CERN Large Hadron Collider in the year 2016, using proton-proton collisions at a center-of-mass energy of 13 TeV.

Differential cross sections of single top-quark production in association with a W boson are measured as function of the transverse momentum of the top quark in an interval ranging from 200 GeV up to 1.2 TeV, using the electron+jets and muon+jets final states, presuming that the top quark decays hadronically. Due to the boosted final-state topology, the top quark is reconstructed as one large jet.

A multivariate method is used to discriminate between the signal process and the dominant background, top-quark pair production. In each bin of the transverse momentum of the top-jet candidate, the simulated model is fitted to data according to a maximum-likelihood estimate, utilizing the response distributions of boosted decision trees. In order to extract cross sections on parton level, a simplified bin-by-bin unfolding procedure is employed.

Table of Contents

Conventions

As usual in high-energy physics, the following conventions apply throughout this thesis:

- Natural units defined by $c = \hbar = 1$ may be assumed in the absence of further specification. In this system, the electronvolt (eV) is used as unit of measure and corresponds to the dimension of energy, mass, and momentum. Nevertheless, SI units may be used as well if appropriate in the given context.
- Cross sections are given in the unit barn (b). One barn is equal to an area of 10^{-28} m^2.
- Mathematical expressions apply the rules of Einstein notation. Greek indices exclusively denote four-vector components. Latin letters are used otherwise.
- In Feynman diagrams, time advances from the left-hand to the right-hand side.

Preamble

The Standard Model of particle physics represents the theoretical framework which describes three out of the four known fundamental interactions in nature: Electromagnetism, the strong nuclear interaction, and the weak nuclear interaction. It is formulated as a quantum field theory and unifies the electromagnetic and weak interaction into the electroweak interaction above the Fermi scale. A further unification with the strong interaction is not possible yet. Gravitation is not covered by the Standard Model and is described by the theory of general relativity . Nevertheless, the Standard Model is one of the most successful theories which have been formulated by physicists so far. Throughout its development history, it was able to predict many observations which were later confirmed by experiments, substantiated by astonishing precision.

The Large Hadron Collider (LHC), the most powerful particle collider ever built, has contributed significantly to the validation of the Standard Model, most importantly by delivering the data necessary to observe the Higgs boson in 2012, the last missing piece of the predicted particle content. Although the Standard Model seems to be complete now, there are many motivations for further studies—especially since the theory is indeed not complete as indicated by many observations in nature which cannot be described by the Standard Model. The most prominent examples for these phenomena are the ones which indicate the believed existence of dark matter or dark energy. Therefore, precision tests of the parameters and predictions of the currently established theoretical framework are necessary to gather new intelligence.

One example for measurements which are able to constrain the validity of the Standard Model up to a certain precision are measurements of differential cross sections of physical processes. One possible target for these measurements are the production processes of the top quark, the heaviest known elementary particle, which plays a key role in the electroweak sector of the Standard Model. The top quark was discovered in 1995 at the Tevatron collider as reported by the CDF and D0 detector experiments. In hadronic collisions like at the Tevatron or the LHC, the top quark can be produced either singly via the electroweak interaction or pairwise via the strong interaction. Several differential cross-section measurements of top-quark production have been performed yet, however mainly focussing on pair production. Top-quark pair production has the advantage of being relatively easily discriminated from background processes compared to single top-quark production for which the pair-production mode is the dominant background. The differential measurements which have been performed so far for the single-top-quark production channels are limited to the kinematic regime of low Lorentz boosts, not surpassing a limit of 300 GeV of top-quark transverse momentum. In this analysis, a feasibility study is performed to extent this limit for single top-quark production to higher values, reaching the kinematic regime of high Lorentz boosts. In order to discriminate between the single-top signal and the dominant pair-production background, a multivariate method is chosen. At the end, differential cross sections of W-associated single top-quark production are measured as function of the transverse momentum of the top quark in an interval ranging from 200 GeV to 1200 GeV.

This thesis is organized as follows. In Chapter 1, the theoretical framework of particle physics is presented and the role of the top quark within the Standard Model is outlined. In Chapter 2, the phenomenology of top-quark production in proton-proton collisions as at the LHC is presented in detail, including an overview of the current status of differential cross-section measurements of single top-quark production. In Chapter 3, the experimental setup is described, i. e. the LHC and the Compact Muon Solenoid (CMS) detector which recorded the data set analyzed in this thesis. Chapter 4 gives an overview of the reconstruction methods and identification criteria for objects which emerge from a collision event and produce signals in the detector. In Chapter 5, the first part of the analysis is presented: The selection cuts on the 2016 data set of the CMS detector are presented which are used to enrich the signal process and to define the measurement phase space. In Chapter 6, the multivariate analysis is presented which uses boosted decision trees to discriminate between single-top signal and top-pair background. Chapter 7 represents the third and final part of the analysis which includes the measurement of the differential cross sections. In Chapter 8, a summary of the presented work and a brief outlook are given.

1 The Top Quark in the Context of the Standard Model of Particle Physics

The top quark has been discovered in 1995 by the CDF and D0 detector experiments at the Tevatron proton-antiproton collider at the Fermi National Accelerator Laboratory (Fermilab) [1, 2]. Initially, its existence was predicted by theorists Makoto Kobayashi and Toshihide Maskawa in 1973 [3] in the course of postulating a third generation of elementary matter particles, motivated by its ability to explain the violation of charge-conjugation parity (CP) symmetry in the decay of charged kaons as observed one decade earlier [4]. Today, the top quark is the heaviest known elementary particle—with a mass of about 173 GeV being close to the mass of a tungsten atom—and is embedded into the *Standard Model* (SM) of particle physics [5], a quantum field theory (QFT) [6] describing the composition, structure, and dynamics of matter on most fundamental levels. The development history of QFT and of the SM is reviewed in Ref. 7. The top quark has been one of the last major SM discoveries, previous to the most recent observation of the Higgs boson, the last missing piece in this puzzle, as announced by the ATLAS and CMS detector experiments at the CERN Large Hadron Collider in 2012 [8, 9]. In this chapter, the SM in its current formulation is briefly recapitulated (Sect. 1.1) and the top quark and its associated physics are identified as key elements of the SM and theories beyond (Sect. 1.2).

1.1 Standard Model of Elementary Particle Physics

The quantum-field-theoretical definition of the SM [5] is based on the postulation of the invariance of its Lagrangian density under local gauge transformations of the internal

$$\mathrm{SU}(3)_C \otimes \mathrm{SU}(2)_\mathrm{L} \otimes \mathrm{U}(1)_Y \tag{1.1}$$

symmetry-group product aside from the inevitable invariance w. r. t. the global Poincaré group of special relativity. The techniques of regularization and renormalization [10] are applicable and serve to treat otherwise arising divergences from higher-order loop corrections. This accomplishes a self-coherent theory. An excitation of a quantum wave field represents one entity out of a set of point-like particles (and vice versa) which can in a first step be differentiated by their spin s: *Fermions* ($s = 1/2$) are the actual building blocks of matter, arranged in three generations (Sect. 1.1.1), and obey the Fermi-Dirac statistics and the Pauli principle. Force-carrying *gauge* or *vector bosons* ($s = 1$) mediate the fundamental interactions. One central scalar boson ($s = 0$), the *Higgs boson* (H), completes the particle content. The bosons obey the Bose-Einstein statistics. The product of Lie groups depicted in Expr. 1.1 describes three of the four known fundamental interactions in nature: The strong nuclear interaction, the weak nuclear interaction, and electromagnetism. Gravitation is not covered by the SM[1]. The SM basically splits up into two major parts: Firstly, the *electroweak theory* (EWT) which unifies the electromagnetic and weak interaction, making use of the concept of spontaneous symmetry breaking (SSB) on basis of the Brout-Englert-Higgs (BEH) mechanism (Sect. 1.1.2). And, secondly, *quantum chromodynamics* (QCD) which describes strong interactions (Sect. 1.1.3). Both are non-Abelian gauge theories a. k. a. Yang-Mills theories which permit vector-boson self-interactions.

According to Noether's theorem, a continuous symmetry leads to the conservation of a current associated with a certain physical quantity. In the case of the SM, QCD conserves the color charge C that is exchanged via its vector bosons, the massless *gluons* (g). The Noether charges of EWT are the weak hypercharge Y and the third component of the weak isospin T_3 which are connected via the Gell-Mann-Nishijima formula

$$Y = 2\,(Q - T_3)\,. \tag{1.2}$$

Herein, Q denotes electric charge, the Noether charge within *quantum electrodynamics* (QED), the standalone theory of electromagnetism based on the $U(1)_Q$ group which emerges from EWT after SSB. The vector boson of QED is the massless *photon* (γ). EWT features four gauge fields in total. The electroweak vector bosons which can actually be observed in nature, i. e. after SSB, are, in addition to the already mentioned photon, the massive $W^{\pm}$ and Z bosons.

1.1.1 Three Generations of Matter and Flavour Dynamics

There are twelve different elementary SM fermions which serve as the fundamental constituents of matter, see Tab. 1.1. For each fermion (f), there is an anti-fermion ($\bar{\text{f}}$) with opposite charge properties. A further distinction is made between *quarks* (q) and *leptons*. The latter ones are divided into charged leptons (ℓ) and neutral leptons, called *neutrinos* (ν). Each fermion is assigned to one of the *three generations of matter*, each of which consists of two quarks and two leptons[2]. The lightest charged lepton is the *electron* (e) which is paired with the *electron*

[1] The exclusion of gravitation does not lead to issues with predictions made by the SM for energy scales which are currently surveyed in particle-physics experiments. Quantum-mechanical effects for gravitational interactions are expected to not occur before reaching the Planck scale ($\sim 10^{19}$ GeV). So far, gravitation is described by the also very successful theory of general relativity [11] which is a classical field theory and thus incompatible with the SM. The unification of all four fundamental interactions would yield a *Theory of Everything*.

[2] However, the lepton and the quark component of each generation have no coherence motivated by any aspect of the SM. Furthermore, there is no motivation for the order of the three generations except for sorting them by the masses of the fermions which they consist of. For simplicity however, we stick with the described picture which is commonly used in overviews of the SM like this one here. There are theories beyond the SM which try to establish a connection between both quarks and leptons, e. g. motivated by the seemingly coincidental fact that particles like the proton, which consists of quarks as described in Sect. 1.1.3, and charged leptons like

Table 1.1.: Elementary fermions within the Standard Model. Their masses as well as electric charges Q are given, ordered by the three generations of matter. Particle masses belong to the SM degrees of freedom and must be determined by experiment. Data taken from Ref. 12 except for the top-quark mass which is taken from Ref. 13 (therein given statistical and systematic uncertainties are combined in quadrature). The top quark holds the record for the most precisely determined quark mass. Relative uncertainties on electron and muon mass are in the order of $\sim 10^{-8}$. For neutrino masses which are expected to be non-zero, upper limits are given[3].

Name	*Symbol*	*Q [e]*	*Mass [MeV]*
I. Generation			
Up quark	u	$+2/3$	$2.2^{+0.6}_{-0.4}$
Down quark	d	$-1/3$	$4.7^{+0.5}_{-0.4}$
Electron	e	-1	0.511
Electron neutrino	ν_e	0	$< 2 \times 10^{-6}$
II. Generation			
Charm quark	c	$+2/3$	$(1.28 \pm 0.03) \times 10^3$
Strange quark	s	$-1/3$	96^{+8}_{-4}
Muon	μ	-1	105.7
Muon neutrino	ν_μ	0	< 0.19
III. Generation			
Top quark	t	$+2/3$	$(172.44 \pm 0.48) \times 10^3$
Bottom quark	b	$-1/3$	$\left(4.18^{+0.04}_{-0.03}\right) \times 10^3$
Tau	τ	-1	1776.86 ± 0.12
Tau neutrino	ν_τ	0	< 18.2

neutrino (ν_e). Together with the *up quark* (u) and the *down quark* (d), they build up the first generation. The second and third generation are set up equivalently, where each of the four particles from the first generation has its respective complement. The electron shares most of its properties with the *muon* (μ) and the *tau* (τ); in particular, their electric charge equals -1 given in units of the elementary charge $e \approx 1.602 \times 10^{-19}$ Coulomb [12]. The complements of the electron neutrino are consequently the *muon neutrino* (ν_μ) and the *tau neutrino* (ν_τ), all of them being electrically uncharged. The six quarks carry fractions of the elementary charge. The *up-type* quarks are the up quark itself, the *charm quark* (c), and the *top quark* (t) with electric charges $+2/3e$. Analogously, the *down-type* quarks are the down quark itself, the *strange quark* (s), and the *bottom quark* (b) with electric charges $-1/3e$. Top and bottom quarks are also referred to as *truth* and *beauty* quarks.

the electron have the same absolute value of electric charge.

[3]The SM does not advocate neutrino masses to arise from the BEH mechanism in the same way as for the other fermions. According to observation and measurement of neutrino oscillations, one finds that neutrinos do have mass and, therefore, an explanation is required. Candidates for a corresponding extension of the SM are the seesaw mechanisms [14] which postulate the existence of additional but significantly more massive neutrinos

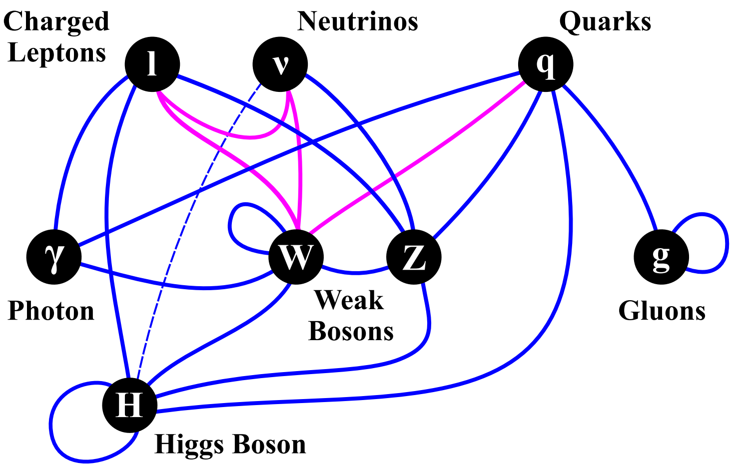

Figure 1.1.: Elementary particle interactions within the Standard Model. Violet lines represent flavour-changing interactions, blue lines all other couplings including vector-boson and Higgs-boson self-interactions. In a strict context, neutrino-Higgs couplings are not supported. Adapted from Ref. 15.

Quarks carry color charge whereas leptons do not. Thus, quarks are the only particles affected by QCD aside from gluons and, hence, the only ones affected by *every* interaction. All possible couplings between fermions and bosons but also the latter ones' self-interactions are depicted in Fig. 1.1. The species of each fermion is referred to as *flavour*. Only the weak interaction is able to change a fermion's flavour via the $W^{\pm}$ bosons which carry $T_3 = \pm 1$ (and $Q = \pm 1$ likewise). All other interactions are flavour-conserving. However, the weak interaction violates parity (P) symmetry, i. e. the possibility of its occurrence depends on the chiral properties of the considered fermions: Only left-handed fermions or right-handed anti-fermions participate and can be arranged in doublets with $T_3 = +1/2$ in each upper and $T_3 = -1/2$ in each lower component. Otherwise, they are arranged in singlets with $T_3 = 0$. For leptons, that is

$$\begin{pmatrix} \nu_e \\ e \end{pmatrix}_L, \quad \begin{pmatrix} \nu_\mu \\ \mu \end{pmatrix}_L, \quad \begin{pmatrix} \nu_\tau \\ \tau \end{pmatrix}_L, \quad \nu_{e,R}, \quad e_R, \quad \nu_{\mu,R}, \quad \mu_R, \quad \nu_{\tau,R}, \quad \tau_R \tag{1.3}$$

and, for quarks,

$$\begin{pmatrix} u \\ d' \end{pmatrix}_L, \quad \begin{pmatrix} c \\ s' \end{pmatrix}_L, \quad \begin{pmatrix} t \\ b' \end{pmatrix}_L, \quad u_R, \quad d_R, \quad c_R, \quad s_R, \quad t_R, \quad b_R. \tag{1.4}$$

For leptons, flavour change is restricted to happen within the same generation, at least according to a strict formulation of the SM[4]. However, up-type quarks are in general permitted to convert to any down-type quark independently from their generation (and vice versa). This phenomenon is called *flavour mixing*. The interaction eigenstates (d′, s′, b′) may emerge as one of the mass

which offset the lighter ones we can currently observe. These theories demand Majorana neutrinos which are their own antiparticle. It is not yet clear whether this is true or they are Dirac particles like all other fermions, with distinguishable matter and antimatter counterparts.

[4]I. e. excluding neutrino oscillations and the consequences which come along with these for charged leptons.

eigenstates (d, s, b). The probability for a certain transition is given by the complex unitary Cabibbo-Kobayashi-Maskawa (CKM) matrix by squaring the absolute value of its respective entry V_{ij}:

$$\begin{pmatrix} \mathrm{d}' \\ \mathrm{s}' \\ \mathrm{b}' \end{pmatrix} = \begin{pmatrix} V_{\mathrm{ud}} & V_{\mathrm{us}} & V_{\mathrm{ub}} \\ V_{\mathrm{cd}} & V_{\mathrm{cs}} & V_{\mathrm{cb}} \\ V_{\mathrm{td}} & V_{\mathrm{ts}} & V_{\mathrm{tb}} \end{pmatrix} \begin{pmatrix} \mathrm{d} \\ \mathrm{s} \\ \mathrm{b} \end{pmatrix}. \tag{1.5}$$

A minimal parametrization of this matrix includes three Euler angles and one complex phase which represents CP violation. Without a third generation, an analogous mixing matrix would not contain such a phase. Since CP violation had been observed, predicting the existence of top and bottom quarks stood to reason. The actual values of the CKM matrix entries are individually determined by different experiments. The results are combined via a global fit, yielding [12]

$$|V_{ij}| = \begin{pmatrix} 0.97434^{+0.00011}_{-0.00012} & 0.22506 \pm 0.00050 & (3.57 \pm 0.15) \times 10^{-3} \\ 0.22492 \pm 0.00050 & 0.97351 \pm 0.00013 & (41.1 \pm 1.3) \times 10^{-3} \\ (8.75^{+0.32}_{-0.33}) \times 10^{-3} & (40.3 \pm 1.3) \times 10^{-3} & 0.99915 \pm 0.00005 \end{pmatrix}. \tag{1.6}$$

1.1.2 Electroweak Symmetry Breaking and the BEH Mechanism

Based on the gauge-symmetry-group product $\mathrm{SU}(2)_\mathrm{L} \otimes \mathrm{U}(1)_Y$, the weak and electromagnetic interaction are unifiable above an energy at which electroweak processes begin to take action. The weak interaction's P violation is depicted by the index "L". The corresponding Fermi scale is commonly said to be equivalent to the vacuum expectation value (VEV) $v = (G_\mathrm{F}\sqrt{2})^{-1/2} \approx$ 246 GeV of the Higgs field (see below) with the Fermi coupling constant (G_F) although it should be understood as a loose benchmark. Starting from the Dirac equation, the electroweak theory introduces four vector fields (W^a_μ where $a \in \{1,2,3\}$ and B_μ) to achieve $\mathrm{SU}(2)_\mathrm{L} \otimes \mathrm{U}(1)_Y$ gauge invariance of its Lagrangian density

$$\mathcal{L}_\mathrm{EW} = -\frac{1}{4}\left(W^{\mu\nu,a} W^a_{\mu\nu} + B^{\mu\nu} B_{\mu\nu}\right) + \sum_\Psi i\,\bar{\Psi}\gamma^\mu \mathcal{D}_\mu \Psi \tag{1.7}$$

by substituting the space-time derivative with a covariant one:

$$\partial_\mu \to \mathcal{D}_\mu = \partial_\mu + \frac{i}{2}\left(g\left\langle \vec{\sigma}_\mathrm{L}, \vec{W}_\mu \right\rangle + g' Y_\Psi B_\mu\right). \tag{1.8}$$

The modified Dirac part of the Lagrangian describes fermion kinetics on the one hand and the coupling between vector bosons and fermions on the other hand. Independently from this, the additional first part of the Lagrangian covers vector-boson kinetics and Yang-Mills self-interactions where the electroweak field strength tensors are given as

$$W^a_{\mu\nu} = \partial_\mu W^a_\nu - \partial_\nu W^a_\mu - g\epsilon^{abc} W^b_\mu W^c_\nu, \qquad B_{\mu\nu} = \partial_\mu B_\nu - \partial_\nu B_\mu. \tag{1.9}$$

Herein, the following notation applies: γ_μ denotes the Dirac matrices, Ψ are the spinors of all SM fermions, $\vec{\sigma}_\mathrm{L}$ are the Pauli matrices which serve as generators of $\mathrm{SU(2)_L}$ but are requested to vanish for right-handed particles; g and g' are the scale-dependent ("running") electroweak coupling constants which are connected via the Weinberg angle $\theta_\mathrm{W}(M_\mathrm{Z}) \approx 28.75°$ [12] by

$$\tan\theta_\mathrm{W} = \frac{g'}{g}. \tag{1.10}$$

The Weinberg angle depicts a rotation related to the symmetry breaking of the electroweak theory. The four vector fields which can actually be observed, i. e. the photon field (A_μ) and the weak bosons' fields (Z_μ and $W_\mu^\pm$), are mixtures of the other vector fields above:

$$W_\mu^\pm = \frac{1}{\sqrt{2}}\left(W_\mu^1 \mp i W_\mu^2\right), \qquad \begin{pmatrix} A_\mu \\ Z_\mu \end{pmatrix} = \begin{pmatrix} \cos\theta_\mathrm{W} & \sin\theta_\mathrm{W} \\ -\sin\theta_\mathrm{W} & \cos\theta_\mathrm{W} \end{pmatrix} \begin{pmatrix} B_\mu \\ W_\mu^3 \end{pmatrix}. \tag{1.11}$$

According to experimental observations, the $\mathrm{W}^\pm$ and Z bosons are massive—in contrast to the photon. This is the predominant reason of their interaction's weakness and also short range which is described by an exponentially decreasing Yukawa potential. The different masses [12]

$$M_\mathrm{W} = 80.379 \pm 0.012\ \mathrm{GeV}, \qquad M_\mathrm{Z} = 91.1876 \pm 0.0021\ \mathrm{GeV} \tag{1.12}$$

are explained by the rotation implied by the Weinberg angle. However, the electroweak Lagrangian density (Expr. 1.7) does not contain any mass terms since they would break gauge invariance. Hence, another mechanism has to exist which introduces surrogate terms.

The BEH mechanism postulates a new T_3-doublet with $Y = +1$ of two complex scalar fields, the Higgs field, which is defined as

$$\phi = \begin{pmatrix} \phi^+ \\ \phi^0 \end{pmatrix} = \frac{1}{\sqrt{2}} \begin{pmatrix} \eta_1 + i\eta_2 \\ \eta_3 + i\eta_4 \end{pmatrix}. \tag{1.13}$$

Subsequently, an additional sector of the Lagrangian density is postulated, reading

$$\mathcal{L}_\mathrm{H} = \left(\mathcal{D}^\mu\phi\right)^\dagger \left(\mathcal{D}_\mu\phi\right) - V(\phi) \tag{1.14}$$

with the electroweak covariant derivative (Expr. 1.8) and with the Higgs potential $V(\phi)$ which consists of a quadratic and a quartic term[5] with the coefficients μ^2 and λ, respectively:

$$V(\phi) = \mu^2\phi^\dagger\phi + \lambda\left(\phi^\dagger\phi\right)^2. \tag{1.15}$$

In case that the mass term is negative ($\mu^2 < 0$), the potential has not a single stable minimum

[5] This ansatz is the only one leading to a consistent theory: Terms of higher order would violate renormalizability and odd terms would yield an asymmetric potential and, thus, an unstable vacuum due to quantum tunnelling.

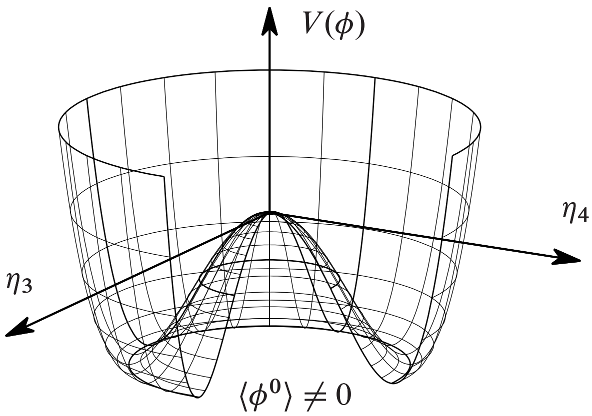

Figure 1.2.: Visualization of the Higgs potential $V(\phi)$ with $\mu^2 < 0$ and $\lambda > 0$. For the sake of simplicity, the Higgs field is reduced to its second component ϕ^0 whose real (η_3) and imaginary (η_4) part span the horizontal plane. The famous shape similar to a Mexican hat is clearly recognizable. In this configuration of its parameters, the local maximum at the origin is not stable but allows for a spontaneously broken symmetry towards a more favourable position in one of the infinitely many local minima: The vacuum is degenerate.

but a continuous set of infinitely many degenerate local minima $\langle\phi\rangle \neq 0$ arranged as a sphere with radius $v = \sqrt{\mu^2/\lambda}$, the VEV, around the origin as shown in Fig. 1.2. One can make an a priori arbitrary choice $\eta_{1,2,4} = 0$ and $\eta_3 = v$ such that the Higgs field can be rewritten like

$$\phi = \frac{1}{\sqrt{2}} \begin{pmatrix} 0 \\ v + H(x) \end{pmatrix} \tag{1.16}$$

where $H(x)$ in addition accounts for excitations around the VEV. The latter field gives rise to the Higgs boson. Once $\mathcal{L}_{\mathrm{H}}$ is written out in full, coupling terms between the scalar Higgs field and the electroweak vector bosons appear where their coefficients define the coupling strength. After SSB, the weak bosons' masses can be read off to be

$$M_{\mathrm{W}} = \frac{1}{2} v g, \qquad M_{\mathrm{Z}} = \frac{1}{2} v \sqrt{g^2 + g'^2}. \tag{1.17}$$

Further, Higgs self-couplings as well as a Higgs-boson mass term ($M_{\mathrm{H}} = \sqrt{-2\mu^2}$) arise. The experimentally established value of the Higgs-boson mass is $M_{\mathrm{H}} = 125.18 \pm 0.16$ GeV [12].

The last missing piece is the introduction of mass terms for fermions. This is done by postulating a third sector of the Lagrangian density, the Yukawa sector, which covers charged leptons and all quarks. Up-type quarks couple to the charge-conjugate Higgs field $\phi_C = -i\sigma_2\phi^*$, the other fermions to the regular one. In the exemplary case of the top quark, the Yukawa term is

$$\mathcal{L}_{\mathrm{Y}}^{(\mathrm{t})} = -g_{\mathrm{Y}}^{(\mathrm{t})} \left(\bar{\Psi}_L \phi_C \mathrm{t}_R + \bar{\mathrm{t}}_R \phi_C^\dagger \Psi_L \right) \tag{1.18}$$

where Ψ_L represents the left-handed T_3-doublet of third-generation quarks and t_R the right-handed top-quark T_3-singlet. The Yukawa coupling constant $g_{\mathrm{Y}}^{(\mathrm{t})}$ contains the top-quark mass

$m_{\rm t} = g_{\rm Y}^{(\rm t)} v/\sqrt{2}$. Since the top quark has by far the largest mass of all SM particles, it has the largest coupling to the Higgs boson and consequently plays a large role in Higgs physics.

1.1.3 Quantum Chromodynamics: The Strong Interaction

The theory of quantum chromodynamics is based on the gauge symmetry group $\mathrm{SU}(3)_C$ which postulates eight vector fields (G^a_μ). They correspond to the strong force carriers, the gluons, which carry color themselves. In equivalence to the electroweak theory, these vector fields are mandatory to achieve $\mathrm{SU}(3)_C$ gauge invariance of the QCD Lagrangian density

$$\mathcal{L}_{\rm QCD} = -\frac{1}{4} G^{\mu\nu,a} G^a_{\mu\nu} + \sum_\Psi i\bar{\Psi}_i \gamma^\mu \mathcal{D}_\mu \delta_{ij} \Psi_j \tag{1.19}$$

where the sum runs over all quark color triplets Ψ_i: The number of color states is equivalent to the dimension of the gauge group. One distinguishes the abstractly named colors red, green, and blue. Anti-quarks carry anti-colors. The QCD covariant derivative is introduced as

$$\partial_\mu \to \mathcal{D}_\mu = \partial_\mu + i g_{\rm s} T^a G^a_\mu. \tag{1.20}$$

Herein, the group generators T^a are the Gell-Mann matrices. These fulfil $[T^a, T^b] = 2if^{abc}T^c$ with the group's structure constant f^{abc}. The gluonic field strength tensors are

$$G^a_{\mu\nu} = \partial_\mu G^a_\nu - \partial_\nu G^a_\mu - g_{\rm s} f^{abc} G^b_\mu G^c_\nu \tag{1.21}$$

whose third term leads to gluon self-interactions, making QCD a Yang-Mills theory.

The strong interaction differs from the electroweak sector of the SM in multiple ways: QCD violates neither P nor CP symmetry according to experimental observations although the theory can be reformulated to contain a corresponding degree of freedom for the latter case. However, the most important disparity consists in its coupling constant ($g_{\rm s}$) which is, firstly, much larger than the electroweak couplings. And, secondly, it shows an inverted running behaviour, or more precisely a logarithmically asymptotic running as shown in Fig. 1.3, what stands in contrast to both electroweak couplings which increase with increasing scale. In approximation, the strong running is described by[6]

$$\alpha_{\rm s}(Q^2) = \frac{g_{\rm s}^2(Q^2)}{4\pi} \propto \frac{1}{\log(Q^2/\Lambda^2)}. \tag{1.22}$$

The currently determined value is $\alpha_{\rm s}(M_{\rm Z}) = 0.1181 \pm 0.0011$ [12]. Herein, Λ estimates a scale which splits the curve in a domain in which perturbation theory is able to describe QCD ($Q > \Lambda$) and another one in which non-perturbative methods must be used ($Q < \Lambda$). This QCD property plays a significant role for predictions made for hadron-collider physics. Phenomenologically,

[6]Within the notational conventions in this thesis, the scale parameter Q is not be confused with electric charge.

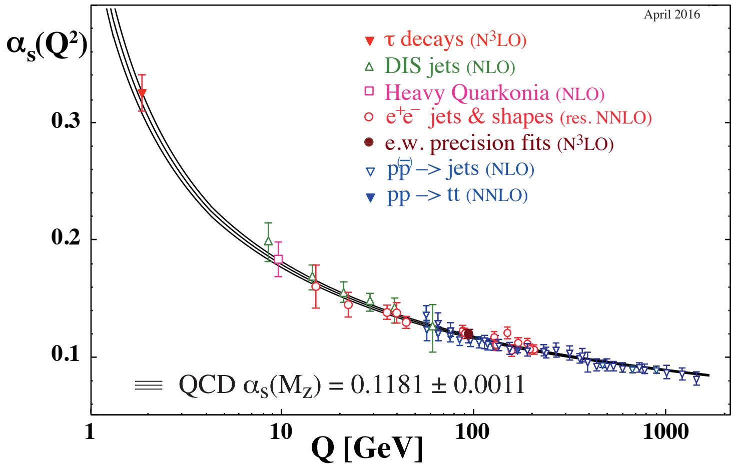

Figure 1.3.: Running of the strong coupling constant. Taken from Ref. 12. The plot shows the predicted curve based on the world average of $\alpha_s(M_Z)$ and includes results from different experimental methods. For each, the perturbative precision (N^nLO) in the α_s-extraction is given. One of the methods is based on analysing top-quark production in proton-proton collisions.

the nature of the strong coupling constant leads to the following observations: Quarks cannot be observed as free particles but obey the principle of *color confinement*, forcing them to bond to other quarks. Bound states of quarks are called hadrons, the corresponding process of hadronic formation is referred to as *hadronization*. Hadrons must be color-singlets (“white”) in total and any isolated color state continues to hadronize until it is completely confined what, e. g., leads to the occurrence of hadronic jets in colliders which emerge from final-state quarks and gluons out of the hard scattering event. Under the perception that larger distances correspond to lower energies, two quarks, which are initially “glued” together but then start to separate, will create a new quark-antiquark pair in between once enough potential energy is in place. However, once they split up, all quarks remain in bound states since each one is able to take a new partner. On the other hand, the strong force between quarks reduces to a nearly vanishing strength at very small distances—they are subject to *asymptotic freedom*.

One distinguishes two kinds of hadrons: Firstly, fermionic *baryons* consisting of three quarks or three anti-quarks with the most prominent representatives being the proton $\mathrm{p} = \{\mathrm{uud}\}$ and the neutron $\mathrm{n} = \{\mathrm{udd}\}$. And, secondly, bosonic *mesons* consisting of one quark and one anti-quark as, for instance, the kaon $\mathrm{K}^+ = \{\mathrm{u\bar{s}}\}$ or the pion $\pi^+ = \{\mathrm{u\bar{d}}\}$. Moreover, highly exotic states like tetra- or pentaquarks are possible and considered to be confirmed [16, 17]. A usual mass scale for hadrons is given by the above QCD scale $\Lambda \approx 200$ MeV. The top quark does not contribute to hadrons since its lifetime ($\sim 5 \times 10^{-25}$ s) is significantly shorter than the usual timescale of hadronization processes ($\sim 10^{-23}$ s $\propto \Lambda^{-1}$) [12]. Thus, top quarks permit unique studies on a “bare” quark. This discussion will be continued in Sect. 2.2.3.

1.2 The Role of Top-Quark Physics within the Theory

So far, we have explored the top quark w. r. t. its position within the theoretical construct of the Standard Model and mentioned its importance for at least some of the branches along the way. To top off this chapter—and to explicitly motivate the work of this thesis from a general viewpoint—, a condensed overview of this particular topic shall be given in this section. For more details, we refer to e. g. Ref. 18, 19.

From the perturbative ansatz of QFT calculations, higher-order radiative correction terms arise. Historically, the Lamb shift is one prominent example for a phenomenon arising from such a correction which was not able to be explained just by the Dirac equation but ultimately by QED. Corrections within the electroweak sector of the SM are dominated by heavy particles, i. e. the top quark and to some extent also the Higgs boson whose masses are in the same order of magnitude as the Fermi scale. They manifest via adjustments made to the W-boson propagator for instance, as shown in Fig. 1.4a. Further, the largest corrections to the Higgs-boson self-energy come from top-quark loops (Fig. 1.4b). In conclusion, the top quark affects crucial SM parameters (and vice versa) since, for instance, the W-boson mass is directly connected to the strength of the weak force (Expr. 1.17). The *hierarchy problem* arises from the fact that gravitation is many orders of magnitude weaker than the interactions incorporated by the SM and, thus, a fundamental relation to top-quark physics is given. The top quark is furthermore the only fermion with a Yukawa coupling $g_{\mathrm{Y}}^{(\mathrm{t})} = \sqrt{2} m_{\mathrm{t}} / v$ (Expr. 1.18) close to unity.

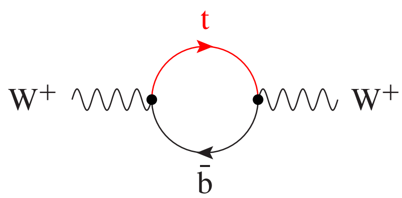

(a) Correction to the W-boson self-energy.

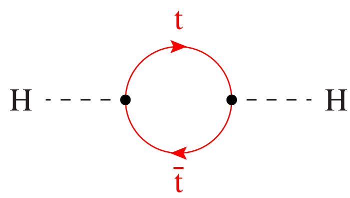

(b) Correction to the Higgs-boson self-energy.

Figure 1.4.: Feynman diagrams representing possible first-order loop corrections from virtual top quarks to the self-energy (i. e. mass) of certain SM particles.

While corrections from heavy particles to the QCD sector are basically negligible, the perturbative corrections within the electroweak sector from the top quark and other particles have measurable effects on the predictions of cross sections, masses, and other quantities—similar to the Lamb shift in QED. Although the mass of the top quark—like all other fermion masses—is a free parameter within the SM, global fits allow to constrain its value together with other SM parameters. An example for a recently published electroweak global fit is shown in Fig. 1.5 in which the consistency of the SM is investigated by examining the correlations between top-quark, Higgs-boson, and W-boson masses. During the preliminary stages of the discovery of the top quark, such fits based on precision measurements at the CERN Large Electron-Positron

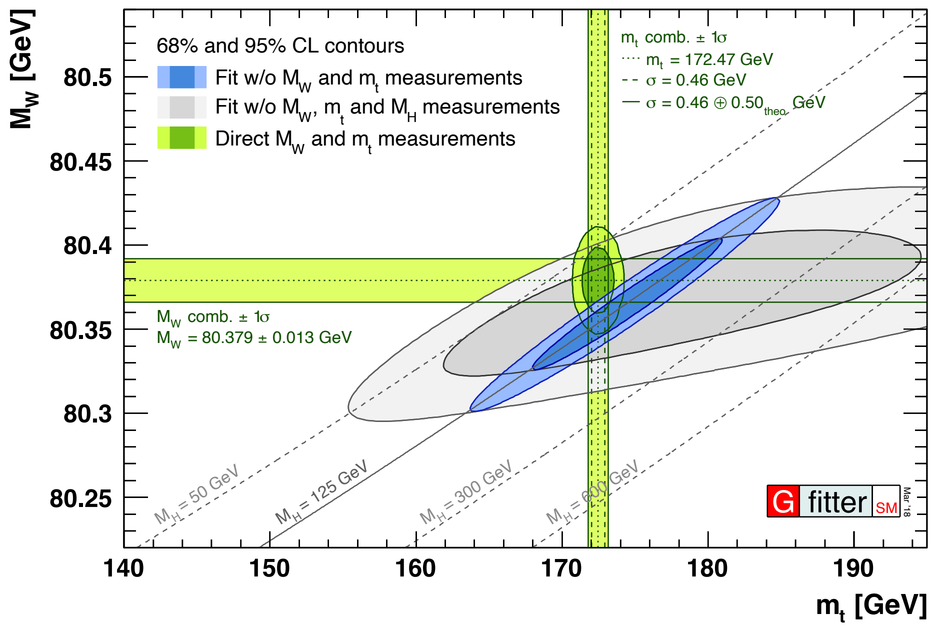

Figure 1.5.: Example for an electroweak global fit. Taken from Ref. 21. Contours at 68 % and 95 % confidence level (CL) are shown for two different fit configurations: One with (blue) and another one without (grey) the results from measurements of the Higgs-boson mass M_{H}, respectively. For comparison, the results from direct measurements of the top-quark mass m_{t} and the W-boson mass M_{W} are shown; they are not included in the fits.

(LEP) collider were able to constrain its mass to $m_{\mathrm{t}} = 173^{+18}_{-20}$ GeV [20] while assuming the not yet known Higgs-boson mass to be in the range of $60 \leq M_{\mathrm{H}}$ [GeV] ≤ 1000.

The pre-discovery estimation of the top-quark mass is a demonstration for how one is able to indirectly constrain particle properties before their actual measurement via direct production of that very particle in experiments. Thus, properties of not yet observed hypothetical particles, which are part of theories beyond the Standard Model (BSM) [22], may be constrained as well, using given SM information. Since the top quark—again due to its high mass—is usually expected by such theories to have large couplings to corresponding BSM particles, detailed investigations of top-quark physics are mandatory. The production of single top quarks—anticipating Sect. 2.2.2—allows precise measurements of the CKM matrix element $|V_{\mathrm{tb}}|$ (cf. Expr. 1.5 and Expr. 1.6) due to its rate being directly proportional to it. When combined with measurements of the other eight CKM matrix elements and results from electroweak precision tests [23, 24], one is able to perform increasingly tight constraints on the potential existence of a fourth generation of matter. In addition, measurements of $|V_{\mathrm{tb}}|$ are able to constrain the possible existence of new heavy vector-like quarks which arise from several minimal extensions of the SM [25]. These constraints complement direct searches for new resonances in mass spectra. Since many new particles from BSM theories are expected to be very heavy, subsequent decays into top quarks would potentially feature boosted final states.

All the discussed points call for precise studies of top-quark physics in general and differential cross-section measurements in particular—like what is presented in this thesis.

Phenomenology of Top-Quark Production in Proton-Proton Collisions

2

The two particle colliders with the ability to produce top quarks in significant amounts were or are the Fermilab Tevatron and the CERN Large Hadron Collider, both using hadronic beam particles with center-of-mass energies $\sqrt{s}$ within the TeV scale. (Anti-)protons, as utilized in both cases, consist of a complex mixture of quarks and gluons, the partons. In the ideal case, a proton-proton collision reduces to a hard scattering between just two partons in which the reduced center-of-mass energy $\sqrt{\hat{s}}$ determines the available physics. Theory calculations allow to make predictions on event cross sections (Sect. 2.1) which correspond to the probability of the occurrence of a specific interaction. There are a handful of possibilities to produce top quarks which will be discussed in this chapter in detail together with the physics of top-quark decays (Sect. 2.2). In case of pair production which has been the discovery channel of the top quark [1, 2], the corresponding $\sqrt{\hat{s}}$ threshold can be expressed via the top-quark mass m_{t} as

$$\hat{s} = x_A x_B s \geq 4m_{\mathrm{t}}^2 \tag{2.1}$$

where $x_{A,B}$ refer to the four-momentum fractions of each parton w. r. t. its host proton. In contrast, the kinematic threshold of single top-quark production, which was observed for the first time in 2009 [26, 27] after first evidence in 2006 [28], individually depends on the considered channel. Single-top production in association with a real W boson ("tW-channel"), the channel which will be analysed in this thesis, corresponds to a threshold of

$$\hat{s} \geq (m_{\mathrm{t}} + M_{\mathrm{W}})^2 \tag{2.2}$$

which is actually lower than for top-quark pair production. But since—among other reasons—the weak force is involved, its cross section is severely smaller at hadron colliders. More details will be discussed in Sect. 2.2.2. A brief overview of a general event topology and associated Monte-Carlo (MC) simulation techniques finalizes this chapter (Sect. 2.3).

2.1 Cross Sections of Hard Scattering Processes

This section is based on Ref. 29 which is an excellent standard reference on QCD and collider physics. Information going beyond the scope of this thesis may be obtained from there.

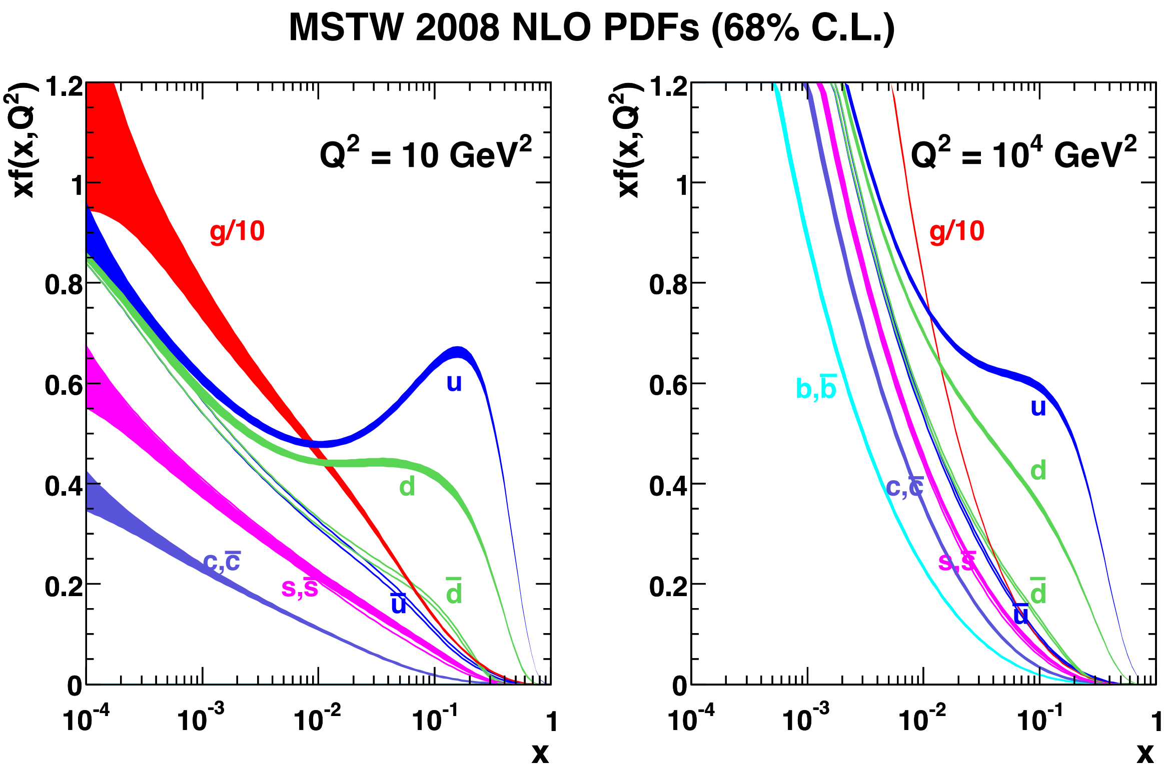

Figure 2.1.: Proton PDFs at next-to-leading order (NLO) for $Q^2 = 10\ \text{GeV}^2$ (left) and $Q^2 = 10^4\ \text{GeV}^2$ (right) as function of the partonic four-momentum fraction x. Quarks and anti-quarks have equal distributions except for u and d quarks due to their presence as sea *and* valence quarks. Gluon PDFs are scaled down by a factor of ten for visibility. Taken from Ref. 30.

Fundamental interactions are illustrated with Feynman diagrams which consist of external lines representing the incoming and outgoing particles of the process, internal propagators transferring momentum between those, and vertices which are proportional to the respective coupling. After translation into a mathematical expression via the Feynman rules, the transition amplitude arises which has to be integrated over the whole phase space, taking into account all possible initial and final states, to get a prediction for the cross section of the process.

In hadron colliders, the initial-state particles of the partonic interaction naturally remain unknown in a particular collision. Therefore, the inner structure of protons has to be understood in the first place: A proton's skeleton consists of two up quarks and one down quark, called *valence quarks*, which are predominantly bound via the strong force. Aside from vacuum fluctuations, the correspondingly present "mesh" of gluons in between permits—alongside of gluon self-interactions—the continuous production and annihilation of virtual quark-antiquark pairs, the *sea quarks*. Sea quarks can be of any flavour but light quarks are significantly more likely to be found than heavy ones. The probability density to find a certain type of parton carrying a specific four-momentum fraction x of its host proton is described by a *parton distribution function* (PDF) $f(x, Q^2)$ which further depends on the considered energy scale Q^2. PDFs can be extracted from deep-inelastic scattering (DIS) experiments, for instance ep $\rightarrow$ e $+ X$ where "X" represents all other event products (i. e. jets and diffractive remnants). Important DIS measurements were performed by, e. g., the ZEUS and H1 collaborations at the ep collider HERA at the Deutsches Elektronen-Synchroton (DESY) in Hamburg, Germany. In recent times, LHC data is used to constrain some of the utilized PDF sets [31] of which one is shown in Fig. 2.1.

Since neither perturbation theory nor non-perturbative approaches like lattice QCD [32] (yet) succeed in describing hadron substructures, one is not able to calculate PDFs directly but relies on the experimental DIS results. However, the Dokshitzer-Gribow-Lipatow-Altarelli-Parisi (DGLAP) QCD evolution functions, which certainly are perturbative, are used to extrapolate PDFs accurately over different energy scales, starting from a certain measured PDF $f(x, Q_0^2)$ at a fixed energy scale Q_0^2 as boundary condition. According to the *factorization theorem*, the inclusive cross section (σ) of a process $AB \to cd + X$ can be written down as

$$\sigma = \sum_{i,j} \iint_0^1 \mathrm{d}x_A \mathrm{d}x_B \, f_{i,A}\left(x_A, \mu_\mathrm{F}^2\right) f_{j,B}\left(x_B, \mu_\mathrm{F}^2\right) \hat{\sigma}\left(ij \to cd, \hat{s}, \mu_\mathrm{R}^2, \mu_\mathrm{F}^2\right) \qquad (2.3)$$

where the sum runs over all types of partons i and j in both colliding hadrons A and B, covering the full PDF combinatorics (gluon-gluon, quark-gluon, and quark-quark); c and d refer to the final-state particles within the hard scattering process, μ_F to the factorization scale describing the energy scale of the considered process, μ_R to the renormalization scale of QCD, and $\hat{\sigma}(\hat{s})$ to the partonic cross section of the hard process $ij \to cd$ which depends on the reduced center-of-mass energy $\sqrt{\hat{s}}$ (Expr. 2.1) and which one is able to calculate to a certain order of perturbative accuracy (N^{n}LO) based on the elements of the scattering matrix ("S-matrix") containing the transition amplitudes. Although not explicitly shown here, the strong coupling constant (α_s, cf. Expr. 1.22) certainly has a large influence on the predictions made since it appears within the DGLAP equations and also many matrix elements, propagating its uncertainty on the results.

2.2 Production and Decay of Top Quarks

The cross sections of top-quark production processes are several orders of magnitude smaller than the total proton-proton collision cross section which is $\sigma(\mathrm{pp} \to X) \approx 1.1 \times 10^{11}$ pb [33] at the LHC at currently $\sqrt{s} = 13$ TeV. In the following, the two main categories of top-quark production at hadron colliders are discussed: Pair production via strong interactions (Sect. 2.2.1) and single production via weak interactions (Sect. 2.2.2). Subsequently, the decay of top quarks is discussed (Sect. 2.2.3). At last, a brief overview on the status of differential cross-section measurements of top-quark production is given (Sect. 2.2.4).

2.2.1 Top-Quark Pair Production via Strong Interactions

Top quarks at the LHC are dominantly produced in pairs via the flavour-conserving strong interaction. The production of top-quark pairs via other processes like electroweak neutral currents or even Higgs-boson propagators is also possible in general but their contribution is negligible.

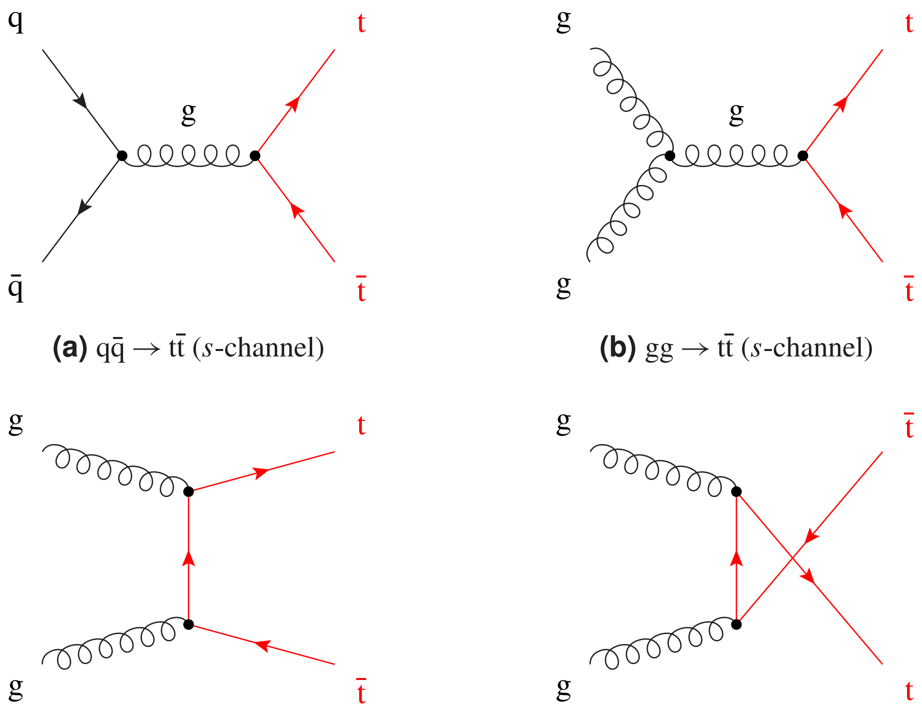

(a) $q\bar{q} \to t\bar{t}$ (s-channel) **(b)** $gg \to t\bar{t}$ (s-channel)

(c) $gg \to t\bar{t}$ (t-channel) **(d)** $gg \to t\bar{t}$ (u-channel)

Figure 2.2.: Leading-order processes of top-quark pair production via the strong force.

All possible leading-order (LO) Feynman diagrams of top-quark production—further classified by the corresponding Mandelstam variable—via either strong quark-antiquark annihilation ($q\bar{q} \to t\bar{t}$; s-channel only) or gluon-gluon fusion ($gg \to t\bar{t}$; s-, t-, and u-channel) are shown in Fig. 2.2. At the Tevatron, quark-antiquark annihilation has been the predominant production channel with about an 85 % contribution due to the availability of valence quarks and valence anti-quarks. However, the circumstances are reversed at the LHC since anti-quarks are just available as virtual particles with correspondingly suppressed PDFs. Furthermore, the probability of finding two gluons with sufficiently large momenta for top-quark pair production is significantly larger at the LHC ($\sqrt{s} \geq 7$ TeV) compared to the Tevatron ($\sqrt{s} \leq 1.96$ TeV) due to the superior center-of-mass energy. At $\sqrt{s} = 7$ TeV (14 TeV) in proton-proton collisions, the ratio is calculated to be around 20 % (10 %) for $q\bar{q} \to t\bar{t}$ and 80 % (90 %) for $gg \to t\bar{t}$ [12].

The most common next-to-leading-order (NLO) processes for top-quark pair production include final-state radiation (FSR) and initial-state radiation (ISR), i. e. the emission of secondary gluons. Another relevant type of NLO process features one gluon and one arbitrary quark in the initial state, representing a variation of the LO t-channel where this particular non-top quark catalyses the interaction by providing another gluon ($gq \to t\bar{t}q$). The emission of a third gluon from the intermediate top-quark propagator in the t- or u-channel is also possible for instance. Beyond these examples which are referred to as "$t\bar{t}$+jets", pair production in assocation with electroweak vector bosons ($t\bar{t}V$ where $V \in \{\gamma, Z, W\}$) [34, 35] has been observed. Searches for double pairs ($t\bar{t}t\bar{t}$ via e. g. gluon-gluon splitting) exist [36]. A recent milestone has been the ob-

Table 2.1.: Theoretical cross sections of $\mathrm{t\bar{t}}$ production (in units of pb). Taken from Ref. 39. They are calculated with the TOP++2.0 program [40] to NNLO+NNLL order, assuming a top-quark mass $m_{\mathrm{t}} = 172.5$ GeV, for different $\sqrt{s}$ in pp collisions. The first uncertainty comes from the independent variation of the factorization (μ_{F}) and renormalization scales (μ_{R}) while the second one is associated to variations in PDFs and α_{s}, following the PDF4LHC prescription with the MSTW2008 NNLO (68 % CL), CT10 NNLO (68 % CL), and NNPDF2.3 (5f FFN) PDF sets [41–44]. The third uncertainty comes from variations (± 1.0 GeV) of the top mass.

LHC setup	*Central value*	*Scale uncert.*	*PDF $\oplus$ α_s uncert.*	*Top-mass uncert.*
pp @ $\sqrt{s} = 7$ TeV	177.31	$+4.56/-5.99$	± 9.02	$+5.44/-5.26$
pp @ $\sqrt{s} = 8$ TeV	252.89	$+6.39/-8.64$	± 11.67	$+7.58/-7.33$
pp @ $\sqrt{s} = 13$ TeV	831.76	$+19.77/-29.20$	± 35.06	$+23.18/-22.45$
pp @ $\sqrt{s} = 14$ TeV	984.50	$+23.21/-34.69$	± 41.31	$+27.14/-26.29$

servation of the production of top-quark pairs in association with a Higgs boson ($\mathrm{t\bar{t}H}$) [37, 38], directly probing the Yukawa interaction (Expr. 1.18) for the very first time, validating the SM once again.

Predicted pair-production cross sections in proton-proton collisions depending on the center-of-mass energy are given in Tab. 2.1, calculated to next-to-next-to-leading order (NNLO) in perturbative QCD, also including soft-gluon resummation to next-to-next-to-leading-logarithmic (NNLL) order. MC $\mathrm{t\bar{t}}$ samples used in this thesis are scaled to the prediction for $\sqrt{s} = 13$ TeV.

2.2.2 Single Top-Quark Production via Weak Interactions

In contrast to pairs of top quarks which can in general be produced via all three fundamental interactions, single top or anti-top quarks are exclusively produced via flavour-changing weak processes. A theoretical review on single-top-quark physics can be found in Ref. 45. There are three "canonical" production channels for single top quarks, as presented in Fig. 2.3, which can be differentiated by the virtuality of the involved W boson [46]: Single-top t-channel and s-channel production, featuring intermediate W propagators, as well as single-top production in association with a real W boson ("tW-channel"). Fig. 2.4 gives an overview over all currently available measurements of inclusive single-top production cross sections versus center-of-mass energy (as of March 2018). A recent breakthrough has been the observation of single top quarks in association with a Z boson [47, 48]. Despite being shown in Fig. 2.4, Z-associated production is a NLO variant (only observed in the t-channel so far, known as tZq) and thus does not count towards the canonical channels. In this section, the canonical channels are presented in more detail individually. Predictions for their cross sections in pp collisions at $\sqrt{s} = 13$ TeV are given in Tab. 2.2 which the corresponding MC samples in this thesis are scaled to.

***t*-channel production.** In the LO process (Fig. 2.3a), a sea b quark and an arbitrary light-flavour quark or anti-quark from the valence or sea pool exchange an intermediate W boson,

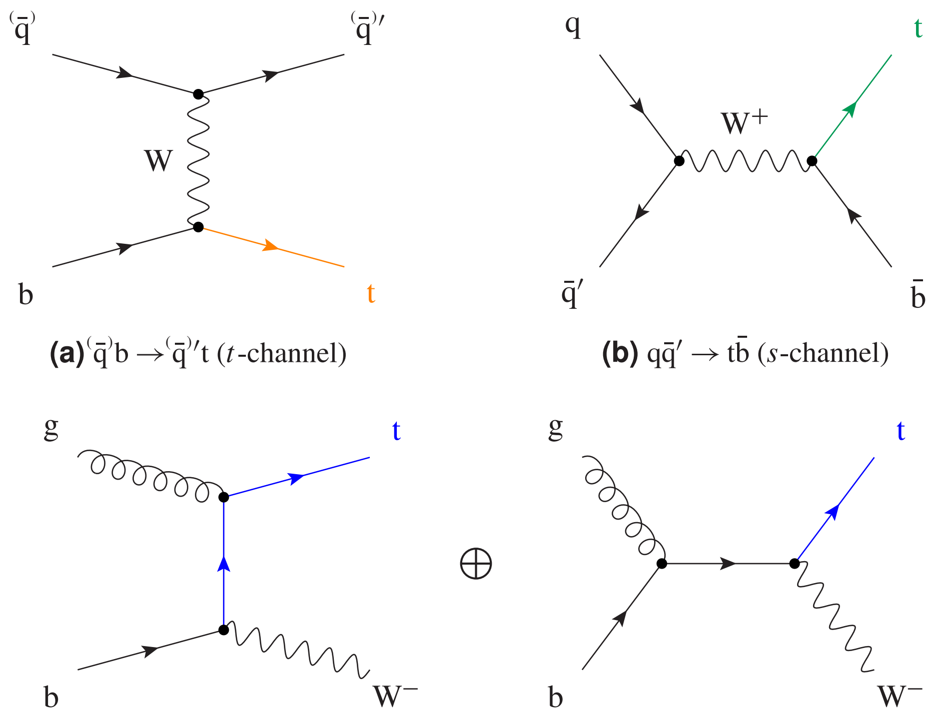

(a) $\overset{(-)}{q}b \to \overset{(-)}{q}'t$ (t-channel) **(b)** $q\bar{q}' \to t\bar{b}$ (s-channel)

(c) $gb \to tW^-$ (t- or s-channel W-associated production a. k. a. "tW-channel")

Figure 2.3.: Leading-order canonical production channels for single top quarks via the weak force. Despite not being shown here, equivalent diagrams hold for single anti-top quarks.

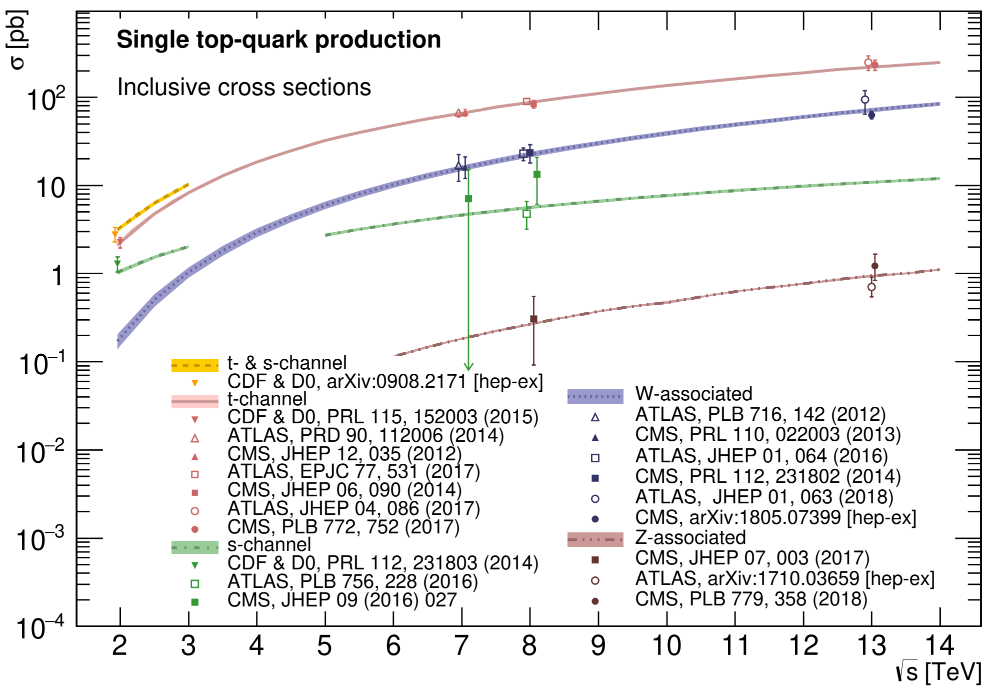

Figure 2.4.: Summary of inclusive-cross-section measurements of single top-quark production at the Tevatron and LHC detector experiments as of March 2018. Taken from Ref. 49. The measurements are compared to theory curves based on NLO QCD complemented with NNLL resummation, calculated as in Ref. 50–52 for the three canonical channels and with aMC@NLO (v.254) [53] for tZq production. The curves for s-channel and the sum of s- and t-channel are calculated for $p\bar{p}$ collisions up to 3 TeV and for pp collisions beyond; for t-channel, tW, and tZq, the curves for pp and $p\bar{p}$ coincide at the considered accuracy.

Table 2.2.: Theoretical cross sections of single top-quark production (in units of pb) for pp collisions at $\sqrt{s} = 13$ TeV. Taken from Ref. 54. Calculations for t- and s-channel were performed at NLO with the HATHOR (v2.1) program [55, 56] using the same PDF sets as given in Tab. 2.1 and covering the same uncertainties, following the PDF4LHC prescription [41]. For tW production, the results of approximate NNLO calculations, using the MSTW2008 NNLO (90 % CL) PDF sets, are given [51, 57] and the second uncertainty is just due to PDFs, excluding α_s.

Mode (pp @ 13 TeV)	*Central value*	*Scale uncert.*	*PDF $\oplus\, \alpha_s$ uncert.*	*Top-mass uncert.*
t-channel ($m_t = 172.5$ GeV)				
top (t)	136.02	$+4.09/-2.92$	± 3.52	± 1.11
anti-top ($\bar{t}$)	80.95	$+2.53/-1.71$	± 3.18	$+0.71/-0.70$
combined ($t+\bar{t}$)	216.99	$+6.62/-4.64$	± 6.16	± 1.81
s-channel ($m_t = 172.5$ GeV)				
top (t)	6.35	$+0.18/-0.15$	± 0.14	$+0.14/-0.13$
anti-top ($\bar{t}$)	3.97	$+0.11/-0.09$	± 0.15	± 0.09
combined ($t+\bar{t}$)	10.32	$+0.29/-0.24$	± 0.27	$+0.23/-0.22$
W-associated ($m_t = 173$ GeV)				
top, anti-top (t, $\bar{t}$)	35.6	± 0.9	± 1.7 (PDF-only)	N/A
combined ($t+\bar{t}$)	71.2	± 1.8	± 3.4 (PDF-only)	N/A

resulting in the production of a top quark. However, b-PDFs are quite small compared to other light-flavour PDFs. Hence, the t-channel is governed by its NLO variant, a $2 \to 3$ process, with one gluon in the initial state that splits into a $b\bar{b}$ pair. One of these two b quarks subsequently scatters weakly with the light quark and transforms into the top quark. This particular process is referred to as "W-gluon fusion" (Fig. 2.5a). The secondary $\bar{b}$ quark is referred to as spectator quark and is preferably scattered into the forward region, the light quark likewise. Other relevant NLO processes include e. g. FSR and ISR (Fig. 2.5b).

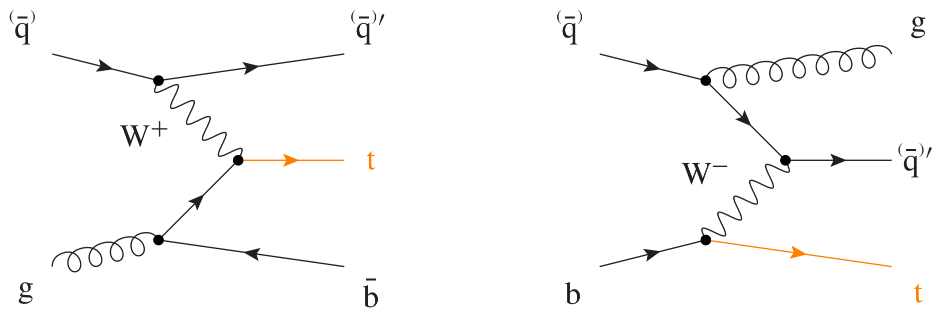

(a) W-gluon fusion **(b)** t-channel featuring ISR

Figure 2.5.: Examples for NLO processes of single top-quark t-channel production.

The t-channel has been the predominant single top-quark production channel at the Tevatron and still is at the LHC with cross sections being one quarter or so of $t\bar{t}$ production. Although single top-quark production is generally suppressed by the weak interaction and also b-PDFs, the t-channel itself is enhanced due to the fact that it scales with $1/M_\mathrm{W}^2$ instead of $1/\hat{s}$ as in $\mathrm{t\bar{t}}$ or s-channel production [58]. At the Tevatron, cross sections for t-channel anti-top and top events are expected to be the same. At the LHC however, bias towards slight suppression of anti-top t-channel production exists due to the asymmetry between quark and anti-quark PDFs in pp collisions compared to $\mathrm{p\bar{p}}$ collisions.

***s*-channel production.** An up-type quark and a down-type anti-quark annihilate into a highly virtual time-like W^+ boson that subsequently decays into a top quark and $\mathrm{\bar{b}}$ quark (Fig. 2.3b). Relevant NLO processes again feature ISR and FSR (Fig. 2.6a) but also the production of at least one of the incoming quarks from gluon splitting (Fig. 2.6b), leading to the presence of an additional final-state quark. At both the LHC and Tevatron, the s-channel is highly suppressed due to the asymmetry between the PDFs of up-type and down-type quarks, resulting from unequal numbers of valence u and d quarks in (anti-)protons. At the LHC only, the asymmetry between quark and anti-quark PDFs belongs to the most limiting factors despite the possibility of NLO quark-gluon fusion and leads to the preferred production of top quarks over anti-top quarks as in the single-top t-channel.

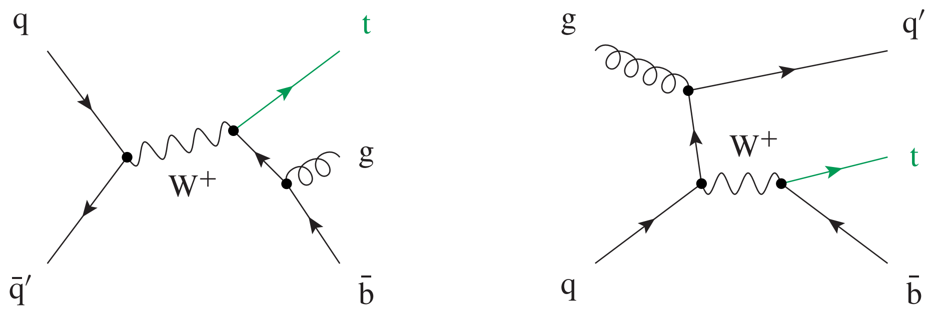

(a) s-channel featuring FSR **(b)** $\mathrm{qg} \to \mathrm{q'}\mathrm{t\bar{b}}$

Figure 2.6.: Examples for NLO processes of single top-quark s-channel production.

W-associated production. This is the signal channel of this thesis' analysis. Like in the single-top t-channel, a sea b quark is found in the initial state, suppressing this channel as well. The b quark scatters with a gluon to produce a top quark and a real or close-to-real W boson, involving an internal quark propagator and being realized as either t- or s-channel (Fig. 2.3c). At the LHC and the Tevatron, there are equal contributions from W-associated top and anti-top production since the above mentioned PDF asymmetries have no effect. It has the second-largest inclusive cross section of all single-top-quark production channels at the LHC. Its first observation succeeded in 2012 [59]. At the Tevatron, tW has not been observed due to its cross section being too small at the corresponding center-of-mass energy and the recorded data sets not being large enough to deliver the necessary statistics.

Relevant NLO processes are the emission of a secondary gluon from the internal quark propagator (in addition to ISR and FSR) or the production of the incoming b quark from gluon

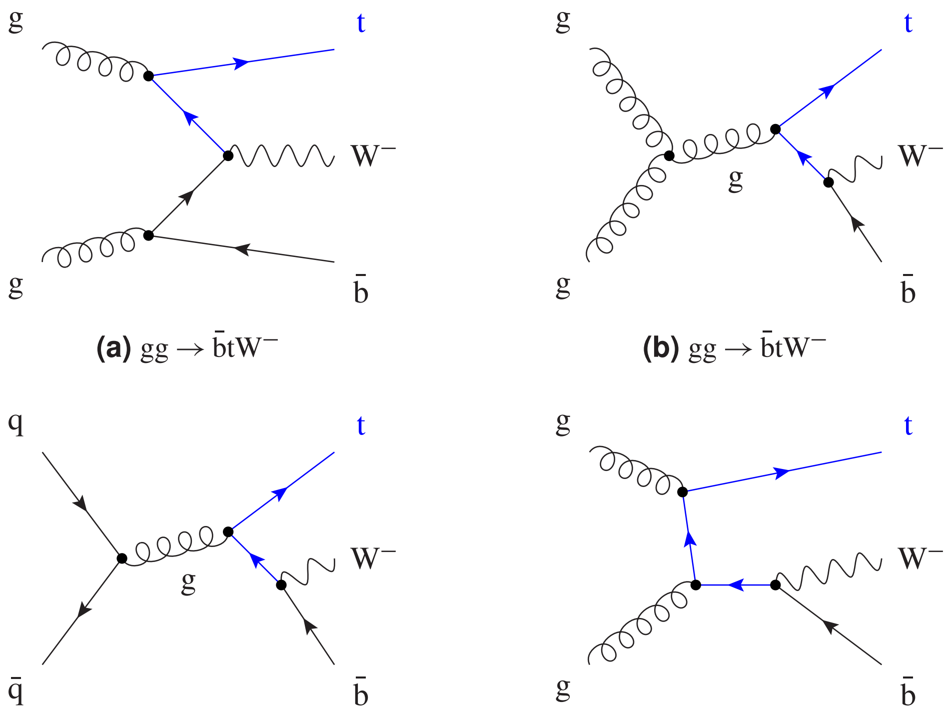

(a) $gg \to \bar{b}tW^-$ **(b)** $gg \to \bar{b}tW^-$

(c) $q\bar{q} \to \bar{b}tW^-$ **(d)** $gg \to \bar{b}tW^-$

Figure 2.7.: Examples for NLO processes of W-associated single top-quark production.

splitting, leading to the presence of a spectator $\bar{b}$ quark in the final state (Fig. 2.7a). However, the most important NLO processes are gluon-gluon fusion (Fig. 2.7b, 2.7d) and quark-antiquark annihilation (Fig. 2.7c) which are similar to $t\bar{t}$ production (Fig. 2.2) but with one top quark from the produced pair being virtual and decaying to a $\bar{b}$ quark and the associated W boson. These NLO contributions lead to non-negligible interferences with $t\bar{t}$ production and make it harder to define tW production as an independent process, especially when the second top quark is close to its mass shell.

As a consequence, LO $t\bar{t}$ production is an irreducible background in collision data since both sets of diagrams feature the same final state ($b\bar{b}W^-W^+$), here taking into account the subsequent decays of all top quarks into b quarks and W bosons. This issue has been studied in Ref. 60, giving recommendations on suitable cuts to define tW as independent process and on how to deal with the interferences in simulation. For simulation of tW, two methods exist: Diagram removal (DR) and diagram subtraction (DS). In the DR method, the interference diagrams in Fig. 2.7 are removed from the NLO cross-section calculation of tW production. In calculations with the DS method, a subtraction term is introduced to cancel out the $t\bar{t}$ contributions. Both methods yield the same event rate and kinematic distributions within scale uncertainties.

2.2.3 Physics of Top-Quark Decays

Due to its very high mass of $172.44 \pm 0.13\,(\text{stat.}) \pm 0.47\,(\text{syst.})$ GeV [13], the top quark opens up a large phase space for decays. It is the only quark with the ability to decay into a real W boson and a b quark, without being hindered to do so by the also large but here smaller mass of the W boson of approximately 80.3 GeV [12]. In general, the top quark is not restricted to decay into a b quark only. However, the contributions from decays into d and s quarks are highly suppressed by the corresponding CKM matrix elements $|V_{\mathrm{td}}|$ and $|V_{\mathrm{ts}}|$ whereas $|V_{\mathrm{tb}}| = 0.99915 \pm 0.00005$ [12] is close to unity (Expr. 1.5 and Expr. 1.6); contributions from light-quark decays are in the order of one part per million and thus negligible.

Neglecting higher-order corrections from EWT and also quadratic terms, the top-quark width at NLO precision is calculated to be [61]

$$\Gamma_{\mathrm{t}} = \frac{G_{\mathrm{F}} m_{\mathrm{t}}^3}{8\pi\sqrt{2}} \left(1 - \frac{M_{\mathrm{W}}^2}{m_{\mathrm{t}}^2}\right)^2 \left(1 + 2\frac{M_{\mathrm{W}}^2}{m_{\mathrm{t}}^2}\right) \left(1 - \frac{2\alpha_{\mathrm{s}}}{3\pi}\left(\frac{2\pi^2}{3} - \frac{5}{2}\right)\right) \tag{2.4}$$

where m_{t} refers to the top-quark pole mass. Assuming $m_{\mathrm{t}} = 173.3$ GeV and $\alpha_{\mathrm{s}}(M_{\mathrm{Z}}) = 0.118$, the top-quark decay width is calculated to be

$$\Gamma_{\mathrm{t}} \approx 1.35\ \mathrm{GeV} \tag{2.5}$$

where larger values of the top-quark mass increase this value. Correspondingly, the top-quark lifetime has a very short value of

$$\tau_{\mathrm{t}} = \frac{1}{\Gamma_{\mathrm{t}}} \approx 5 \times 10^{-25}\ \mathrm{s}. \tag{2.6}$$

The usual time scale of other interactions is much larger, so that the top quark can decay in most cases without their interference. As presented in Sect. 1.1.3, top quarks are thus not affected by hadronization, i. e. no $\mathrm{t\bar{t}}$ quarkonium states or other top-flavoured hadrons exist. Furthermore, QCD fragmentation effects are suppressed what allows for unique studies on “bare” quarks. In case of single top-quark production for instance, measurements of the top-quark spin polarization are possible. In pair production, only spin correlations can be measured.

Since the W boson coming from the top-quark decay is on or very close to its mass shell, it cannot decay into another top quark due to the latter one’s higher mass. All other fermions are eligible to contribute as decay products of real W bosons. Decays into quarks are referred to as *hadronic* decays. Taking into account that quarks come as color triplets, the branching fractions of hadronic and leptonic W^- decays are $\sum \mathcal{B}(\mathrm{W}^- \to \mathrm{q\bar{q}'}) \approx 67\ \%$ and $\mathcal{B}(\mathrm{W}^- \to \ell^- \bar{\nu}_\ell) \approx 11\ \%$, respectively (and similar for W^+) [12]. Since both $\mathrm{t\bar{t}}$ and tW production respectively feature two real W bosons in their final state (always one W^- and one W^+), they share the same naming conventions for their decay channels. An overview of the combinatoric possibilities is given in Fig. 2.8. Using the W-decay branching fractions, one can calculate the individual contributions:

- $\mathrm{W^+W^-} \to \mathrm{q\bar{q}'q''\bar{q}'''}$: *Fully hadronic* decay with $\sim 45.7\ \%$.
- $\mathrm{W^+W^-} \to \mathrm{q\bar{q}'}\ell^-\bar{\nu}_\ell$ and $\mathrm{W^+W^-} \to \ell^+\nu_\ell \mathrm{q''\bar{q}'''}$: *Semileptonic* decay with $\sim 43.8\ \%$.

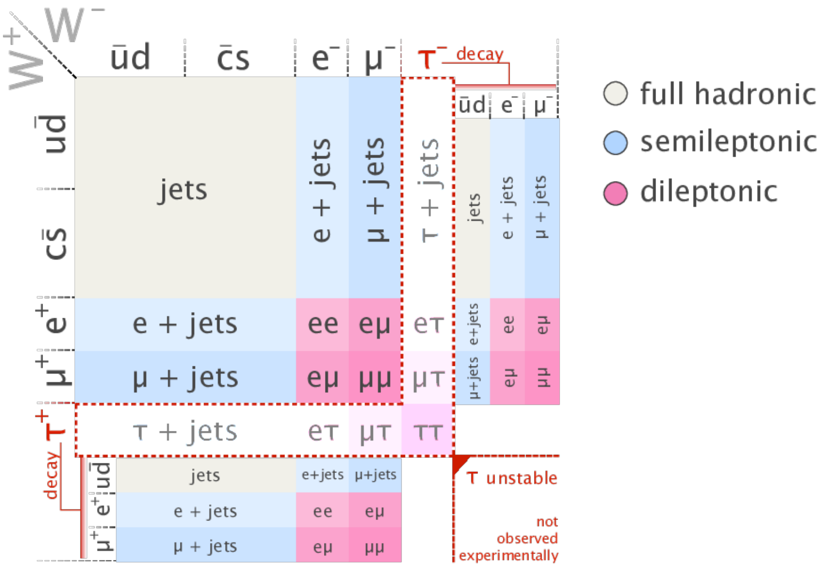

Figure 2.8.: Decay channels of top-quark pair and tW production. Taken from Ref. 62.

- $W^+W^- \to \ell^+\nu_\ell\ell'^-\bar{\nu}_{\ell'}$: *Dileptonic* decay with ~ 10.5 %.

The quarks in the final state evolve into jets of hadrons; therefore, the fully hadronic channel is referred to as "all-jets" in experiments and the semileptonic channel as "ℓ+jets". However, experimentalists further distinguish between e/μ+jets and decays involving τ leptons: Since τ leptons have a very short lifetime, they decay into further particles before reaching the detector, making their reconstruction more complicated.

The physics of top-quark decays of course does not change under Lorentz boosts. However, the reconstruction of top quarks and their corresponding particle jets in detectors is different compared to decays in rest or close to rest. This topic—which is of particular importance for this thesis—is addressed in Sect. 4.5.2.

2.2.4 Differential Cross-Section Measurements

There are several differential cross-section measurements of top-quark production as function of certain kinematic variables available. Both the ATLAS and CMS collaboration present results for differential measurements of top-quark pair and single production in proton-proton collisions. Most of these measurements are however measurements of $t\bar{t}$ production since its study is in general more promising due to the fact that it can be separated from its backgrounds more efficiently. On the other hand, single-top measurements are affected by large $t\bar{t}$ backgrounds what usually requires the application of multivariate algorithms to optimize the signal-background discrimination. Nevertheless, the study of single top-quark production is, due to increasing performance of the LHC detectors and increasingly large data sets, at the point of entering its precision era. A complete overview of all available differential and inclusive cross-section measurements of top-quark pair and single production as of November 2018 can be

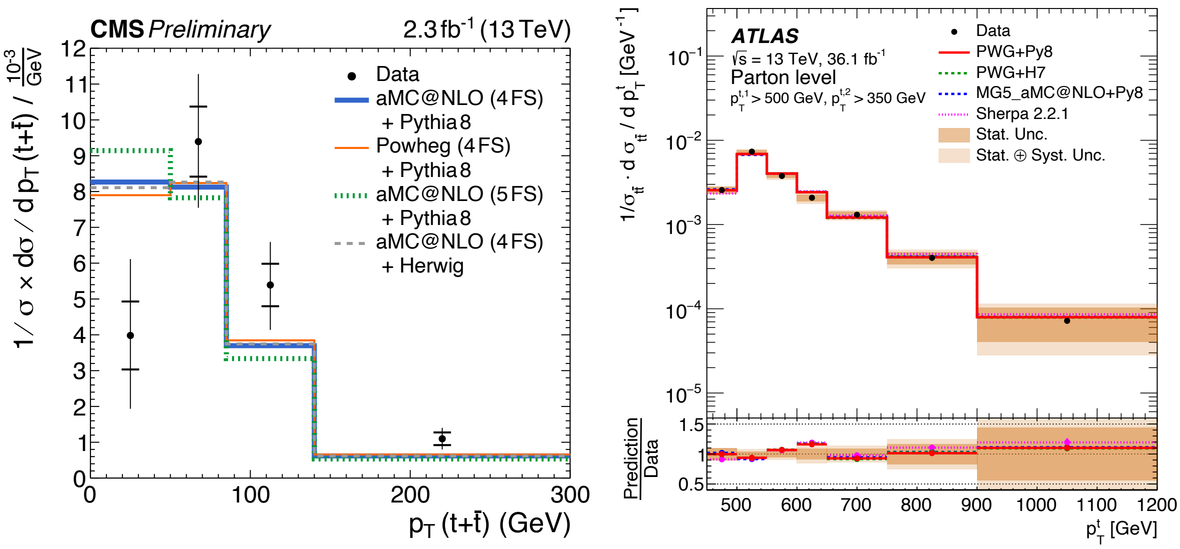

(a) single-top t-channel

(b) $\mathrm{t\bar{t}}$

Figure 2.9.: Results of differential cross-section measurements of single-top t-channel production presented by CMS (left) [65] and of $\mathrm{t\bar{t}}$ production presented by ATLAS (right) [68], both as function of top-quark transverse momentum (p_{T}) in proton-proton collisions at $\sqrt{s} = 13$ TeV. For $\mathrm{t\bar{t}}$, the average spectrum of both top quarks is shown.

found in Ref. 63.

The CMS collaboration presents differential measurements in the single-top t-channel as function of the top-quark transverse momentum (p_{T}) and rapidity[1] at $\sqrt{s} = 8$ TeV [64] and at $\sqrt{s} = 13$ TeV [65]. The ATLAS collaboration presents differential measurements in the single-top t-channel as well at $\sqrt{s} = 8$ TeV [66] and in the single-top tW-channel at $\sqrt{s} = 13$ TeV [67]. The most important takeaway is that none of these differential single-top measurements as function of the top-quark p_{T} go beyond a threshold of $p_{\mathrm{T}} = 300$ GeV, as can be exemplarily seen in Fig. 2.9a. In contrast, there are already results from $\mathrm{t\bar{t}}$ measurements available which reach $p_{\mathrm{T}} = 1200$ GeV as, e. g., one ATLAS measurement published in Ref. 68, see also Fig. 2.9b. This thesis presents a feasibility study on the possibility to extent the single-top threshold into the high-p_{T}, i. e. boosted, regime.

2.3 Event Topology and Monte-Carlo Simulation

One of the difficulties in physics analyses arises from the fact that the exact hard process behind a certain event from recorded data remains a priori unknown. For each event, only information from the detector is stored (*reconstruction level*). In order to study kinematic distributions on particle level—with the ability to estimate the individual contribution of different physical processes—, data is compared to models predicted by theory. However, it is not feasible to use analytical calculations to build these models. Therefore, events are simulated using Monte-

[1]These kinematic variables and others are explained in Sect. 3.2.1.

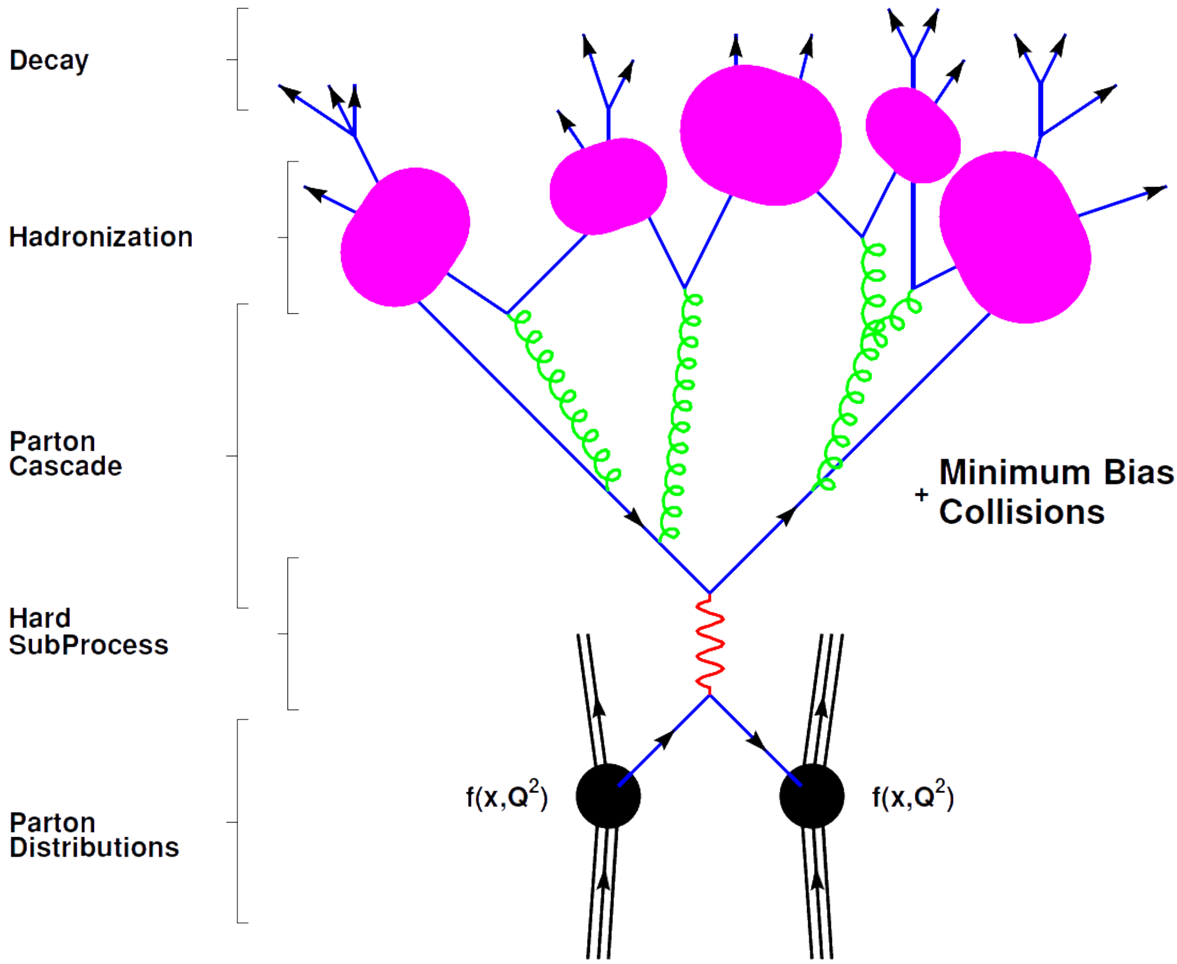

Figure 2.10.: Schematic illustration of a hadron-hadron collision event. Taken from Ref. 69.

Carlo (MC) methods, a stochastic technique based on random sampling. The resulting MC samples consist of large numbers of simulated events of known, pre-defined processes. In contrast to data events, MC events do not just store information from the detector but from all relevant evolutionary phases of the event, most importantly the initial hard process. This is called MC *truth* information. A generic hadron-hadron collision is shown in Fig. 2.10, highlighting the different steps of simulation which will be discussed in the following.

The event is initiated by the hard scattering of two partons from the incoming hadrons. The most relevant aspects regarding the calculation of matrix elements and cross sections have been introduced in Sect. 2.1. For the MC samples used in this thesis, the hard processes have been calculated with generators like POWHEG [70–74] and MADGRAPH5_AMC@NLO (MADGRAPH) [53, 75]. This stage of simulation is referred to as *parton level* and also includes information on the kinematics of all final-state particles.

Partons not involved in the hard process are either spectators, manifesting as diffractive remnants, or softly interact with other partons. In addition, these partons may interfere with the hard process via secondary interactions with the final-state particles. The occurrence of these additional parton interactions cannot be neglected despite being mostly soft compared to the hard process. This component of the collision is referred to as *underlying event* and is implemented in simulations. Hard process and underlying event cannot be distinguished from each other in the event reconstruction since they share the same interaction vertex. Thus, the underlying event must be understood in the first place to correct for bias in energy measurements arising from it.

Final-state and initial-state radiation consisting of gluons and additional quarks from the splitting of such gluons is known as parton shower. The parton shower, the subsequent hadronization, and the decay of unstable hadrons are simulated with the PYTHIA8 [76] software package. Up to this stage, one speaks about *generator level*. Since hadronization cannot be described analytically as described in Sect. 1.1.3, a phenomenological model is used in the simulation process, where gluons are treated as color strings according to the *Lund string model* [77].

The interaction of particles with the detector material is simulated with the GEANT4 [78] software package, using a detailed model of the whole CMS detector. This last stage is called *reconstruction level*, as mentioned before, and allows the simultaneous selection of MC and data events using the same variables.

At colliders like the LHC, protons are accelerated and collided in bunches. A single bunch crossing leads to multiple proton-proton interactions, each at a slightly different position. Most of these interactions do not yield interesting hard-scattering events but only soft QCD interactions. The clusters of decay products of the distinct proton-proton interactions, which are seen simultaneously in the detector, overlap. This biasses energy measurements of decay products from the event which one is interested in. This effect is known as *pile-up* and is also included in simulations.

3 The CMS Detector Experiment at the CERN Large Hadron Collider

The *Large Hadron Collider* (LHC) [79] at the *European Organization for Nuclear Research* (CERN[1]) is—measured by the reached center-of-mass energy and event rate—the most powerful particle accelerator ever built. It is designed for the acceleration and collision of protons at up to $\sqrt{s} = 14$ TeV. In addition, its design allows the study of heavy-ion collisions. Four major detector experiments are installed at the LHC which record the collisions:

- ATLAS: *A Toroidal LHC Apparatus* [80],
- CMS: *Compact Muon Solenoid* [81],
- LHCb: *LHC beauty* [82], and
- ALICE: *A Large Ion Collider Experiment* [83].

Both ATLAS and CMS are general-purpose particle detectors. LHCb particularly focusses on the physics of hadrons containing b quarks (“B physics”) and precision measurements of CP violation. ALICE focusses on heavy-ion collisions, QCD measurements, and the study of quark-gluon plasmas. There are in addition three minor detectors for more specialized research tasks, namely *LHC forward* (LHCf) [84], *Total Elastic and Diffractive Cross Section Measurement* (TOTEM) [85], and *Monopole and Exotics Detector at the LHC* (MoEDAL) [86].

The LHC has been constructed from 2001 to 2008. The first test beams of protons successfully circulated the LHC on September 10, 2008. From 2010 to 2013, the first operational run (Run I) took place, reaching $\sqrt{s} = 7$ TeV and later 8 TeV. After a two-year period of major upgrades with the aim to increase the center-of-mass energy and to increase the instantaneous luminosity (a measure for the event rate, see Sect. 3.1.2), Run II started in 2015, reaching 13 TeV. Run II ends in 2018. Further upgrades are scheduled for the upcoming years after which the LHC will continue its operation at 14 TeV in Run III and Run IV. For the far future, a major upgrade is planned: The *High-Luminosity LHC* (HL-LHC) [87] will increase the instantaneous luminosity by a factor of ten.

Integrated over its total runtime up to today, the LHC has produced hundreds of millions of individual top quarks, earning it the nickname “top factory” and providing best conditions

[1] Derived from the 1950s founding council, named *Conseil Européen pour la Recherche Nucléaire*.

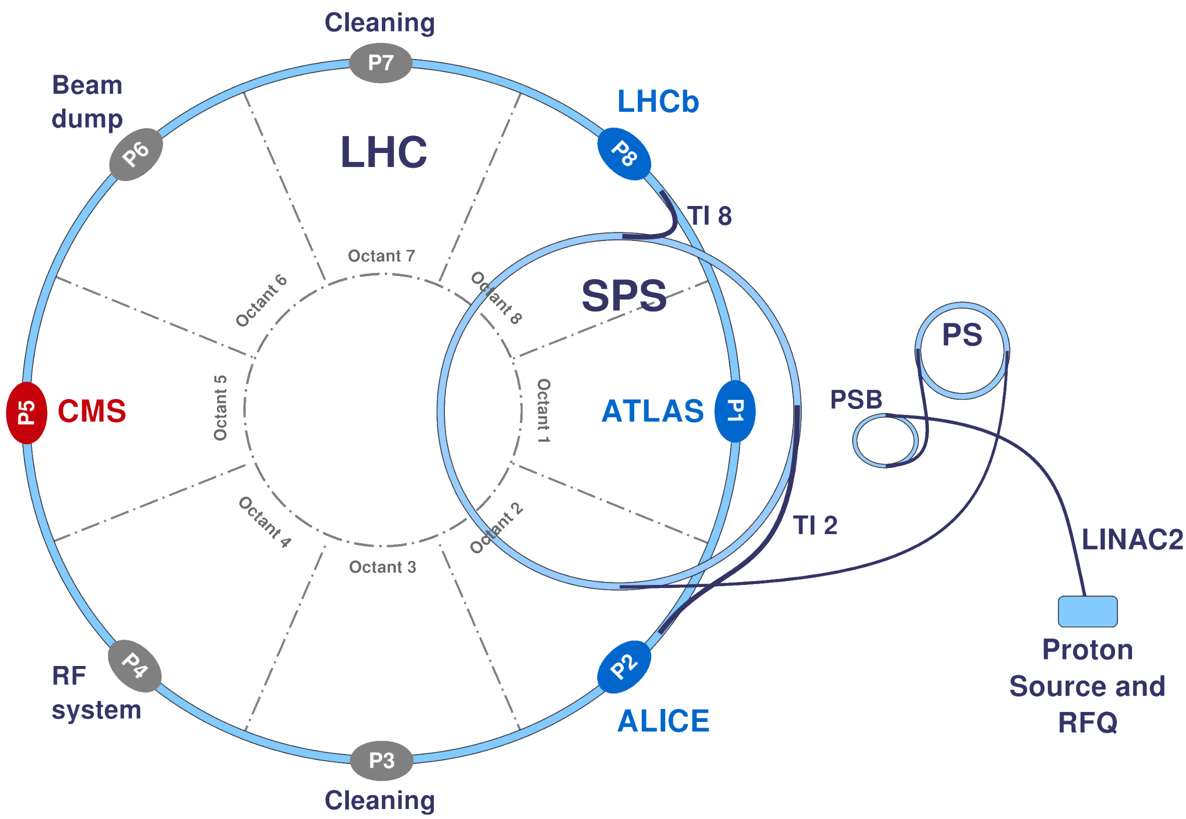

Figure 3.1.: The LHC and its system of pre-accelerators (not to scale). Proton pre-acceleration starts at LINAC2 and proceeds up to the SPS. Hereafter, they are divided into two separate beam channels, transferred through the transfer lines TI2 or TI8, and injected into the LHC main ring with opposite directions. The main ring itself is divided into octants with alternating curved and straight sections, each featuring crucial mechanisms including the CMS detector at Point 5. See running text in Sect. 3.1 and Tab. 3.1 for further explanations. Taken from Ref. 88.

for the study of top-quark physics. In this chapter, the LHC accelerator facility is presented (Sect. 3.1). The data analysed in this thesis was recorded by the CMS detector which is presented subsequently (Sect. 3.2).

3.1 The Large Hadron Collider

An overview of the LHC accelerator facility is given in Fig. 3.1. The core part of the complex is the LHC main ring, a synchrotron with a circumference of approximately 27 kilometers. The main ring is housed by a tunnel with a depth ranging between 50 and 175 meters and is located near Geneva, Switzerland, partially crossing the Franco-Swiss border. The same tunnel had formerly been used for the *Large Electron-Positron Collider* (LEP) [89], the largest lepton collider so far, that operated from 1989 to 2000. The ring is divided into eight arc segments, featuring curved and straight sections. All straight sections feature crucial components of different purpose (P1–P8), e. g. the detectors. In this section, the functionality of the accelerator complex is explained (Sect. 3.1.1) and the quantity *luminosity* is introduced in further detail (Sect. 3.1.2).

Table 3.1.: Proton energies after each acceleration stage in the LHC. At first, a simple electron-emitting cathode ionizes hydrogen gas. The resulting protons are extracted by an electric field, bringing them up to a kinetic energy of 90 keV, and then enter the RFQ. Later, each of the two LHC beam pipes takes 4 minutes and 20 seconds to be filled by the SPS. Another 20 minutes are required to boost the proton energy up to its maximum (7 TeV as per design of the LHC).

Acceleration stage	*Acronym*	*Final proton energy*
Radio-frequency quadrupole	RFQ	750 keV
Linear Accelerator 2	LINAC2	50 MeV
Proton Synchrotron Booster	PSB	1.4 GeV
Proton Synchrotron	PS	26 GeV
Super Proton Synchrotron	SPS	450 GeV
Large Hadron Collider	LHC	6.5 TeV during Run II

The information given here is based on Ref. 79.

3.1.1 The Accelerator Facility

Before entering the LHC main ring, protons need to be pre-accelerated in several stages. The pre-accelerators and the reached proton energies within the chain are listed in Tab. 3.1. During the last transition from the *Super Proton Synchrotron* (SPS) to the main ring, protons are divided into two individual beams which are then injected into anti-parallel channels, one with clockwise and the other one with anti-clockwise direction. At four interaction points (P1, P2, P5, P8), at which the detectors are located within their own respective underground caverns, the beams intersect to produce collisions.

The two beam pipes within the LHC synchrotron contain an ultra-high vacuum with a pressure of the order of 10^{-10} to 10^{-11} mbar to reduce beam loss as a consequence of interactions between beam particles and leftover gas molecules as much as possible. The synchrotron includes superconducting electromagnets which use a sophisticated cryogenic system to be cooled down by superfluid helium to temperatures of 1.9 Kelvin while operating at flux densities above 8.3 Tesla. In total, the synchrotron uses 1,232 dipole magnets, each about 15 meters long, to bend the charged hadrons' trajectories and to keep them on a near-to-circular orbit. The beam optics furthermore include 392 quadrupole magnets and additional higher-order multipole magnets to perpetually counter beam instabilities. The magnets are arranged according to the focussing-defocussing principle, known as FODO structure. The two contrarily directed beam channels are seated inside a common cryogenic mass, adopting the so-called dual-bore design, and share the same magnetic installations. Aside from the detector points, the straight sections within the arc segments include the following components: One radio-frequency (RF) linear accelerator (P4) to further increase the beam energy after leaving the pre-acceleration stages, the beam-injection (TI2 and TI8) and beam-dump mechanisms (P6), and two distinct collimator systems for momentum and betatron cleaning of the beams (P3 and P7).

3.1.2 Luminosity and Event Rate

At each interaction point, the expected rate of events which correspond to a specific physical process with cross section σ is given by

$$\frac{\mathrm{d}}{\mathrm{d}t}N = L \cdot \sigma \tag{3.1}$$

where the proportionality factor L is the *instantaneous* luminosity. The expected number of events (N) produced within a given time frame is calculated using the *integrated* luminosity

$$L_{\mathrm{int}} = \int L \cdot \mathrm{d}t. \tag{3.2}$$

The instantaneous luminosity at each interaction point is given by

$$L = N_{\mathrm{b}} f_{\mathrm{rev}} \frac{n_1 n_2}{4\pi\sigma_x\sigma_y} F, \tag{3.3}$$

where N_{b} states the number of proton bunches which each beam is partitioned into. Each beam consists of 2,808 bunches with a uniform separation of about 25 nanoseconds and a length of about 30 centimeters. Each bunch consists of $n_i \approx 1.15 \times 10^{11}$ protons. In the transverse plane perpendicular to the beam axis, the bunches have a Gaussian profile with a spreading area of $4\pi\sigma_x\sigma_y$. At the collision points, the bunches are squeezed to a few micrometers[2]. The variable $f_{\mathrm{rev}} = 11.245$ kHz refers to the revolution frequency of the beam particles inside the LHC[3] and F is a geometric correction factor. The LHC peak luminosity in proton-proton collisions currently is $L \approx 10^{34}\ \mathrm{cm}^{-2}\,\mathrm{s}^{-1}$.

3.2 The Compact Muon Solenoid Detector

The *Compact Muon Solenoid* (CMS) detector [81] at LHC Point 5 is located close to the city of Cessy, France, lowered into its own underground cavern at a depth of approximately 100 meters. The integrated luminosity over time for pp data-taking periods is shown in Fig. 3.2. The detector is built radially symmetric around the beam axis, using an onion-like layer structure. The overall setup consists of three parts, the cylindrical barrel enclosing the collisions point, and two end caps to cover the forward and backward regions. Fig. 3.3 gives an overview of the detector. In total, CMS has a length of 28.7 meters and a diameter of 15.0 meters while assembling a total weight of about 14,000 tonnes, dominated by the steel return yokes for the solenoid magnetic

[2] The exact dimension is not known and must be measured by Van-der-Meer scans to perform a valuable estimation on the luminosity yield [90].

[3] The particles travel at nearly the speed of light. More precisely, the proton Lorentz factor approximates to 6,930, assuming an energy of 6.5 TeV per proton in the laboratory rest frame.

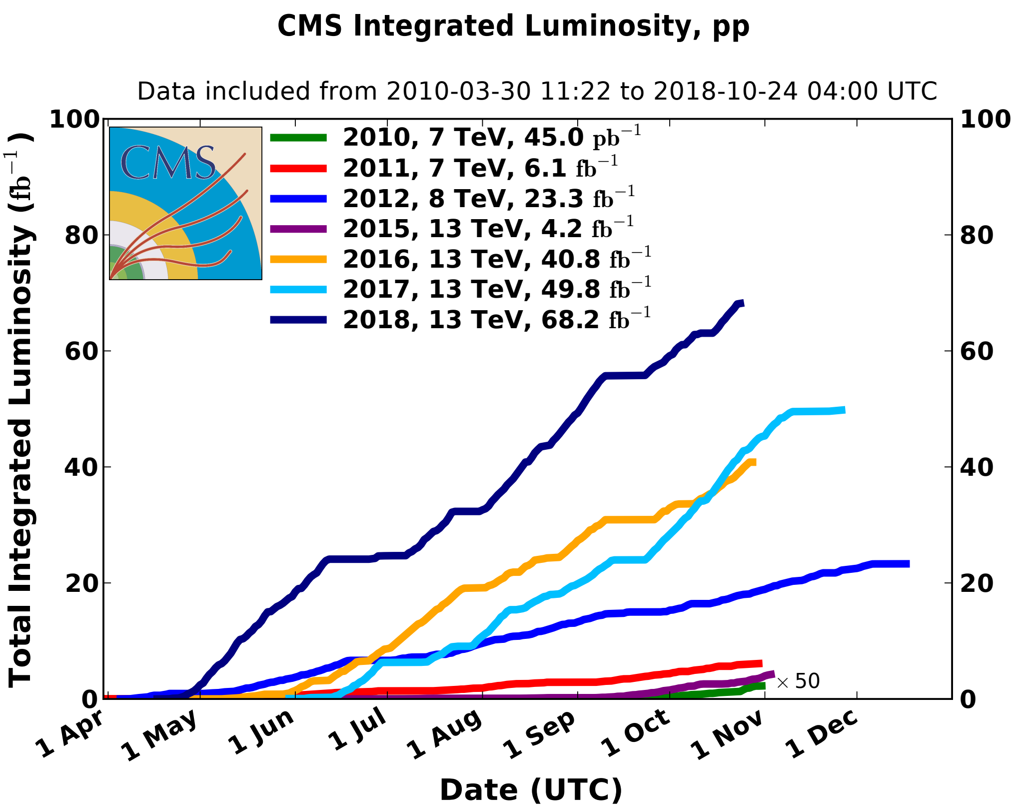

Figure 3.2.: Integrated luminosity versus time for each proton-proton data-taking period at CMS. The 2010 graph is multiplied by a factor of 50 to be visible. Taken from Ref. 91.

field. In this section, the coordinate system is introduced (Sect. 3.2.1) and the task of each main layer is discussed (Sect. 3.2.2). At last, the trigger system is described (Sect. 3.2.3).

3.2.1 Coordinate System and Important Kinematic Variables

The geometry of the CMS detector and the trajectories of particles inside it can be described by using a coordinate system in which the nominal collision point in the very center of the detector serves as origin. In a right-handed Euclidean description, the beam axis defines the z-axis, with its positive side pointing parallel to the direction of the anti-clockwise beam channel, and the transverse x-y-plane standing perpendicular to it. The x-axis points towards the center of the LHC, the y-axis points vertically upwards. Alternatively, adopting a system similar to spherical coordinates that reflects the cylindrically symmetric design of the machine and, simultaneously, the geometry of scattering events in a more practicable way, the transverse plane is parametrized by the azimuthal angle ϕ and the transverse radial distance starting at the beam axis. The polar angle θ spans between the transverse plane and the beam axis.

Since the colliding partons' exact momenta in z-direction with respect to the laboratory frame are not known in contrast to the total momentum of their hosting protons, one relies on kinematic variables which are invariant under Lorentz boosts along the z-axis and therefore inde-

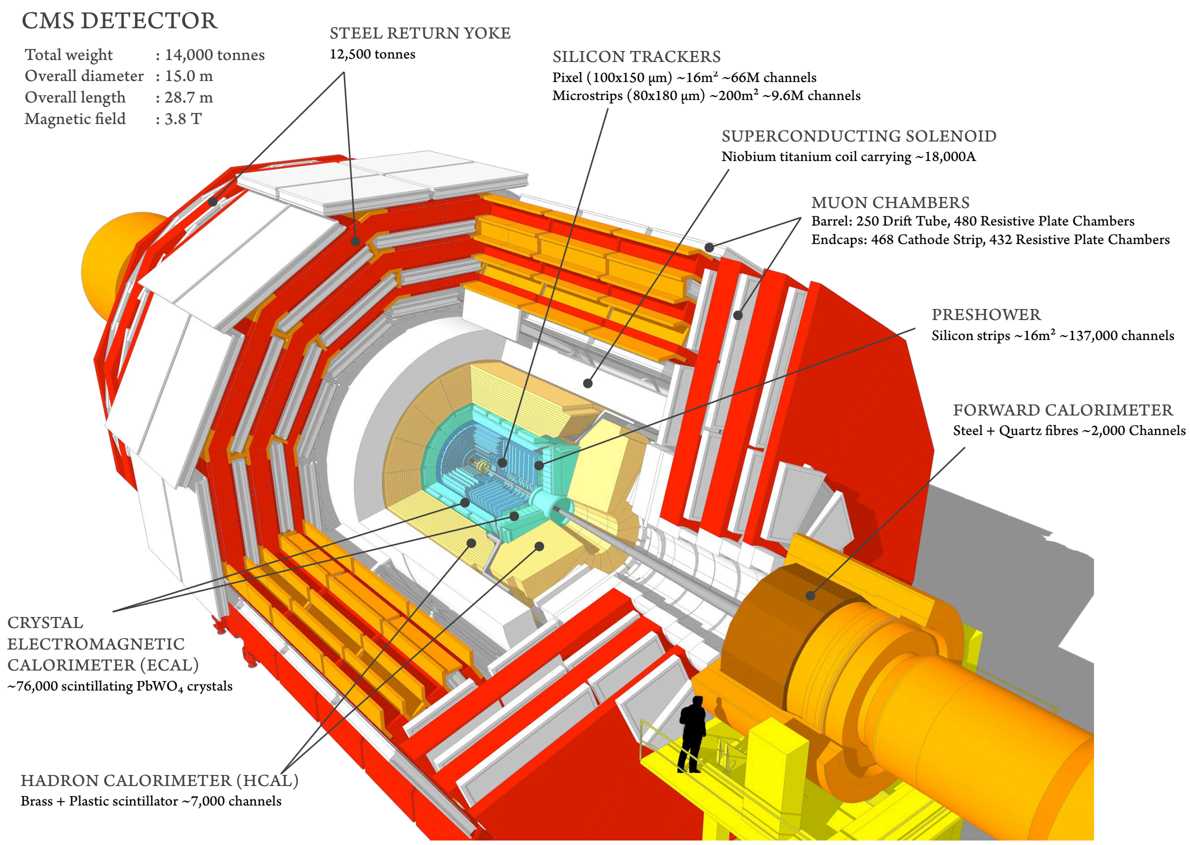

Figure 3.3.: Perspective cutaway view on the CMS detector. Taken from Ref. 92.

pendent from initial momenta. The transverse momentum

$$p_{\mathrm{T}} = \sqrt{p_x^2 + p_y^2} \tag{3.4}$$

of a particle emerging from the collision as well as its azimuthal angle fulfil this criterion. The polar angle θ has to be replaced by the more advantageous pseudo-rapidity

$$\eta = -\log\left(\tan\frac{\theta}{2}\right) \in [0, \infty). \tag{3.5}$$

It has the benefit that differences $\Delta\eta = |\eta_1 - \eta_2|$ are invariant under longitudinal Lorentz boosts as well. In the ultra-relativistic limit, the pseudo-rapidity is equal to the rapidity y of a particle, defined by its energy E and longitudinal momentum p_z via

$$y = \frac{1}{2}\log\left(\frac{E + p_z}{E - p_z}\right), \tag{3.6}$$

which in turn has the useful property that rapidity differences are invariant under Lorentz transformation. Another commonly used variable that measures the distance between two positions in the η-ϕ-plane is given by the formula

$$\Delta R = \sqrt{(\Delta\eta)^2 + (\Delta\phi)^2} \tag{3.7}$$

that is also conserved under longitudinal Lorentz boosts. Conclusively, the four-momentum of a particle can be transformed into a new set of components like $(E, p_x, p_y, p_z) \rightarrow (E, p_\mathrm{T}, \eta, \phi)$ by making use of the introduced variables.

3.2.2 Detector Components

In the following, the main components of the CMS detector are presented, starting with the innermost layer closest to the interaction point, the tracking system. Then, the electromagnetic (ECAL) and hadronic calorimetry (HCAL) in CMS is described. A special feature of the CMS detector is the placement of the calorimeters within the solenoid magnet which is presented next. The outermost layer contains a system of muon chambers, which exclusively detect muons, and is interleaved with steel return yokes for the magnetic field. The information given in this section is based on Ref. 81, 93. This section focusses on technical aspects and the overall design of the CMS detector. For the reconstruction and identification of particles emerging from a collision event, see Chapter 4.

Inner Tracking System. A single bunch crossing, taking place every 25 ns, yields a mean number of more than 20 proton-proton interactions, resulting into thousands of particles entering the detector. The tracking system lies closest to the interaction point and thus handles the highest particle flux of all the detector components. It aims at a precise reconstruction of trajectories of electrically charged particles, measuring momenta and charges by exploiting the coaxial solenoid magnetic field. To achieve best possible performance, the inner tracking system consists of semi-conducting silicon layers which provide a good single-point resolution and fast read-out. In total, the tracker has a longitudinal dimension of about 5.4 m and a transverse radius of 1.1 m, covering the solid-angle region described by $|\eta| < 2.5$. A schematic view of the tracking system is given in Fig. 3.4. The tracker uses two different types of detectors: The inner part consists of pixel detectors and the outer part of silicon strip detectors. Particles passing the layers create hits, i. e. a current by exciting electrons in the conduction band of the silicon, what can be measured. Tracks are reconstructed by fits made to these hits.

The pixel detector covers the smallest but closest volume around the interaction point. It consists of three barrel-region layers[4] and two endcap discs at each of the two forward regions. The barrel layers are located at 4.4 cm, 7.3 cm, and 10.2 cm distance from the beam axis. The endcap discs are located at a z-distance of 34.5 cm and 46.5 cm from the interaction point. Each of the 66 million implemented pixels covers an area of 100 μm × 150 μm, leading to a spatial resolution of approximately 10 μm in the r-ϕ-plane and 20 μm in z-direction.

Around the pixel detector, the silicon strip detectors are built. The barrel-region strip detectors are divided into two parts: The *Tracker Inner Barrel* (TIB) and the *Tracker Outer Barrel* (TOB). The TIB, covering a region of up to $|z| = 65$ cm, consists of four layers of strip sensors;

[4] Since 2017, the pixel barrel consists of four layers. Since this thesis' analysis is based on data recorded in 2016, the information given in this section are valid.

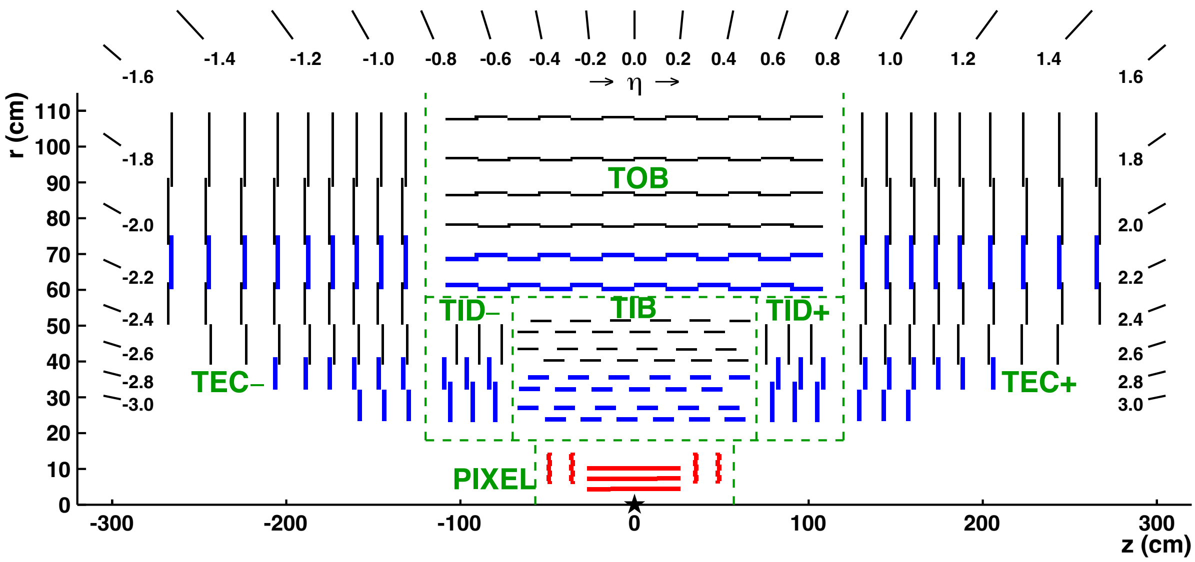

Figure 3.4.: Schematic view of the CMS tracker. The locations and layers of the pixel detector (PIXEL), tracker inner barrel (TIB), outer barrel (TOB), endcaps (TEC), and inner discs (TID) are shown. Taken from Ref. 94.

each of these strips is 320 µm thick and separated to the next one by 23–34 µm in the r-ϕ-plane and 23 µm in z-direction. The TOB covers a region of up to $|z| = 110$ cm and consists of six layers of strip sensors; each of these strips is 500 µm thick and separated to the next one by 120–180 µm. The spatial resolution is 35–52 µm in the r-ϕ-plane and 52 µm in z-direction. The endcap strip detectors are divided into the *Tracker Inner Disc* (TID) and the *Tracker End Cap* (TEC). The TEC, covering a region of 120 cm $< |z| <$ 280 cm, consists of nine layers of strip sensors. The TID is located in between the TEC and the TIB and consists of three layers of strip sensors. The TID strips and the three innermost TEC strips have a thickness of 320 µm and the six outer TEC layers have a thickness of 500 µm.

Electromagnetic Calorimeter. The ECAL measures energy deposits from particles which predominantly interact electromagnetically, i. e. electrons or positrons and photons. Muons and particles which predominantly interact via the strong force also deposit a small amount of their energy here; however, those particles traverse the ECAL carrying most of their initial energy and reach the HCAL or, in case of muons, the muon chambers to deposit most of their energy there. While the previously described tracking system is just able to detect charged particles, the calorimeters have the ability to measure also neutral particles.

The ECAL, shown in Fig. 3.5, is a homogeneous calorimeter, consisting of lead tungstate ($PbWO_4$) crystals which are used as scintillating material: Passing high-energetic particles generate an electromagnetic shower, exciting atoms or molecules within the material; when these return to their ground state, they emit light which can be measured by photodetectors. The lead tungstate has a high density of 8.28 $\mathrm{g\,cm^{-3}}$, however being optically clear. It has a radiation length of $X_0 = 0.89$ cm and a Molìere radius of 2.2 cm. Nearly 80 % of the scintillating pho-

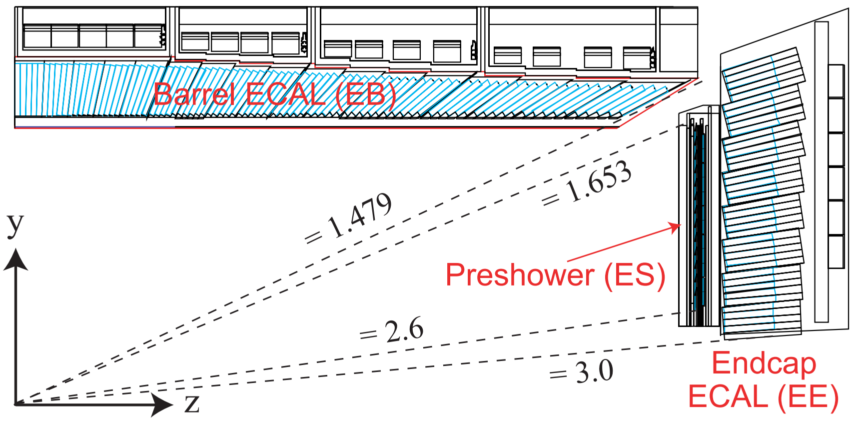

Figure 3.5.: Schematic view of the CMS electromagnetic calorimeter. Taken from Ref. 93.

tons are emitted within a timespan of 25 ns, the nominal bunch-crossing rate. These material characteristics allow for a very compact design of the ECAL with yet high granularity.

The ECAL barrel region (EB) consists of crystals each with a cross section of $22 \times 22\ \text{mm}^2$ and a depth of 230 mm corresponding to $25.8X_0$, covering a region of $0 < |\eta| < 1.479$. All crystals are arranged to face towards the interaction point. The EB begins at $r = 129$ cm distance from the beam axis. In the EB, scintillating photons are detected by silicon avalanche photodiodes (APD). The two ECAL endcaps (EE), respectively starting at $|z| = 314$ cm and covering a region of $1.479 < |\eta| < 3.0$, consist of crystals each with a cross section of $28.6 \times 28.6\ \text{mm}^2$ and a depth of 220 mm corresponding to $24.7X_0$. In the EEs, the scintillating photons are detected by vacuum phototriodes (VPT). In addition, preshower (ES) modules are seated before the EEs, consisting of two layers of lead, sandwiched with two layers of silicon strip detectors. They cover a region of $1.653 < |\eta| < 2.6$ and aid in the discrimination between forward signatures of photons and neutral pions.

The performance of the ECAL w. r. t. its energy resolution has been estimated by electron-beam measurements at beam energies of 20–250 GeV to be [95]

$$\frac{\sigma_E}{E} = \frac{2.8\,\%}{\sqrt{E\,[\text{GeV}]}} \oplus \frac{12\,\%}{E\,[\text{GeV}]} \oplus 0.3\,\% \qquad (3.8)$$

where the first term represents stochastic effects of the shower development within the ECAL, the second term covers noise from the electronics, and the third constant term describes calibration errors and effects from non-uniform light collection. These three terms are added in quadrature. Later, the ECAL has also been calibrated and its resolution has been measured with pp collisions at $\sqrt{s} = 7$ TeV [96].

Hadronic Calorimeter. Around the ECAL, the larger HCAL is built. It aims at the measurement of the energy of strongly interacting particles. These particles have interaction lengths which are much larger than the radiation lengths of electrons or photons which are stopped by the ECAL. Since the remaining space between the ECAL and the solenoid magnet is limited,

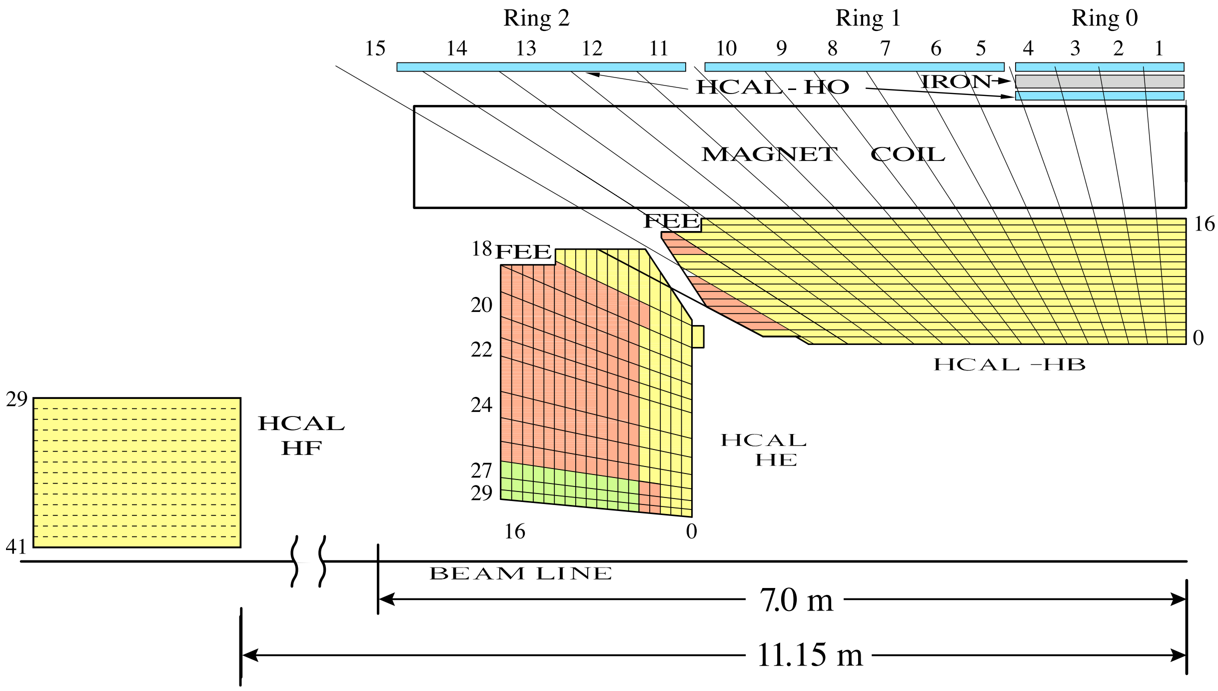

Figure 3.6.: Schematic view of the CMS hadronic calorimeter. In addition to the main components, the locations of the front-end electronics (FEE) of the endcap (HE) and barrel (HB) components are shown. Signals of the tower segments with the same color are sent to the same photo sensors to provide horizontal segmentation. Taken from Ref. 97.

the CMS collaboration has favoured the HCAL to be designed as a non-homogeneous sampling calorimeter. The active material of a sampling calorimeter for the read-out is interspersed with absorber material. The active material consists of scintillating plastic into which wavelength-shifting fibres are embedded. The absorber material consists of non-magnetic brass which, due to its high density, has a radiation length of $X_0 = 1.5$ cm and a comparatively short nuclear interaction length of 16.42 cm.

The HCAL consists of four different components, as illustrated in Fig. 3.6. It consists of the *Hadron Barrel* (HB), the *Hadron Endcap* (HE), the *Hadron Outer* (HO), and *Hadron Forward* (HF) calorimeters. The HB covers a region of $0 < |\eta| < 1.3$ and is further divided into two half-barrels (HB+ and HB−), each consisting of 18 identical wedges arranged around the beam axis. Each wedge consists of 18 absorber plates; deviating from the default brass design, the outer- and innermost layers are made of stainless steel to protect the structural integrity; they alternate with 17 scintillators. The active material in each wedge is further divided into multiple towers, leading to a final resolution of 0.087×0.087 in the η-ϕ-plane. The HCAL energy resolution in the barrel region can be parametrized as [98]

$$\frac{\sigma_E}{E} = \frac{115.3\,\%}{\sqrt{E\,[\mathrm{GeV}]}} \oplus 5.5\,\% \tag{3.9}$$

where the first term represents stochastic effects of the hadronic shower development and the second constant term describes calibration errors.

The HO is located outside of the solenoid magnet, covering a region of $0 < |\eta| < 1.26$. It aims at the measurement of remnant hadrons which manage to traverse the HB and the solenoid material, finalizing the hermeticity of the HCAL in the barrel region. The HO provides the same resolution as the HB; the HO further plays an important role in the measurement of missing energy resulting from neutrinos (and possibly yet unknown particles) leaving the detector.

The HE covers an additional region of $1.3 < |\eta| < 3.0$. Together with the HB, the HE encloses the ECAL. The active material is divided into towers as well. At smaller $|\eta|$, the tower segmentation is $\Delta\phi = 5°$, $\Delta\eta = 0.087$. At higher $|\eta|$, the segmentation becomes $\Delta\phi = 10°$, $0.09 < \Delta\eta \leq 0.35$.

The HF covers the most forward region of all calorimetry components with $3.0 < |\eta| < 5.0$. The cylindrical HF absorbers are exclusively made of steel. Since the forward region has to handle a dense and high-energetic particle flux, the HF active material is made of more robust quartz fibres. Cherenkov radiation induced by charged particles inside the hadron showers is amplified by fast photomultipliers. The HF tower segmentation is $\Delta\phi = 10°$, $\Delta\eta = 0.175$, with slightly different values for the inner- and outermost ones.

Superconducting Solenoid Magnet. The magnet is the core device of the CMS machine. It generates a homogeneous magnetic field equivalent to a constant flux density of 3.8 T inside the tracker (originally designed for 4 T with a nominal current of 19,500 A). The field is directed parallel to the z-axis. Its task is the bending of trajectories of electrically charged particles, allowing the calculation of their charges and momenta by measuring the resulting radii of curvature. The solenoid has a length of 12.9 meters, an inner diameter of 5.9 meters, and weighs 220 tonnes. As described before, not just the tracker but also the calorimeters are placed inside the solenoid since the energy resolution of particles would be worse if they would pass the solenoid material first. On the outside of the solenoid, the muon detectors are embedded into a structure of steel yokes which return the magnetic field and guide it outside the solenoid where it switches its sign. With a weight of about 11,400 tonnes, the return yokes have the most significant contribution to the total weight of the CMS detector.

Muon Detectors. The only detectable particles able to traverse all prior presented components are muons. Since muons have an approximately 200 times higher mass than electrons, they behave different when entering materials and are considered for all practical purposes as minimally ionizing particles (MIP). The magnetic field inside the muon system is 2 T, having a reversed sign compared to the tracker. Like the tracking system, the muon system allows for a measurement of muon momenta, providing additional information for an enhanced muon reconstruction. An overview of the components of the muon system is shown in Fig. 3.7.

In the muon-system barrel region (MB), covering $0 < |\eta| < 1.2$, aluminium drift-tube (DT) chambers are arranged in four layers as concentric twelve-sided cylinders around the beam axis. The gaseous DTs have an average size of 2.0×2.5 m^2 and, all together, contain about 172,000

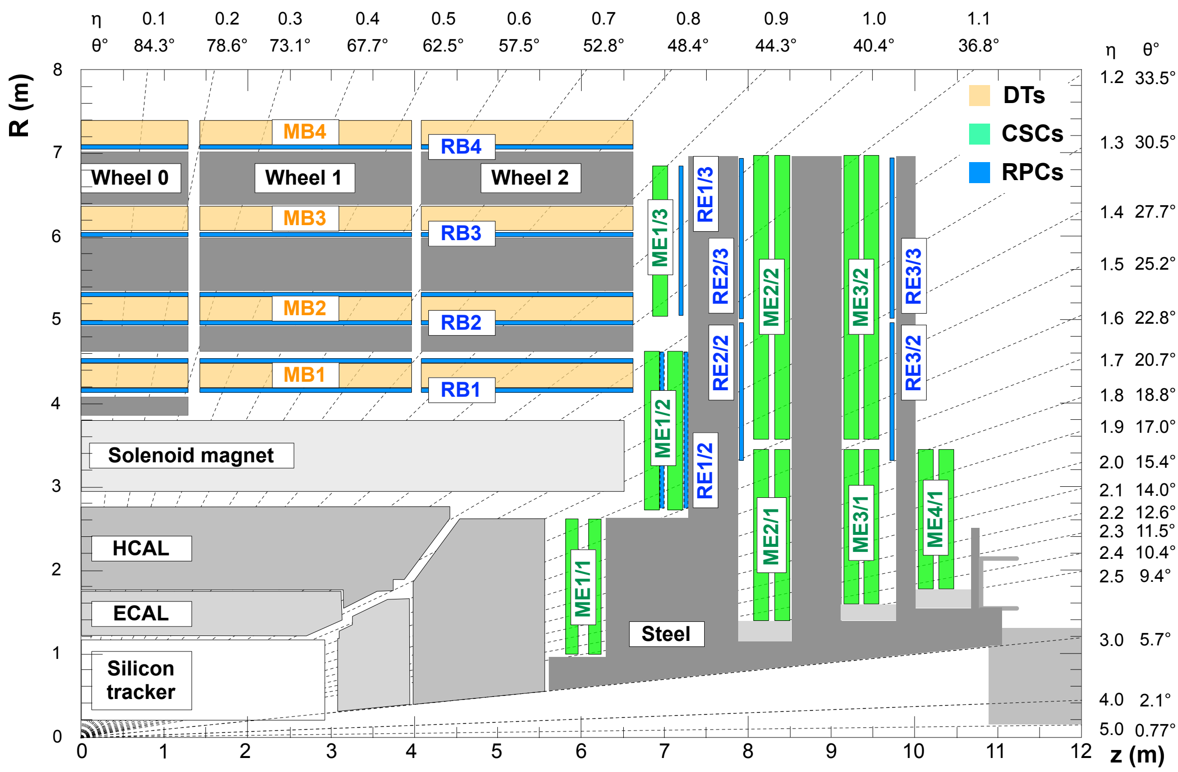

Figure 3.7.: Schematic view of a quadrant the CMS detector, highlighting the components of the muon system. The locations of the drift tubes (DT), cathode strip chambers (CSC), and resistive plate chambers (RPC) are shown. Taken from Ref. 99.

sensitive wires. The two inner layers are respectively surrounded by gaseous resistive plate chambers (RPC) which aid in muon identification; each of the two outermost layers has one RPC in front of it. In the muon-system endcap regions (ME), covering $0.9 < |\eta| < 2.4$, gaseous cathode strip chambers (CSC) are used. The ME is divided into four layers of CSCs, interleaved with the RPCs in the $0.9 < |\eta| < 1.6$ region. The CSCs provide a high time resolution of ~ 1 ns and have finer segmentation, necessary due to the high particle flux in the forward region.

3.2.3 Data Acquisition and Trigger System

The interval between bunch crossings at the nominal LHC design luminosity is 25 ns which corresponds to a frequency of 40 MHz. Each bunch crossing however also leads to a mean number of more than 20 proton-proton interactions, resulting in an enormous amount of potential data to be stored (~ 100 TB s^{-1}). The real-time processing as well as actual storage of all this data is not feasible. Thus, the recorded collisions must be cut down to a more reasonable number on the fly, aiming at the selection of interesting events for further offline analysis. This is realized by the CMS trigger system which decides in real time whether an event shall be stored or discarded. There are several trigger levels, the *Level-1 Trigger* (L1) and the *High-Level Trigger* (HLT), which are briefly discussed in the following.

The L1 trigger is hardware-based, implemented by field-programmable gate arrays (FPGA) and application-specific integrated circuits (ASIC), allowing for a low latency of about 3.2 µs. While the data from a recorded collision is held in buffers, an approximate calculation is performed to estimate an event's value of interest, using individual or globally combined key information from the calorimeters and the muon system which provide fast read-out. The L1 trigger aims at the rejection of soft QCD events and accepts events featuring high-energetic jets, muons, or significant amounts of missing energy. After the L1 trigger, the event rate is reduced by a factor of one thousand to about 50 kHz.

The HLTs consist of a computing cluster, running software similar to offline-analysis frameworks. Each event is sent to a processor which has access to the full read-out of all detector components. Sophisticated algorithms categorize each event e. g. by the presence of muons or electrons. In the end, the total event rate is further reduced to about 100 Hz, keeping only a millionth part of the initial amount of collisions. The data is ultimately stored on tape and copied to sites of collaborating institutes around the world via the *Worldwide LHC Computing Grid* (WLCG).

Reconstruction and Identification of Final-State Physics Objects

4

Event data recorded by the CMS detector consists of a collection of raw signals of the subsystems (Sect. 4.1) which have to be translated into objects with actual physical meaning. For this reason, the CMS collaboration has developed the *Particle-Flow* (PF) algorithm (Sect. 4.2) [100] to thoroughly combine information of all subsystems to reconstruct particle candidates and to identify which kind of particle has been detected. After this initial data reconstruction, more specific physics analysis can take place. The presented analysis has been performed with *CMS Offline Software* (CMSSW) [101]. In this chapter, the reconstruction methods and identification criteria for objects relevant to this analysis are introduced. These objects are muons (Sect. 4.3), electrons (Sect. 4.4), and hadron cascades known as jets (Sect. 4.5). At last, missing transverse momentum is introduced (Sect. 4.6).

4.1 Signatures of Particles in the Detector

Starting from the interaction point, particles emerging from an event first enter the inner tracking system. Only electrically charged particles produce signals (*hits*) within the sensitive layers of the tracker which are then used to reconstruct corresponding trajectories (*tracks*) and origins (*vertices*). The trajectory-bending magnetic field from the solenoid allows to measure momentum and charge of each particle. In the following ECAL, electrons and photons are hermetically stopped and deposit their entire energy hereby. They produce electromagnetic showers which are detected as single clusters of energy in neighbouring cells. Charged and neutral hadrons may initiate showers within the ECAL as well but are predominantly stopped within the HCAL. The clusters are used to estimate energy and direction of the corresponding particles. Muons produce hits in the tracker but traverse the calorimeters with just little interaction. They however certainly produce signals in the outermost layers of the detector, the muon chambers, which function as additional muon trackers. Since the magnetic field outside the solenoid has a reversed sign compared to within the inner tracking system, two individual tracking measurements enhance the reconstruction of the momentum of muons. Neutrinos are just able to interact weakly and thus leave the detector without any interaction.

Fig. 4.1 visualizes the individual particle signatures. In Fig. 4.2, an exemplary event display of a candidate for W-associated single top-quark production in the dileptonic decay channel is

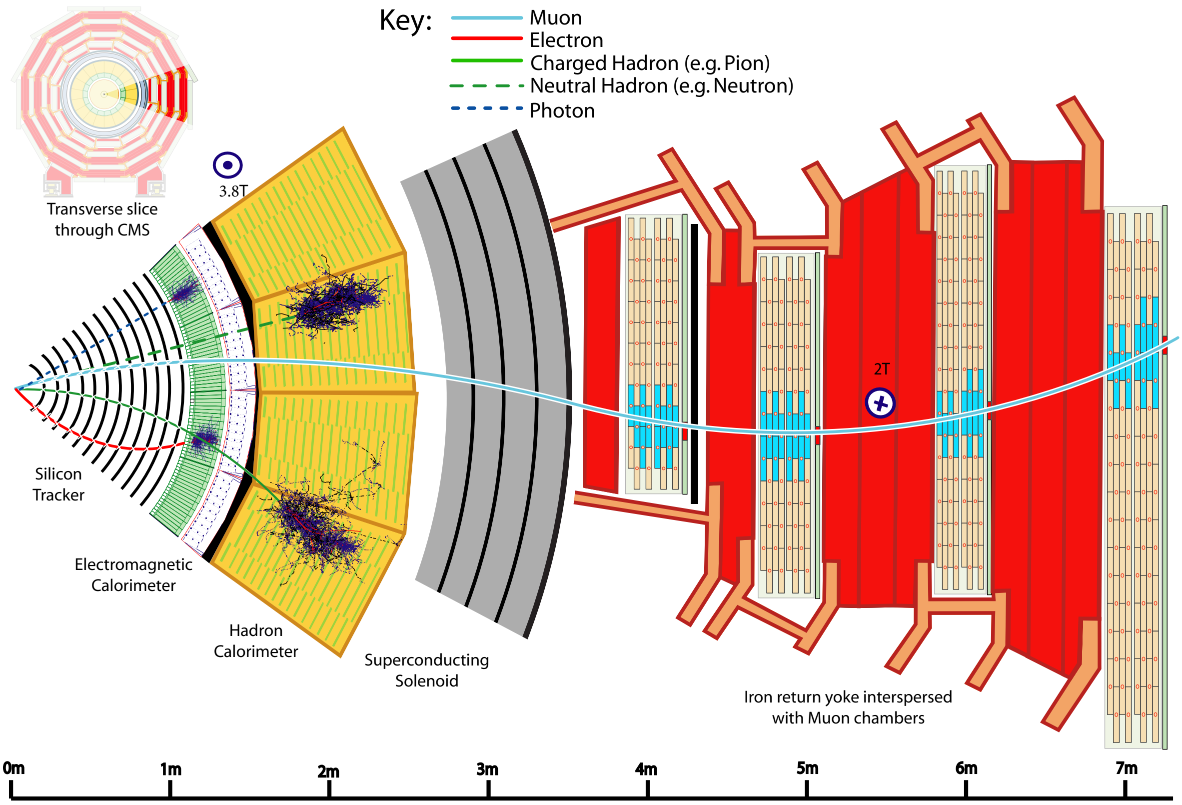

Figure 4.1.: Cross-sectional view of a segment of the CMS detector. All types of detectable particles and their corresponding interactions with the detector material are shown. From the left-hand to the right-hand side, the inner tracking system, the ECAL, the HCAL, the solenoid magnet, and the muon system are visible. Taken from Ref. 100.

shown which combines all particle signatures relevant for this thesis: One electron, one muon, one hadronic jet, and missing energy from neutrinos. This example however shows a resolved, i. e. non-boosted, top-quark decay in contrast to the boosted signature investigated in this thesis.

4.2 The Particle-Flow Algorithm

The PF algorithm uses the combined information from all sub-systems of the CMS detector to reconstruct and identify objects from the signals described in the previous section.

In the first step, tracks in both the inner tracking system and the muon chambers are reconstructed by combining hits in an iterative procedure. After each iteration, hits which have been assigned to a track are removed from the event input. In the beginning of this procedure, the quality requirements on the track reconstruction are very tight but become looser with an increasing number of iterations. Isolated tracks have a higher reconstruction efficiency than the ones which are closely flanked or overlapped by others. In addition to track reconstruction, the ECAL and HCAL cells with energy deposits are clustered. Cells with local energy maxima above a certain threshold serve as seeds for the clustering of adjacent cells which are required

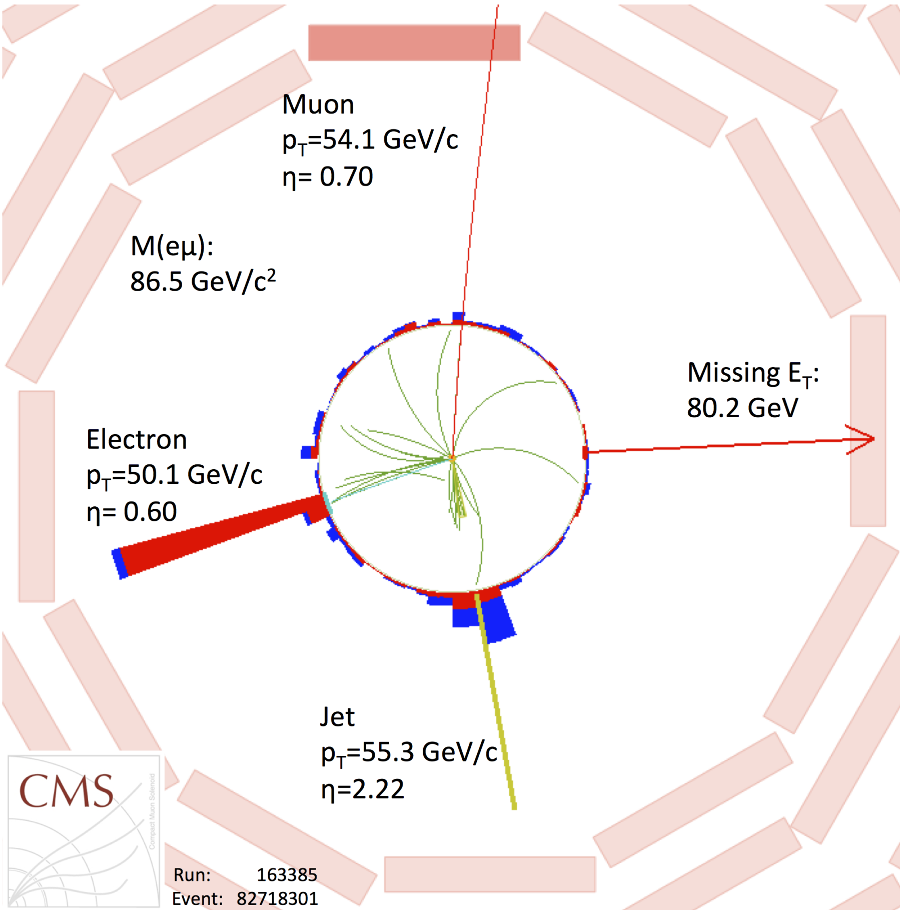

Figure 4.2.: Exemplary event display of the CMS detector. A candidate of W-associated single top-quark production at $\sqrt{s} = 7$ TeV in the dileptonic decay channel is shown. In addition to an electron and a muon, a jet coming from the b quark decay is visible. ECAL (HCAL) deposits are shown as red (blue) bars with a height proportional to the magnitude. The two neutrinos, which cannot be detected, add up as missing transverse energy $\not{E}_{\mathrm{T}}$. Taken from Ref. 102.

to exceed another given threshold.

In the second step, the accumulated information is used to link the individual detector signals from the sub-systems to each other. Tracks within both the inner tracking system and the muon chambers are compared to each other. If tracks from both sub-systems are matchable by fulfilling the criteria described by a certain χ^2-fit, they are assigned to a *global muon* candidate. The tracks from this global muon are removed from the event input. Remaining inner tracks are extrapolated from their outermost hit into the calorimeters. If matches between tracks and clusters of energy deposits are found, they are linked to each other. Electrons cause bremsstrahlung in the inner tracking system what leads to the presence of additional photon deposits in the ECAL. Those bremsstrahlung deposits are linked to corresponding electron tracks to account for the energy loss of the electrons. Elements within the sub-detectors which have been linked to each other are referred to as *block*.

In a last step, these blocks are identified as certain particles. If tracks in the muon system are matchable to tracks in the inner tracking system and the measured momenta are in agreement with each other following certain criteria, the initial global muon will now be classified as a *PF muon*. Similarly, information from the ECAL and the inner tracking system is used to identify *PF electrons*. All tracks and energy deposits belonging to PF muons and electrons are removed from further consideration. The remaining tracks are assigned to *PF charged hadrons*. Afterwards, *PF photons* and *PF neutral hadrons* are identified.

4.3 Muon Identification

After their reconstruction by the PF algorithm, the muon candidates are required to fulfil additional identification criteria to be considered as valuable objects to perform offline analyses with. The CMS collaboration recommends different working points (WP) which differ by the applied criteria and provide different identification efficiencies and misidentification rates. In this analysis, the *tight* WP [103, 104] is used to identify muons in the μ+jets signal selection (cf. Chapter 5). The criteria of the tight WP are listed in the following:

- The candidate is reconstructed as a global muon, i. e. within the inner tracking system and the outer muon detectors.
- The candidate is reconstructed by the PF algorithm.
- The global track fit returns $\chi^2/\mathrm{n.d.f.} < 10$, where n.d.f. is the number of degrees of freedom of the fit.
- At least one hit within the muon chambers is included in the global track fit.
- The candidate is matched to hits from at least two muon stations.
- The track from the inner tracking system has a transverse impact parameter of $d_{xy} < 2$ mm w. r. t. the primary vertex.
- The track from the inner tracking system has a longitudinal distance of $d_z < 5$ mm w. r. t. the primary vertex.
- At least one hit within the pixel detector is present.
- Hits from at least six different layers within the inner tracking system are present.

In the e+jets signal selection, a veto on additional muons is implemented using the *loose* WP [103]. A loose muon candidate has to fulfil just two criteria: Firstly, the candidate is reconstructed as a global muon or within the inner tracker only. And, secondly, the candidate is reconstructed by the PF algorithm.

In addition to these identification criteria, a cut on the relative isolation of the muon candidate is applied. The relative isolation is defined as a numerical value calculated from the kinematics of all hadron and photon PF candidates within a cone of $\Delta R < 0.4$ around the muon candidate. As formula, it reads

$$I_{\mathrm{rel}} = \frac{\sum p_{\mathrm{T}}(h^{\pm}) + \max\left(0, \sum p_{\mathrm{T}}(\gamma) + \sum p_{\mathrm{T}}(h^{0}) - \frac{1}{2}\sum p_{\mathrm{T}}(h^{\pm}_{\mathrm{PU}})\right)}{p_{\mathrm{T}}(\mu)} \tag{4.1}$$

where $p_{\mathrm{T}}(\gamma)$ are all photon transverse momenta and $p_{\mathrm{T}}(h^{0})$ and $p_{\mathrm{T}}(h^{\pm})$ the transverse momenta of all neutral and charged hadrons which originate from the same primary vertex. The transverse momenta of all charged hadrons from different primary vertices, denoted by $p_{\mathrm{T}}(h^{\pm}_{\mathrm{PU}})$, enters the calculation as well, approximating the contribution of neutral hadrons coming from different primary vertices than the muon candidate.

4.4 Electron Identification

Electron candidates have to fulfil additional identification criteria after they have been reconstructed by the PF algorithm. In CMS, different approaches to define electron WPs exist such as simple cut-based identification or more sophisticated identification using multivariate algorithms. In addition, a less common solution for high-energetic electrons exists. In this analysis, the cut-based approach is chosen since it is sufficiently robust while offering good performance. The cut-based identification is described in Ref. 105. The *tight* WP ($\sim$ 70 % efficiency) is chosen for the e+jets signal selection, the *veto* WP ($\sim$ 95 % efficiency) is used to reject events with additional electrons in the μ+jets signal selection. The variables considered for the selection are listed in the following. The cut values are given in Ref. 105.

- $\sigma_{\eta\eta}$ describes the shape of the shower in the ECAL along η.
- $|\Delta\eta_{\mathrm{in}}|$ ($|\Delta\phi_{\mathrm{in}}|$) is the distance in pseudorapidity (azimuth) between the track matched to the ECAL cluster and the cluster itself.
- H/E is the ratio of HCAL and ECAL energy deposits matched to the electron candidate.
- I_{rel} is the relative combined PF isolation of the electron candidate which however is differently calculated than for muons.
- $|E^{-1} - p^{-1}|$, where the candidate's energy E is obtained from the calorimeters and the momentum p from tracker information.
- $N_{\mathrm{e.m.i.h.}}$ is the expected number of missing inner tracker hits.
- d_{xy} (d_z) is the transverse (longitudinal) impact parameter w. r. t. the primary vertex.

In addition to these cuts, each electron candidate regardless of the considered WP has to pass a veto which accounts for electrons originating from photon conversion ($\gamma \to e^{+}e^{-}$) in the ECAL.

4.5 Reconstruction of Jets

Quarks and gluons hadronize and, therefore, cannot be detected as independent particles like electrons or muons. The arising particle cascades, predominantly consisting of hadrons, can be clustered as jets. In this thesis, the understanding of jets plays a very important role, especially since the boosted single top quark of the signal process decays hadronically. In this section, the jet clustering algorithms used in this thesis are presented (Sect. 4.5.1 and Sect. 4.5.2). In general, a jet algorithm has to guarantee that the resulting jets fulfil two important quality criteria: Firstly, infrared safety which means that a jet must not change regardless of including or excluding soft gluon radiation. And, secondly, collinear safety which means that a jet also must not change regardless of the presence or absence of collinear gluon splitting. It is further guaranteed that the clustering has minimal sensitivity to side-effects from not well-understood physical phenomena like hadronization, underlying event, and pile-up. The jet algorithms presented in the following fulfil these criteria. In addition, this section includes an overview on the tagging of jets originating from b quarks (Sect. 4.5.3) and on the calibration corrections which need to be applied to jet energies (Sect. 4.5.4).

4.5.1 The Anti-k_T and Cambridge/Aachen Algorithms

There are two different types of jet clustering algorithms: Cone-type algorithms and sequential clustering algorithms. The algorithms used in this thesis are based on the sequential clustering approach. In this approach, a jet is clustered via iteratively assigning new objects to the jet until a certain stop criterion is fulfilled. One widely-used implementation is described in the following.

A list of all objects ("pseudojets") reconstructed in the detector is given as input. For each object i, the value

$$d_{i,\mathrm{B}} = k_{\mathrm{T},i}^{2n} \tag{4.2}$$

is calculated, where $k_{\mathrm{T},i}$ refers to the transverse momentum of the pseudojet. This variable is an effective measure for the distance between pseudojet and beam axis. For each pair of two pseudojets i and j, the following quantity is calculated which measures an effective distance between them:

$$d_{ij} = \min\left(k_{\mathrm{T},i}^{2n}, k_{\mathrm{T},j}^{2n}\right) \cdot \frac{\Delta R_{ij}^2}{R_0^2} \tag{4.3}$$

where ΔR_{ij} describes the distance of the two pseudojets in the η-ϕ-plane. The constant R_0 sets a limit on the cone size of the final jet, or more precisely its radius, and can be freely chosen. If $d_{ij} < \min(d_{i,\mathrm{B}}, d_{j,\mathrm{B}})$, both pseudojets are combined and the clustering variables are re-calculated for this combined object. At some point, no pseudojets fulfilling this last criterion are leftover and the combined object is considered to be one jet. The pseudojets in this jet are removed from the input list. The variable n, which occurs within the definitions of d_{ij} and $d_{i,\mathrm{B}}$, is also a free parameter. The choice of n is crucial: It affects the order in which pseudojets are clustered and, in turn, the shape of the jet. A distinction is made between three implementations which define different algorithms:

- $n = 1$: k_{T} algorithm [106, 107],
- $n = 0$: Cambridge/Aachen (CA) algorithm [108], and
- $n = -1$: Anti-k_{T} algorithm [109].

The Anti-k_{T} algorithm is the standard jet algorithm used within the CMS collaboration since it yields jet shapes which are mostly circular. CA jets are clustered by only using geometrical information of objects (since $n = 0$ removes any k_{T}-dependence) and have less uniform shapes. This however makes it more suitable in studies of jet substructures. In this analysis, Anti-k_{T} jets with a radius parameter of $R_0 = 0.4$ are used. They are referred to as "AK4" jets from now on. Only AK4 jets which fulfil $p_{\mathrm{T}} > 30$ GeV and $|\eta| < 2.4$ are considered in this analysis. They further need to fulfil the criteria of the *loose* WP for PF jets described in Ref. 110.

4.5.2 Boosted Top Quarks and the HOTVR Algorithm

The physical aspects of the decay of top quarks have been discussed in Sect. 2.2.3. Concerning the top-quark reconstruction, one has to distinguish two cases: If a top quark is produced in rest or close to rest, its decay products can fly off into any direction. This leads to a resolved signature, ideally consisting of three distinct jets—assuming that the top quark decays hadronically. On the other hand, if the reduced center-of-mass energy is large enough, the top quark might be highly relativistic and its decay products will be boosted into a preferred direction. Fig. 4.3 visualizes how the distance between the particles emerging from top-quark decays decreases with increasing top-quark transverse momentum. In the highly boosted regime, it is very likely that the individual jets from the hadronic decay products overlap and form one large jet.

In this analysis, candidates for such jets are clustered with an algorithm called *Heavy Object Tagger with Variable R* (HOTVR) [111]. HOTVR is also capable of applying additional criteria on these jets to significantly increase their likelihood to actually originate from top quarks; this is referred to as top tagging. This analysis uses the default HOTVR top-tagging criteria which will be discussed during the presentation of the event selection in Sect. 5.4.2. In the following, the HOTVR jet clustering algorithm is presented which as well is based on sequential clustering.

HOTVR clusters jets similar to the CA algorithm. However, the main difference is given by the fact that the constant radius parameter R_0 is substituted by an effective radius defined by

$$R_{\mathrm{eff}} = \begin{cases} R_{\mathrm{min}} & \text{for } \rho/p_{\mathrm{T}} < R_{\mathrm{min}}, \\ R_{\mathrm{max}} & \text{for } \rho/p_{\mathrm{T}} > R_{\mathrm{max}}, \\ \rho/p_{\mathrm{T}} & \text{else.} \end{cases} \tag{4.4}$$

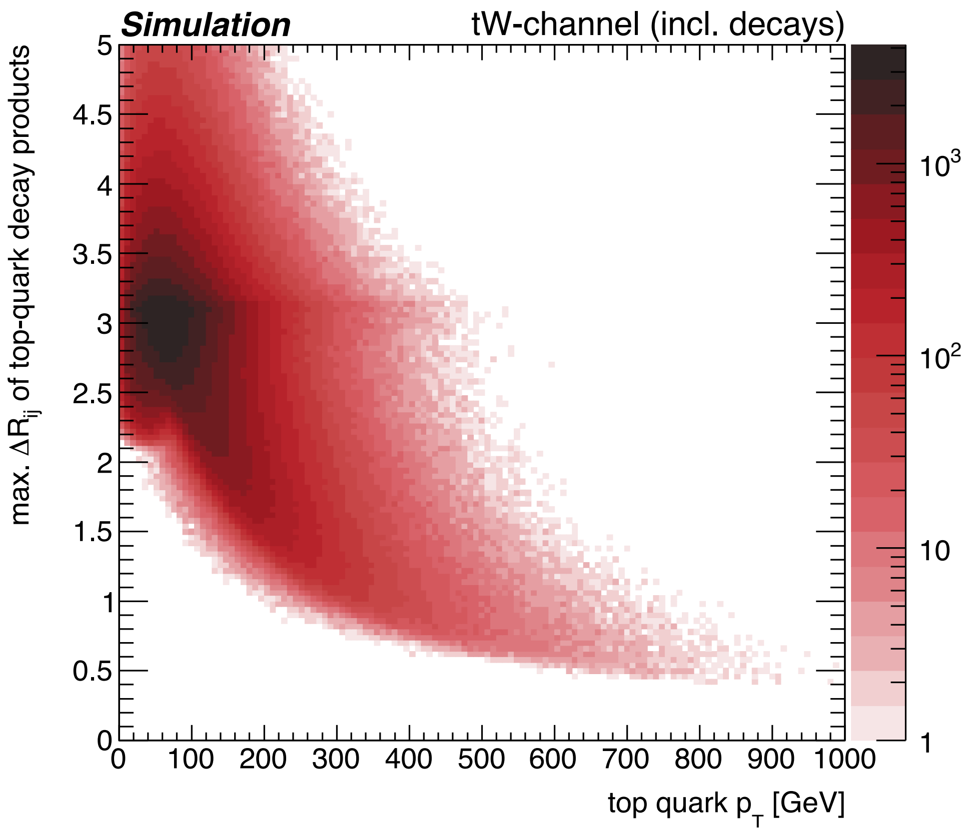

Figure 4.3.: Maximum ΔR_{ij} between two of the three decay products of the top quark versus the p_{T} of the top quark. This generator-level study only shows W-associated single top-quark production. However, top-quark decays certainly behave independent from the production channel. Furthermore, not just hadronic but all possible decay products are included. This still makes no difference. The used MC samples have been generated with POWHEG and PYTHIA8.

Herein, p_{T} refers to the transverse momenta of the pseudojets to be clustered. This p_{T} dependence is scaled by the constant parameter ρ which has a default value of 600 GeV. Consequently, HOTVR adapts the jet size to the overall jet p_{T} what is an advantageous feature for the clustering of boosted jets which shrink in size the more boosted they are. The radius boundaries are set to $R_{\mathrm{min}} = 0.1$ and $R_{\mathrm{max}} = 1.5$. To exclude soft radiation from the clustering process, referred to as “grooming”, HOTVR implements a mass-jump criterion: If the invariant mass m_{ij} of two pseudojets fulfils the threshold $m_{ij} > \mu$, where the constant parameter μ has a default value of 30 GeV, the following criterion will be checked:

$$\theta \cdot m_{ij} > \max\left(m_i, m_j\right). \tag{4.5}$$

The parameter $\theta \in [0,1]$ can be used to scale the strength of the criterion. The default is set to $\theta = 0.7$. Only if this criterion and, additionally, the threshold $p_{\mathrm{T},i} > p_{\mathrm{T,sub}}$ with default value $p_{\mathrm{T,sub}} = 30$ GeV are fulfilled, both pseudojets are combined. If not, the softer jet is classified as originating from soft radiation and is removed. If the initial two pseudojets are combined, they are stored as subjets of the combined pseudojet. In this analysis, all default values for

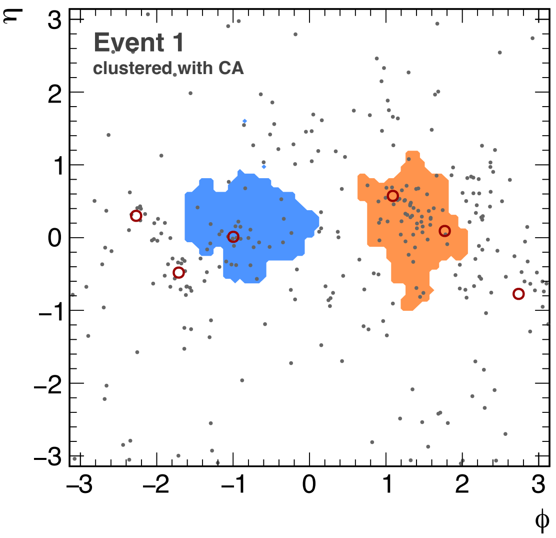

(a) CA, low p_T

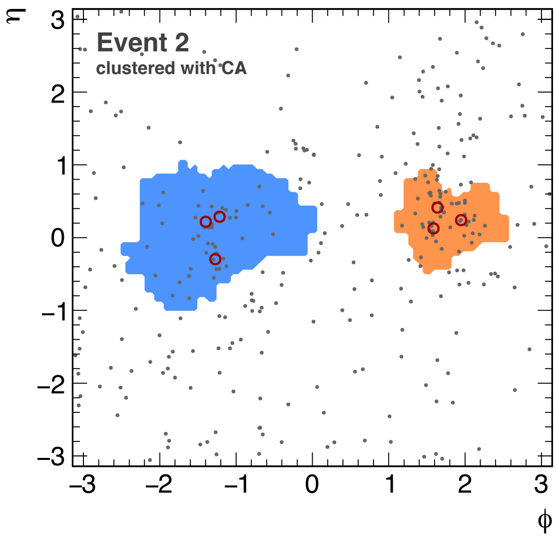

(b) CA, high p_T

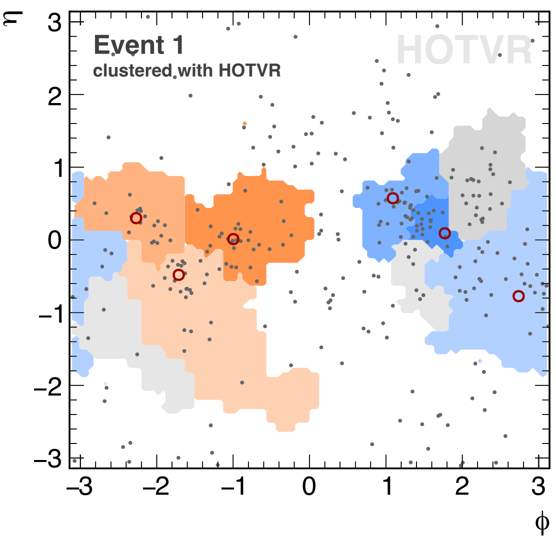

(c) HOTVR, low p_T

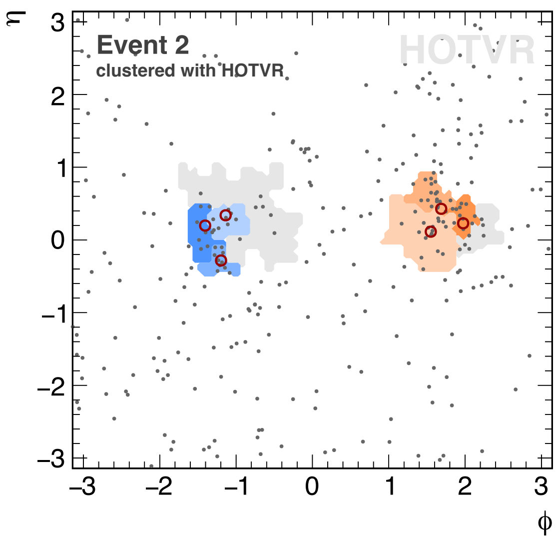

(d) HOTVR, high p_T

Figure 4.4.: Comparison of top-jet clustering by the CA and HOTVR algorithms. The decays of simulated all-jets $t\bar{t}$ events are shown within the η-ϕ-plane. The low-p_T (event 1) and high-p_T (event 2) regimes are compared. The orange and blue clusters represent the two leading jets corresponding to the hadronically decaying top quarks. Stable particles which are used as input for the clustering algorithms are shown as grey dots. The locations of the initial three quarks from the top-quark decays on generator level are marked by red circles. In case of HOTVR, the areas with different color intensity represent the identified subjets, where increasing intensity corresponds to higher p_T. Grey areas are rejected from the jet clustering by the HOTVR mass-jump criterion. Taken from Ref. 111.

the mentioned parameters are used. A comparison of the CA and the HOTVR algorithm with the task to cluster jets from boosted top quarks is given in Fig. 4.4, using simulated $t\bar{t}$ events. The matching between HOTVR subjets on reconstruction level and top-quark decay products on generator level is illustrated.

Within the framework used in this thesis, HOTVR implements the *Pile-Up Per Particle Identification* (PUPPI) [112] algorithm to mitigate pile-up effects in the clustering process.

4.5.3 The CSV b-Tagging Algorithm

In analyses with focus on top-quark physics, the identification of jets originating from b quarks plays a central role. Since top-quark decays basically always include b quarks, b-tagging is a very useful tool to discriminate top-quark signal processes from specific backgrounds which mostly feature jets originating from light-flavour quarks or gluons. The B meson, the most prominent manifestation of b quarks after hadronization, has a relatively long lifetime of about $\tau_B \approx 1.6 \times 10^{-12}$ s [12]. Taking into account the relativistic velocities of b quarks emerging from an event and the associated time dilatation, B mesons may travel a few millimeter ($c\tau_B \approx$ 480 µm without dilatation) within the detector before it decays into further particles. This gives rise to a displaced vertex, a very distinctive signature within an event. The high-resolution CMS tracking system is able to distinguish between primary and such secondary vertices. Fig. 4.5 depicts the geometry of a secondary vertex relative to its associated primary vertex.

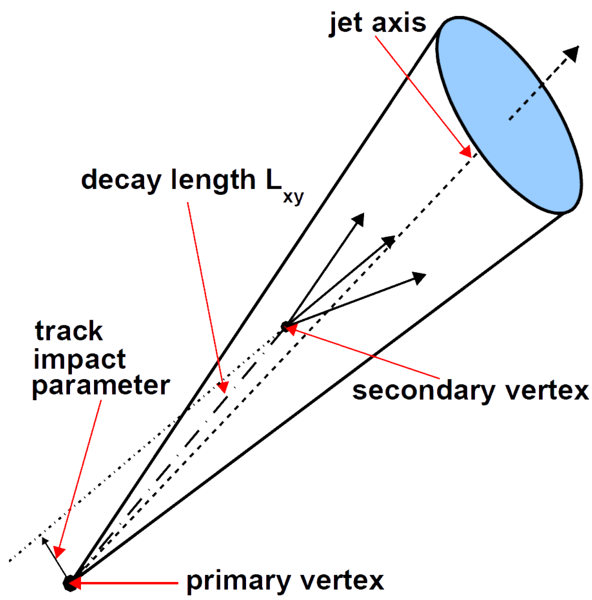

Figure 4.5.: Sketch of a displaced vertex as originating from the decay of a B meson. Taken from Ref. 113.

To identify b-quark jets, the CMS collaboration developed the *Combined Secondary Vertex* (CSV) algorithm [114] and its updated version CSVv2 [115]. It is an algorithm which, based on several input variables, returns a discriminator in the interval $[0, 1]$ which corresponds to the likelihood that the jet originates from a b quark. Examples for those input variables are the impact parameter of the reconstructed secondary vertex, the fraction of charged hadrons within the jet, and the invariant jet mass. CMS recommends different working points [116] which differ from each other by the cut value applied on the CSV discriminator. In this analysis, jets are considered to be b-tagged if they fulfil the requirement of the *medium* WP of the CSVv2 algorithm which corresponds to a cut value of 0.800. In this analysis, scale factors are applied to account for differences in b-tagging efficiencies and mis-tagging rates between data and simulation.

4.5.4 Jet Energy Corrections

The energy of jets found by clustering algorithms on reconstruction level need to be corrected due to several reasons which are discussed in the following. A detailed description of this procedure can be obtained from Ref. 117. In general, the four-momentum of the raw jet is calibrated according to the ansatz

$$p^{\mu}_{\text{corrected}} = \mathcal{C}_{\text{JEC}} \cdot p^{\mu}_{\text{raw}} \tag{4.6}$$

where the correction factor $\mathcal{C}_{\text{JEC}}$ can be factorized as

$$\mathcal{C}_{\text{JEC}} = C_{\text{offset}}\left(p_{\text{T}}^{\text{raw}}\right) \cdot C_{\text{MC}}\left(p'_{\text{T}}, \eta\right) \cdot C_{\text{rel}}\left(\eta\right) \cdot C_{\text{abs}}\left(p''_{\text{T}}\right). \tag{4.7}$$

The first factor (C_{offset}) corrects the jet energy for noise effects from electronics and excess energy from pile-up. It depends on the raw jet p_{T} before applying any corrections. The second factor (C_{MC}) scales the momentum of the reconstructed jet to the energy of the corresponding generated MC particle jet such that both become equal on average. These factors are calculated in two-dimensional bins of the jet pseudorapidity and the jet transverse momentum after applying the first correction (p'_{T}). The third factor (C_{rel}) accounts for small relative differences between data and simulation, dependent on η only. The fourth factor (C_{abs}) is applied to obtain the absolute jet energy scale, based on previous calibration measurements using γ/Z+jets events. This last factor depends on the jet transverse momentum after applying all other corrections (p''_{T}).

In this analysis, jet energy corrections are applied to AK4 jets and HOTVR subjets but not to the overall HOTVR jet since no such corrections are available yet.

4.6 Missing Transverse Energy

For each event, the net transverse momentum is assumed to be zero. Variations in the alignment of the two proton beams are insignificant and can be neglected. Consequently, the missing transverse energy[1] ($\not{E}_{\text{T}}$) in an event is defined as the absolute value of the negative of the vectorial

[1] The terms missing momentum and missing energy are interchangeable in this context.

sum of all transverse three-momenta $\vec{p}_{\mathrm{T},i}$ of essentially all particle-flow objects, i. e. charged leptons, all jets fulfilling a certain p_T threshold, and photons. As formula, the definition reads

$$\not{E}_\mathrm{T} = \left|\vec{\not{E}}_\mathrm{T}\right| = \left|-\sum_i \vec{p}_{\mathrm{T},i}\right|. \tag{4.8}$$

Only the missing *transverse* energy is a valid observable since the initial momenta of the interacting partons along the beam axis and, thus, also the longitudinal component of missing energy remain unknown. The total missing energy is indeterminable.

The presence of missing transverse energy can be interpreted in multiple ways. Since neutrinos interact just weakly according to the SM, they practically do not interact with the detector material. As a consequence, signatures of events with neutrinos in their final state feature missing transverse momentum. In general, similar effects from certain hypothetical new particles of BSM physics must be considered as well. However, this analysis does not focus on the search for new physics and treats missing momentum as exclusively arising from neutrinos. Missing energy can also be a result of measuring errors of course. Information on the performance of the PF reconstruction of missing transverse energy can be obtained from Ref. 118.

5 Analysis Strategy, Event Selection, and Signal Event Reconstruction

This chapter covers the first part of the analysis performed in this thesis. The utilized data set from the CMS detector is presented and the Monte-Carlo samples, which are used to model the SM prediction, are listed in Sect. 5.1. Thereafter, the general analysis strategy for this thesis is formulated in Sect. 5.2, including the motivation for using the W-associated production channel of single top quarks as signal channel. The expected SM backgrounds of this channel which have to be considered during the analysis are introduced in Sect. 5.3. The event selection is presented in Sect. 5.4 which defines the phase space for the studies and measurements in the next two chapters. In Sect. 5.5, formulae for the reconstruction of final-state objects in signal events are given.

5.1 Data Set and Monte-Carlo Samples

The data analyzed in this thesis has been recorded by the CMS detector in 2016, using proton-proton collisions at a center-of-mass energy of $\sqrt{s} = 13$ TeV. Fig. 5.1 shows the integrated luminosity delivered by the LHC and integrated luminosity recorded by CMS versus time. The majority of delivered events has been recorded by the detector. The total 2016 data set corresponds to an integrated luminosity of 37.76 fb^{-1}. Data used in this analysis is required to fulfil various quality criteria. Therefore, luminosity sections in which the detector or accelerator facility were not fully operational are excluded from the analyzed data set such that it is reduced to an integrated luminosity of 35.87 fb^{-1}.

This analysis makes use of two distinct signal channels, distinguished by the presence of a single electron or single muon in the event signature. The complete signal signature is defined in Sect. 5.2. Each of the two analysis channels uses one subset of the total 2016 data set. Both subsets are statistically independent. For the electron channel, the `SingleElectron` data stream is chosen, containing only events for which a single-electron L1 trigger fired. Analogously, the `SingleMuon` data stream is chosen for the muon channel.

The event selection described in this chapter is simultaneously applied on data and MC simulation samples. The MC generators used for the samples used in this thesis have been introduced in Sect. 2.3. The full list of MC samples utilized in this thesis are given in Tab. 5.1 and Tab. 5.2. The samples are scaled to the integrated luminosity $L_{\text{int}} = 35.87\ \text{fb}^{-1}$ of the analyzed data set

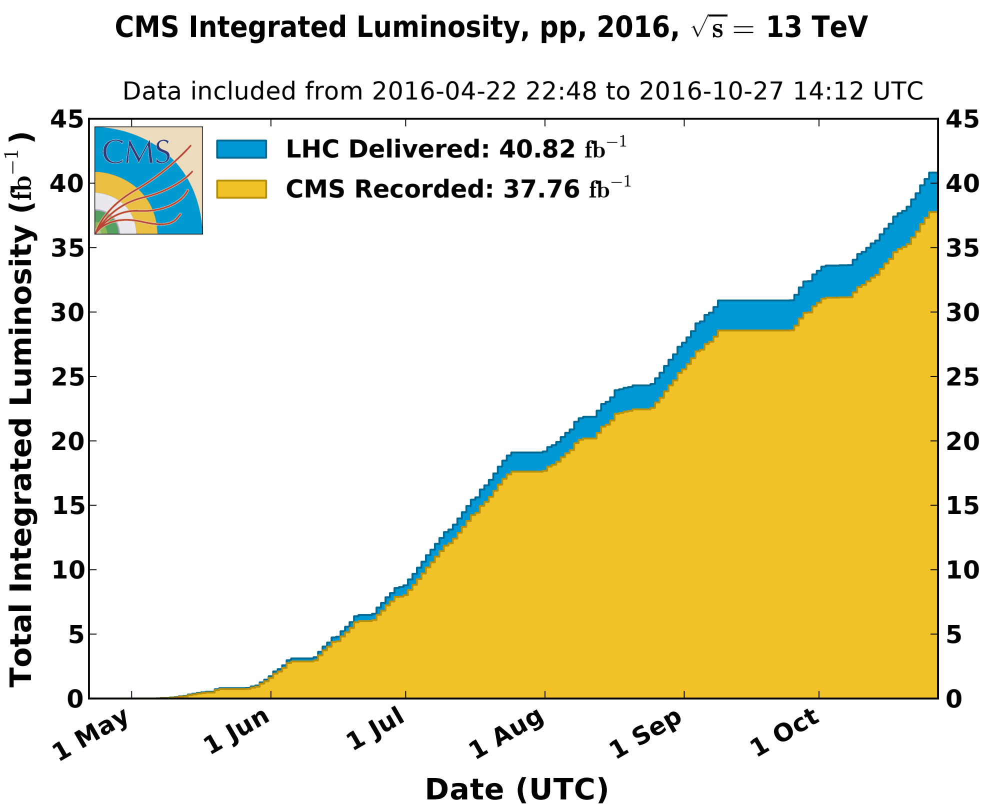

Figure 5.1.: Integrated luminosity versus time for the 2016 proton-proton data-taking period at the CMS experiment. The luminosity delivered by the LHC at the interaction point (blue) and the luminosity which has actually been recorded by the CMS detector (yellow) are compared to each other. The histograms are binned in days. Taken from Ref. 91.

by applying weights. These luminosity weights w_i are individually calculated as

$$w_i = \frac{\sigma_i}{N_i} \cdot L_{\text{int}} \tag{5.1}$$

where N_i is the number of events stored in the sample and σ_i is the cross section of the considered process. Most processes are divided into various sub-samples, binned in a certain kinematic variable, to still provide sufficient MC statistics in the highest-energetic regions which the selection aims at.

5.2 Signal Definition and Analysis Strategy

As presented in Sect. 2.2.4, there are no measurements of single top-quark production in the boosted kinematic regime previous to this thesis. Each one of the three canonical channels of single top-quark production comes with individual phenomenology, as presented in Sect. 2.2.2. Fig. 5.2 shows the spectra of top-quark p_{T} for all three canonical channels at a center-of-mass energy of $\sqrt{s} = 13$ TeV, as predicted by MC simulation. To define a signal for this analysis, a consideration has to be done concerning each channel's suitability for such a measurement in

Table 5.1.: Utilized Monte-Carlo samples. For each simulated process, the generator software, the expected cross section, and the total number of events is given. Most processes are divided into several sub-samples, binned in different variables: $t\bar{t}$ uses the invariant mass ($M_{t\bar{t}}$) of the top-quark pair, W+jets uses the W boson's p_T, and Z+jets uses the scalar sum over all jets' p_T (H_T). Some samples are non-inclusive, i. e. the simulated processes do not feature all physically possible but just the most relevant decay channels w. r. t. the targeted event selection. E. g., the signal samples (tW) exclude fully hadronic decays. Continued in Tab. 5.2 for QCD samples.

Simulated process	*MC generator*	*Cross section [pb]*	*Number of events*
Single top			
tW^- (di- and semileptonic)	POWHEG	19.4376	8 629 378
$\bar{t}W^+$ (di- and semileptonic)	—"—	19.4376	8 681 265
t-channel (t; inclusive)	—"—	136.02	5 993 570
t-channel ($\bar{t}$; inclusive)	—"—	80.95	3 927 980
s-channel (t and $\bar{t}$; leptonic)	MADGRAPH	3.36	3 370 582
$t\bar{t}$+jets (inclusive decays)			
$M_{t\bar{t}} \in [0, 700)$ GeV†	POWHEG	831.76	76 920 200
$M_{t\bar{t}} \in [700, 1000)$ GeV	—"—	76.605	38 556 810
$M_{t\bar{t}} \in [1000, \infty)$ GeV	—"—	20.578	24 540 191
W+jets ($W \to \ell\nu$)			
$p_T \in [100, 250)$ GeV	MADGRAPH	676.3	178 194 873 646
$p_T \in [250, 400)$ GeV	—"—	23.94	617 245 383
$p_T \in [400, 600)$ GeV	—"—	3.031	11 569 720
$p_T \in [600, \infty)$ GeV	—"—	0.4524	1 830 034
Z+jets ($Z \to \ell\bar{\ell}$; $M_{\ell\bar{\ell}} \geq 50$ GeV)			
$H_T \in [70, 100)$ GeV	MADGRAPH	215.619	9 615 980
$H_T \in [100, 200)$ GeV	—"—	181.302	10 414 580
$H_T \in [200, 400)$ GeV	—"—	50.4177	9 312 572
$H_T \in [400, 600)$ GeV	—"—	6.9839	3 940 285
$H_T \in [600, 800)$ GeV	—"—	1.6814	8 292 160
$H_T \in [800, 1200)$ GeV	—"—	0.7754	2 668 311
$H_T \in [1200, 2500)$ GeV	—"—	0.1862	595 906
$H_T \in [2500, \infty)$ GeV	—"—	0.0044	399 147
Diboson (inclusive decays)			
WW	PYTHIA8	118.7	7 981 014
WZ	—"—	47.13	3 995 778
ZZ	—"—	16.523	1 988 069

†This sample is initially inclusive w. r. t. $M_{t\bar{t}}$ but on-the-fly cut down to $M_{t\bar{t}} < 700$ GeV during the preselection. Cross section and number of events given in this table refer to the inclusive sample. The other two $t\bar{t}$ samples serve to provide higher statistics in the region of high top-jet transverse momentum which the selection aims at.

Table 5.2.: Utilized Monte-Carlo samples (continued from Tab. 5.1). For each simulated process, the generator software, the expected cross section, and the total number of events is given. The QCD samples are binned in $\hat{p}_T$, the transverse momentum transfer of the $2 \rightarrow 2$ process on generator level. The μ+jets analysis channel exclusively uses the muon-enriched and the e+jets analysis channel the electromagnetically enriched QCD samples, respectively.

Simulated process	*MC generator*	*Cross section [pb]*	*Number of events*
QCD (μ-enriched)			
$\hat{p}_T \in [15, 20)$ GeV	PYTHIA8	3 819 570.0	4 104 069
$\hat{p}_T \in [20, 30)$ GeV	—”—	2 960 198.4	30 318 903
$\hat{p}_T \in [30, 50)$ GeV	—”—	1 652 471.46	29 759 918
$\hat{p}_T \in [50, 80)$ GeV	—”—	437 504.1	19 710 314
$\hat{p}_T \in [80, 120)$ GeV	—”—	106 033.6648	23 413 977
$\hat{p}_T \in [120, 170)$ GeV	—”—	25 190.5151	8 012 991
$\hat{p}_T \in [170, 300)$ GeV	—”—	8654.4932	17 466 153
$\hat{p}_T \in [300, 470)$ GeV	—”—	797.3527	47 744 437
$\hat{p}_T \in [470, 600)$ GeV	—”—	79.0255	13 523 641
$\hat{p}_T \in [600, 800)$ GeV	—”—	25.0951	9 969 168
$\hat{p}_T \in [800, 1000)$ GeV	—”—	4.7074	18 357 746
$\hat{p}_T \in [1000, \infty)$ GeV	—”—	1.6213	13 006 608
QCD (em. enriched)			
$\hat{p}_T \in [20, 30)$ GeV	PYTHIA8	5 352 960.0	9 218 839
$\hat{p}_T \in [30, 50)$ GeV	—”—	9 928 000.0	11 498 448
$\hat{p}_T \in [50, 80)$ GeV	—”—	2 890 800.0	45 810 696
$\hat{p}_T \in [80, 120)$ GeV	—”—	422 800.0	77 694 296
$\hat{p}_T \in [120, 170)$ GeV	—”—	77 274.0	77 770 116
$\hat{p}_T \in [170, 300)$ GeV	—”—	18 810.0	11 539 879
$\hat{p}_T \in [300, \infty)$ GeV	—”—	1350.0	7 373 130
QCD ($b/c \rightarrow e + X$)			
$\hat{p}_T \in [15, 20)$ GeV	PYTHIA8	254 596.0	2 685 563
$\hat{p}_T \in [20, 30)$ GeV	—”—	328 999.93	10 964 108
$\hat{p}_T \in [30, 80)$ GeV	—”—	405 623.4	14 456 613
$\hat{p}_T \in [80, 170)$ GeV	—”—	38 104.43	13 561 051
$\hat{p}_T \in [170, 250)$ GeV	—”—	2635.8133	9 696 750
$\hat{p}_T \in [250, \infty)$ GeV	—”—	711.9259	9 757 009

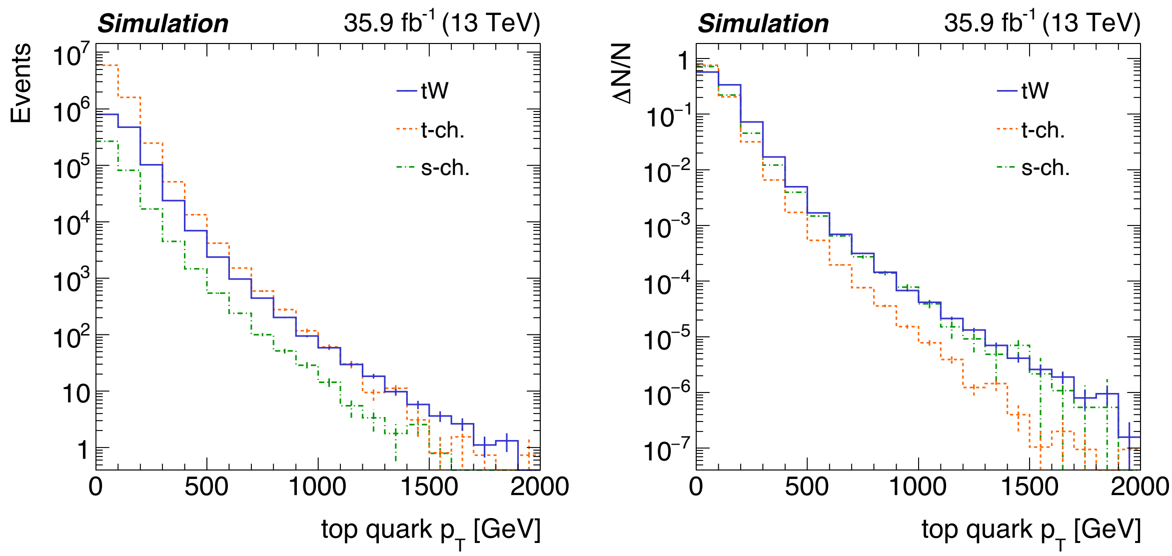

Figure 5.2.: Study of the top-quark p_T spectrum on MC generator level, comparing the three canonical channels of single top-quark production. The histogram on the left-hand side shows the expected numbers of events for 2016 data with inclusive decays and without any selection cuts applied. The histogram on the right-hand side, where each distribution is scaled to unit area, aids in a shape comparison. The depicted uncertainties include MC statistics only.

the boosted regime. The following arguments have been taken into consideration:

- The inclusive cross section of s-channel production is significantly smaller than for the other two channels. Hence, analyses of t-channel and tW production are more promising, considering limited statistics of the data set.

- Comparing the normalized shapes of the top-quark p_T spectra, s-channel and tW production are more suitable for measurements in the boosted regime than t-channel production since their spectra are significantly harder. Nevertheless, tW production is still more suitable than s-channel production due to the previous argument.

- Comparing expected differential cross sections, the higher the top-quark p_T, the more tW production catches up with t-channel production. At $p_T \gtrsim 1$ TeV, the two channels have approximately equal cross sections within statistical uncertainties of the MC prediction, not yet accounting for theoretical uncertainties of the modelling.

- In this analysis, the top quark is expected to decay hadronically and is reconstructed as one large boosted jet. Since electrons and muons have a very clean signature compared to hadronic jets, their presence enhances the event reconstruction significantly. Considering just the LO processes, the only single-top channel with the possibility of the presence of a lepton, which does not originate from the top quark but a secondary W boson, is the tW channel. Thus, tW production has a significant advantage over both t-channel (final state: $\overset{(-)}{\mathrm{q}}\mathrm{t}$) and s-channel (final state: $\mathrm{t\bar{b}}$) in terms of the event reconstruction.

Consequently, tW production is chosen as signal channel for this analysis. As anticipated by the last argument given, a lepton+jets event signature is chosen in which the top quark is expected to decay hadronically into one large collimated jet. Candidates of this jet must have been clustered by the HOTVR algorithm. In addition, the presence of exactly one lepton (muon or electron) and missing transverse momentum from the corresponding neutrino is required. The event selection in full detail is presented in Sect. 5.4.

Once the event selection is applied, the process with the most dominant contribution to all kinematic distributions is top-quark pair production. As a consequence, a certain analysis strategy has to be developed which is outlined in the following: In order to discriminate between tW and $t\bar{t}$ production, a multivariate analysis is performed in Chapter 6, employing boosted decision trees. The final differential measurements of cross sections as function of the top-quark p_T in W-associated single production are performed in Chapter 7: After the model prediction, predominantly consisting of contributions from tW and $t\bar{t}$ production, has been fitted to data, utilizing the discriminating response distributions of the previously trained boosted decision trees, a simplified unfolding procedure is employed to extract the differential cross section on parton level.

5.3 Background Processes

Several SM processes can lead to the same final-state event signature in the detector than the previously defined signal and are considered as background which the signal has to be separated from. Processes which have the same final state on parton level as the signal process are called *irreducible*; processes with parton-level final states different from the signal signature are called *reducible*. All processes which are relevant for this analysis are briefly discussed in the following.

Other top-quark production. Top-quark pair production is one of the most important backgrounds as in any single-top-quark analysis. The production of $t\bar{t}$ pairs has been described in Sect. 2.2.1. In this analysis, the semileptonic $t\bar{t}$ decay mode has the most dominant contribution in which one top quark decays into a large jet, as required from the signal process; the other top quark decays into a lepton, a neutrino leading to missing transverse energy, and an additional jet from the b quark. This additional b jet will be of particular importance for further discrimination between tW signal and $t\bar{t}$ background after the full event selection has been applied. The irreducibility of LO $t\bar{t}$ production w. r. t. NLO tW production has been discussed in Sect. 2.2.2.

Single top-quark t-channel and s-channel production also contribute as background. Though, their contribution to the overall background is very small in the end since the requirement of the presence of a lepton plus missing transverse energy and a boosted top jet at once can almost be considered as veto against other single-top processes than tW. This is reasoned by the fact that LO t- or s-channel production cannot feature leptons except they arise from the top quark.

Vector-boson production. The production processes of single W or Z bosons are relevant backgrounds in this analysis, with the production of W bosons being the second-most important background overall after $t\bar{t}$ production. Due to the presence of additional jets in the final states, the corresponding processes are referred to as "W+jets" or "Z+jets".

W+jets events in which the W boson decays leptonically and which feature associated heavy-flavour (b or c) quarks in the final state may be misidentified as tW signal events. The same will hold if final states feature e. g. $b\bar{b}$ pairs from gluon splitting. Although misidentification rates are relatively low in general, they still have a significant effect: The number of W+jets events passing the selection due to misidentification is counterbalanced by the inclusive cross section of vector-boson production which is some orders of magnitude larger than the ones of single top-quark production. For the same reason, even events with light-flavour quarks in the final state may contribute as relevant background.

Z+jets events are a less important background than W+jets since they always lead to the production of an even number of charged leptons or neutrinos what contradicts the signal signature. In this analysis, the Z+jets MC samples only include Drell-Yan processes ($Z \rightarrow \ell\bar{\ell}$). Signal-like Z+jets events need to have (at least) one unidentified lepton, reducing the probability of passing the event selection in the first place.

Diboson production. Another set of processes considered in this analysis is the associated production of two weak vector bosons (WW, WZ, or ZZ). The same arguments regarding misidentification as in single vector-boson production hold. Overall, the contribution of these processes is almost negligible despite that at least WW production can lead to signatures very similar to tW production.

QCD multi-jet production. The background with the largest production cross section is the production of multi-jet events via strong interactions. Aside from gluons, only light-flavour, c, or b quarks may participate in the hard process.

QCD events may feature leptons which are produced via the decay of heavy-flavour quarks or via in-flight decays of e. g. pions or kaons after hadronization. The QCD samples used for this analysis are enriched with single electrons or muons to account for these effects. Those leptons usually have low transverse momenta and, thus, most QCD events will be rejected by the event selection which requires a high-energetic lepton. Furthermore, misidentified leptons again play a role. For instance, hadrons reaching the muon chambers may be misidentified as muons.

One must consider that, due to the large QCD cross sections and the fact that the size of MC samples generally is limited, QCD samples have very large luminosity weights compared to samples of other processes with lower cross sections. After the event selection has been applied, only a small number of QCD events remains which is not any longer able to accurately describe kinematic distributions. Since the contribution of the QCD background is almost negligible at that point, the QCD samples are removed in the final steps of the analysis.

5.4 Event Selection

The final state of the LO signal process consists of one boosted top quark, decaying hadronically into one large jet clustered by the HOTVR algorithm, and a W boson, decaying into an electron or muon and the corresponding neutrino. Higher-order signal processes may include additional final-state quarks or gluons, leading to the presence of additional jets. The event selection, being based on this signature, is applied simultaneously on the data set and the presented MC samples. From now on, the terms *electron channel* or e+jets are used for the selection involving an electron and, equivalently, the terms *muon channel* or μ+jets for the selection involving a muon. The selection procedure is divided into three parts: Firstly, the preselection (Sect. 5.4.1) which aims at reducing the number of background events as much as possible while still keeping a relatively large fraction of signal events. Secondly, the application of top-tagging requirements on the HOTVR top-jet candidates (Sect. 5.4.2) what further reduces the number of kept events while increasing the likelihood for each remaining event to actually feature a boosted, hadronically decaying top quark. At last, the final measurement phase space is defined (Sect. 5.4.3). The presented event selection is inspired by Ref. 119.

5.4.1 Preselection

The individual steps of the preselection are listed in the following. For the muon channel, control distributions of some key variables after the preselection are shown in Fig. 5.4. Analogous distributions for the electron channel can be found in Fig. A.1 in Appendix A. The number of data events passing the preselection versus recorded integrated luminosity is shown in Fig. 5.3 for both the electron and muon channel.

Trigger requirements. The two analysis channels use different high-level trigger paths. In the electron channel, events are required to pass a boolean query, using the logical "or" combination of the `HLT_Ele27_WPTight_Gsf_v*` and `HLT_Ele115_CaloIdVT_GsfTrkIdT_v*` trigger, as recommended by the CMS collaboration for such single-electron analyses. These trigger require the presence of exactly one electron candidate with $p_T > 27$ GeV or $p_T > 115$ GeV, respectively, aside from other criteria. In the muon channel, events need to pass the `HLT_IsoMu24_v*` or `HLT_IsoTkMu24_v*` trigger, as recommended by the CMS collaboration for such single-muon analyses. Analogously, these trigger require the presence of exactly one isolated muon candidate with $p_T > 24$ GeV; the difference in these two trigger paths is found in the method used for the online reconstruction of the muon. Scale factors are applied to simulated events to account for differences in trigger efficiencies in MC and data.

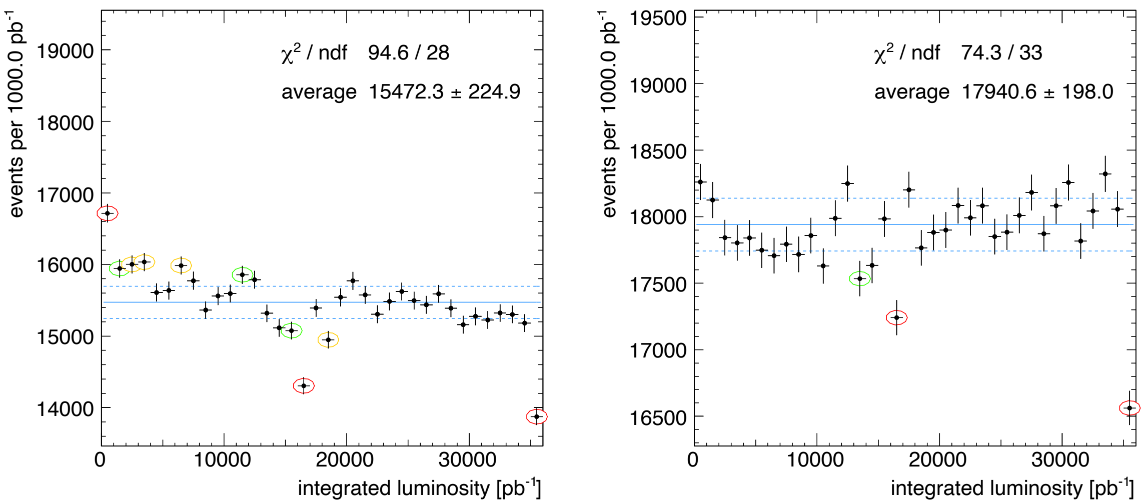

(a) e+jets **(b)** μ+jets

Figure 5.3.: Number of data events passing the preselection in the electron (left) and muon (right) channel as function of the integrated luminosity in bins of 1,000 pb^{-1}. Respectively, the constant solid blue line represents the average number of passing events with a standard deviation depicted by two dashed blue lines. Outliers are marked by circles and are not included in the average: Green (yellow, red) circles indicate a deviation of 3σ (4σ, 5σ or more) from the average. In both histograms, the strong outlier in the last bin from 35.0 fb^{-1} to 36.0 fb^{-1} is explained by the fact that only 35.87 fb^{-1} have been recorded in total. The difference between the averages of electron and muon channel are explained by different lepton trigger, reconstruction, and identification efficiencies.

Event cleaning and primary vertex. All reconstructed final-state physics objects which do not match the quality criteria described in Chapter 4 are removed from further consideration. In particular, only AK4 jets which fulfil $p_\mathrm{T} > 30$ GeV, $|\eta| < 2.4$, and the loose WP for PF jets [110] are considered in this analysis. The lepton identification criteria and requirements on HOTVR jets are described in the next selection steps.

Aside from this, each event needs to include at least one well-reconstructed primary vertex, i. e. it must be located close to the interaction point, requiring $\sqrt{x^2 + y^2} < 2$ cm and $|z| < 24$ cm, and the number of degrees of freedom in its reconstruction (strongly correlated with the number of tracks associated with that vertex) must be at least four. If there is more than one such primary vertex—what is most likely the case—, the vertex with the largest scalar sum of squared transverse momenta of associated tracks is interpreted as primary vertex and all others are treated as pile-up vertices [94].

Lepton requirements. In the electron (muon) channel, the presence of exactly one electron (muon) is required which fulfils the tight WP of identification criteria described in the previous chapter. In addition, this single lepton has to fulfil a kinematic threshold defined by its transverse momentum and the absolute value of its pseudorapidity with values $p_\mathrm{T} > 50$ GeV and $|\eta| < 2.4$, respectively. In case of the muon channel, the single muon furthermore has to pass a selection

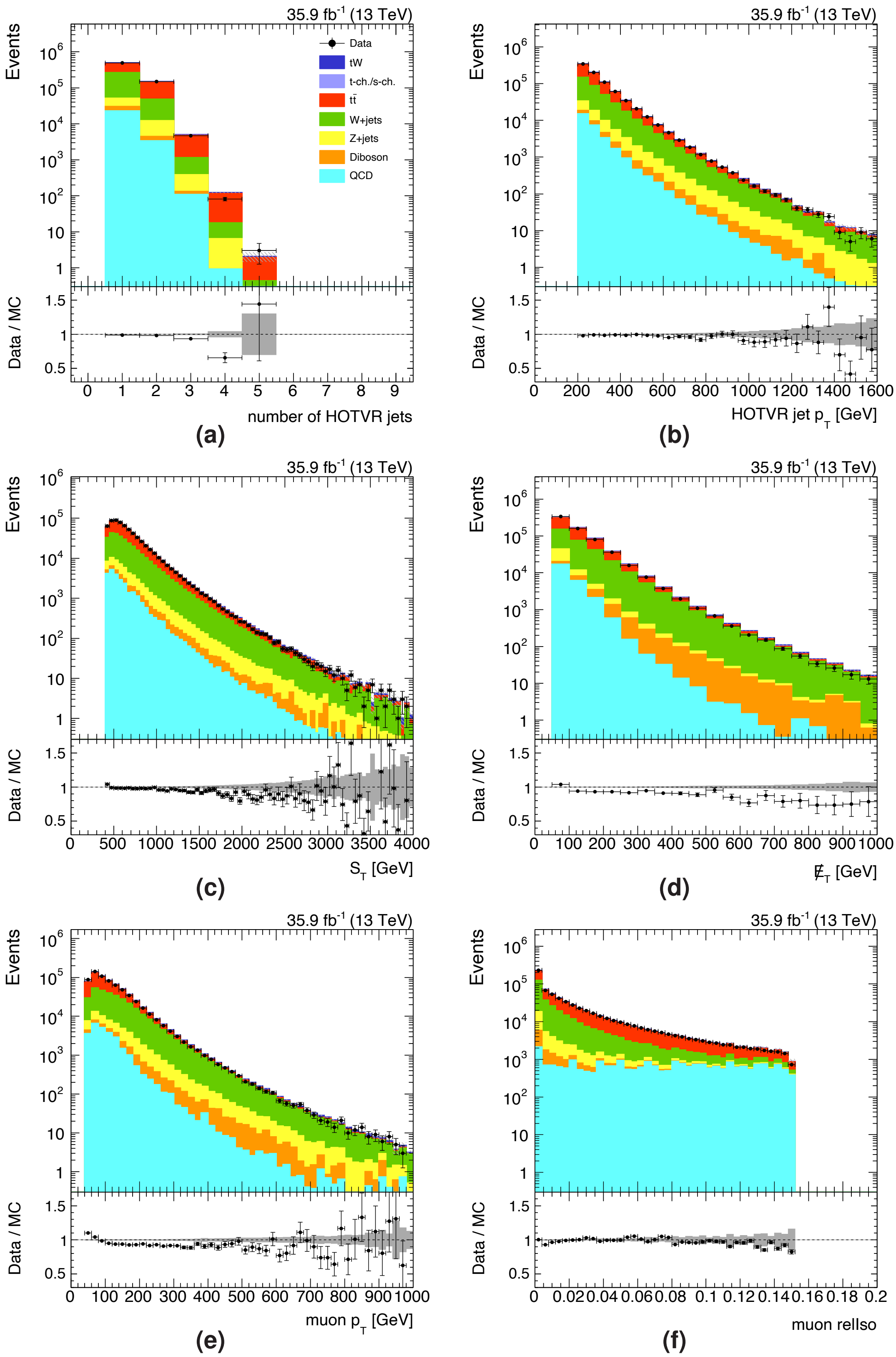

Figure 5.4.: Control distributions of the muon channel after the preselection described in Sect. 5.4.1. The **(a)** number of HOTVR jets, the **(b)** transverse momenta of all HOTVR jets, the **(c)** transverse activity, the **(d)** missing transverse energy, the **(e)** transverse momentum of the muon, and the **(f)** relative isolation of the muon (cf. Expr. 4.1) are shown. Analogous distributions for the electron channel can be found in Fig. A.1 in Appendix A. Uncertainties on the model prediction represent MC statistics only. The tW signal and other single-top processes are at the top of the histogram stack and, due to the logarithmic scale, barely visible.

cut on its relative isolation, given as $I_{\mathrm{rel}} < 0.15$ (cf. Expr. 4.1). Scale factors are applied on MC events to account for differences in reconstruction and identification efficiencies of leptons between data and simulation. For muons, an additional isolation scale factor is applied. For electrons, an isolation criterion is embedded into the identification WP.

In order to guarantee that there are no additional high-energetic charged leptons of other flavour which would contradict the signal signature, a respective veto is employed. In the electron (muon) channel, a veto is put on the presence of additional muons (electrons) fulfilling the loose (veto) WP with $p_{\mathrm{T}} > 30$ GeV and $|\eta| < 2.4$.

Missing transverse energy. Since the associated W boson is expected to decay into a lepton and a neutrino while most likely being highly boosted like the top quark, the presence of a significant amount of missing transverse energy in the event is required. The selection cut is defined to be $\not{E}_{\mathrm{T}} > 50$ GeV. Together with the previous high-p_{T} single-lepton requirement, this cut is able to reject a large amount of QCD multi-jet background events which mostly feature soft secondary leptons and very rarely neutrinos as described in the previous section.

Transverse activity. Since this study aims at highly boosted top quarks, the overall event topology is required to be boosted as well. Since top quark and associated W boson can in most cases be expected to be in a back-to-back position to each other, a cut on the transverse activity S_{T} is reasonable. It is defined as the scalar sum over the transverse momenta of all electrons, muons, AK4 jets, and the missing transverse energy, reading

$$S_{\mathrm{T}} = \not{E}_{\mathrm{T}} + \sum_{\mathrm{e,\,\mu,\,AK4\;jets}} p_{\mathrm{T},i}\,. \tag{5.2}$$

The selection cut is set to be $S_{\mathrm{T}} > 400$ GeV.

HOTVR jets. Each event is required to feature at least one jet clustered by the HOTVR algorithm which fulfils $p_{\mathrm{T}} > 200$ GeV and $|\eta| < 2.5$. After the preselection, these HOTVR jets undergo a set of additional identification requirements, as presented in the next section, to increase their likelihood to originate from top quarks since, so far, they may as well originate from any other hadronically decaying final-state object with significant energy (e. g. the associated W boson which may decay hadronically in contrast to the signal definition). HOTVR jets which do not fulfil these kinematic thresholds are no longer considered as such for this analysis.

In addition to the scale factors presented alongside the selection criteria, simulation needs to be adjusted further. In order to describe the true number of interactions in a collision event as accurately as possible, a pile-up re-weighting is applied to each MC event in which this number is a known parameter. Corresponding correction factors are calculated from the integrated luminosity and the minimum-bias cross section in proton-proton collisions at $\sqrt{s} = 13$ TeV which

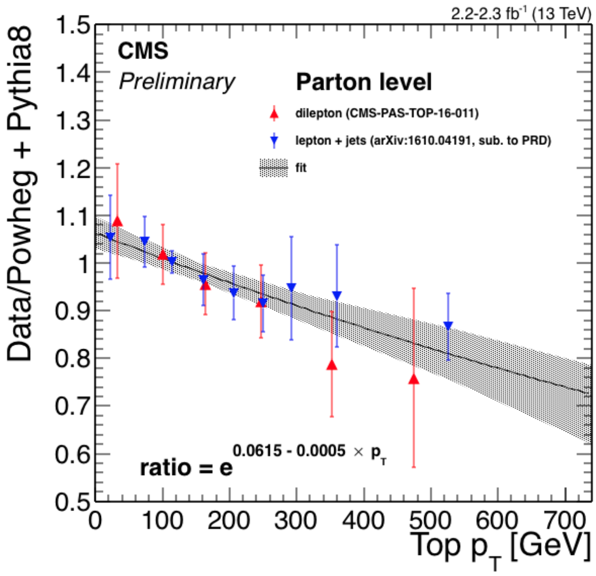

Figure 5.5.: Correction factors for the re-weighting of the true top-quark p_{T} in simulated $\mathrm{t\bar{t}}$ events. The data-over-simulation ratio fit with an exponential ansatz is based on results from Ref. 120, 121. Taken from Ref. 123.

is equal to $\sim$ 69 mb. Furthermore, a re-weighting of the transverse momentum of top quarks in simulated $\mathrm{t\bar{t}}$ events has to be done. The difference in top-quark p_{T} spectra of $\mathrm{t\bar{t}}$ events between data and simulation has been observed in many published analyses of CMS [120–122] and is interpreted as a mis-modelling effect which has to be corrected for. Data shows that the true top-quark p_{T} spectrum is slightly softer than the simulated one. Fig. 5.5 shows the correction factors which are applied to the POWHEG+PYTHIA8 MC samples of $\mathrm{t\bar{t}}$ production used in this thesis. A priori, it stands to reason that a similar mis-modelling might be present in the simulation of single top-quark production. However, no essential investigations in that respect have been performed yet, at least not for the boosted kinematic regime. A future analysis related to the work in this thesis might gather new intelligence.

Investigating the control distributions shown in Fig. 5.4, one can make the following observations: The number N_{HOTVR} of HOTVR jets in data significantly deviates from simulation for $N_{\mathrm{HOTVR}} = 4$ (Fig. 5.4a). An explanation is given by the inaccurate modelling of events with high jet multiplicities [120]. In addition, a trend in the $\not{E}_{\mathrm{T}}$ distribution (Fig. 5.4d) and, conclusively, in the S_{T} distribution (Fig. 5.4c) is observed in the ratio between data and simulation. A similar trend is observed in the muon p_{T} distribution (Fig. 5.4e) which also features an excess at $p_{\mathrm{T}} \lesssim 100$ GeV. An explanation for this excess is given by the QCD multi-jet contribution in the corresponding bins since jets including muons from hadronic decays are not sufficiently well described in simulation [119]. Despite these discrepancies, good agreement between data and simulation is observed.

5.4.2 Top-Tagging Requirements

As a next step, top-tagging requirements are applied onto all reconstructed HOTVR jets, using the default values of the standard cut-based HOTVR top-tagging criteria [111]. These criteria, which are predominantly based on selection cuts on jet substructure variables, are summarized in the following:

- The leading sub-jet, i. e. the sub-jet with the largest transverse momentum out of all sub-jets, is required to only contribute with at most 80 % to the total HOTVR jet p_{T}. This requirement, formulated as $f_{p_{\mathrm{T}}} = p_{\mathrm{T},1}/p_{\mathrm{T}} < 0.8$, is motivated by the fact that the three decay products of the top quark on parton level are expected to most likely carry equally distributed fractions of the overall transverse momentum.

- The number of sub-jets is required to be equal or greater than three. This increases the probability of finding top quarks whose decay products on parton level are fully merged with the sub-jets on reconstruction level. Additionally, a fair amount of QCD multi-jet events gets rejected by this criterion.

- The jet mass, which is calculated as the invariant mass of all clustered pseudojet four-momenta, is required to be in the interval $140 < m_{\mathrm{jet}}$ [GeV] < 220 which covers the top-quark mass of approximately 173 GeV.

- The minimum pairwise invariant mass of two of the three leading sub-jets has to fulfil $m_{ij} > 50$ GeV. For instance, this criterion is expected to increase the likelihood for the presence of a W boson from the top-quark decay.

In addition to these standard top-tagging criteria of HOTVR, a cut on the variable τ_3/τ_2 is imposed. The variable τ_N is referred to as *N-subjettiness* [124] and measures the likelihood of the hypothesis that a jet consists of up to N sub-jets. As formula, it reads

$$\tau_N = \frac{1}{d_0} \sum_k p_{\mathrm{T},k} \min\left(\Delta R_{1,k}, \Delta R_{2,k}, \ldots, \Delta R_{N,k}\right) \tag{5.3}$$

where $\Delta R_{i,k}$ measures the distance between the jet axis of a hypothetical sub-jet component i and the jet constituent k with transverse momentum $p_{\mathrm{T},k}$. The normalization factor d_0 reads

$$d_0 = \sum_k p_{\mathrm{T},k} R_0 \tag{5.4}$$

where R_0 is the jet radius parameter as introduced in Expr. 4.3. Values of τ_N may range between 0 and 1 and values close to 0 support the hypothesis whereas values close 1 reject it, meaning that the jet likely consists of more than N sub-jets. Jets originating from top quarks most likely consist of three sub-jets ($\tau_3 \gtrsim 0$) and significantly less likely of two sub-jets ($\tau_2 \lesssim 1$), resulting into $\tau_3/\tau_2 < 1$. Here, a cut value of $\tau_3/\tau_2 < 0.56$ is chosen.

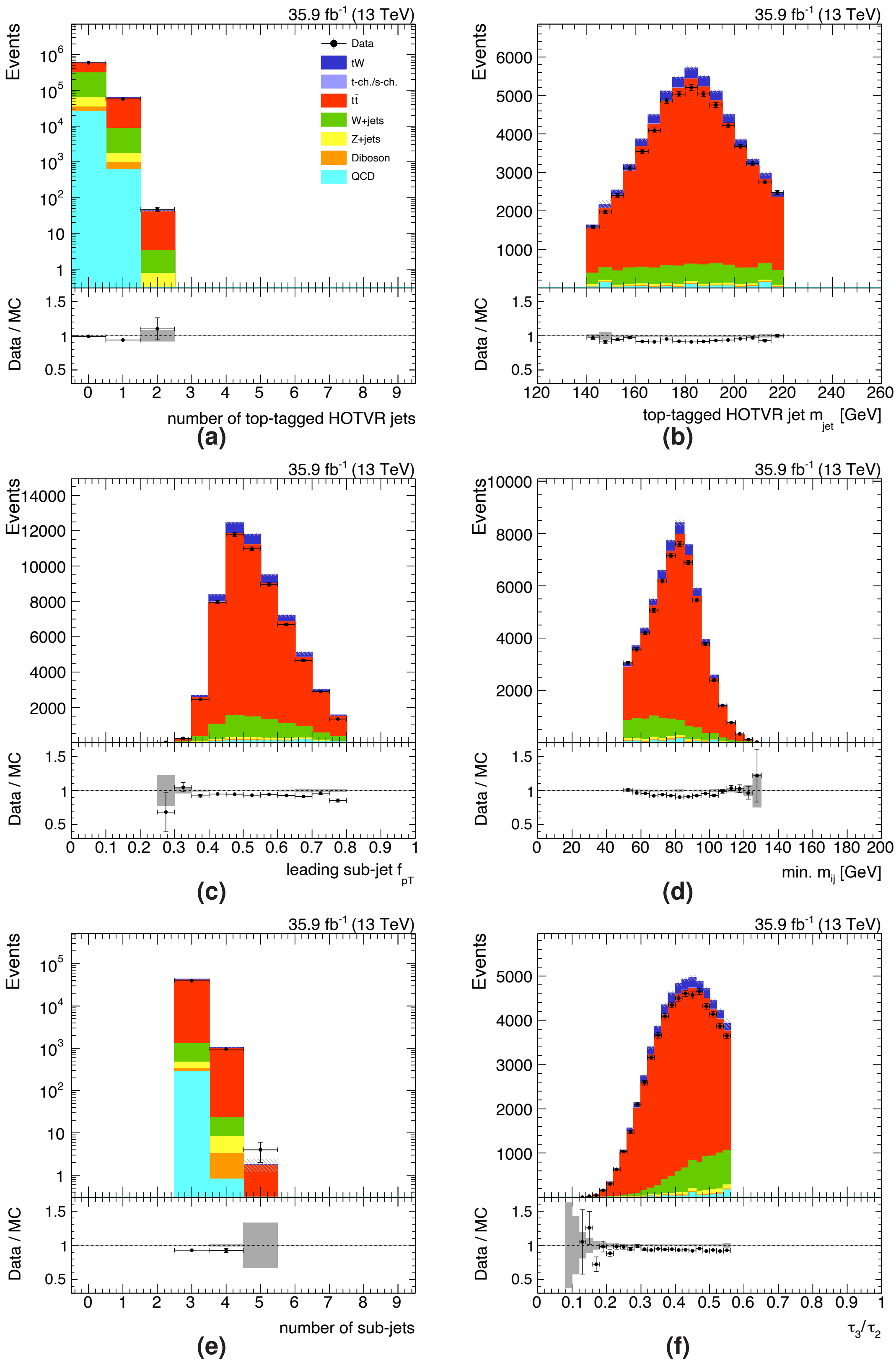

Figure 5.6.: Control distributions of top-tagging variables in the muon channel as introduced in Sect. 5.4.2. The **(a)** number of top-tagged HOTVR jets is shown for all events passing the preselection. For events with exactly one top-tag, the following variables of the top-tagged HOTVR jet are shown: The **(b)** jet mass, the **(c)** p_T fraction of the leading sub-jet, the **(d)** minimum pairwise invariant mass of the three leading sub-jets, the **(e)** number of sub-jets, and the **(f)** N-subjettiness ratio. Analogous distributions for the electron channel can be found in Fig. A.2 in Appendix A. Uncertainties on the model prediction represent MC statistics only.

As a last criterion, the azimuthal distance between the top-jet candidate and the reconstructed lepton must fulfil $\Delta\phi(\mathrm{t}, \ell) > \pi/2$ since top quark and associated W boson are expected to have a back-to-back signature.

Control distributions for events with HOTVR jets which fulfil these top-tagging criteria are shown in Fig. 5.6 for the muon channel. Again, analogous distributions for the electron channel can be found in Fig. A.2 in Appendix A. The first observation which one can make is that there is a general offset between data and simulation of about 8 %. This is explained by a difference in top-tagging efficiency between data and simulation which has to be corrected for by a scale factor. However, no such scale factors are available yet for HOTVR. Since fits are performed at the end of the analysis, this discrepancy may be ignored, assuming that the contributions of individual processes remain unaffected. In the future, scale factors need to be implemented of course. Aside from this, one can observe a peak in the HOTVR jet mass (Fig. 5.6b) around the top-quark mass what validates the functionality of HOTVR. A shift to slightly higher values than 173 GeV is explained by the fact that remaining pile-up effects and soft radiation increases the jet mass. The minimum pairwise mass (Fig. 5.6d) shows a peak at the mass of the W boson ($\sim$ 80.3 GeV) from the top-quark decay.

5.4.3 Full Selection

After the preselection, the overall contribution of tW production in simulation is 3.44 % (3.50 %) for the electron (muon) channel. The two main backgrounds are $\mathrm{t\bar{t}}$ and W+jets production with a contamination of 44.42 % (47.25 %) and 37.39 % (38.18 %), respectively, in the electron (muon) channel. In order to increase the signal-to-background ratio to be able to perform a valuable measurement, the signal has to be further discriminated from the remaining backgrounds. In the next chapter, a multivariate approach is chosen to achieve this. Beforehand, the final phase space is defined by two additional selection criteria:

- Exactly one top-tagged HOTVR jet must be present.
- At least one b-tagged AK4 jet must be present, using the identification criterion imposed by the medium WP of the CSVv2 algorithm.

Scale factors are applied to MC events to account for different b-jet identification efficiencies and mis-tag rates in data and simulation. As seen in Fig. 5.6a, the top-tag selection cut reduces the overall number of events significantly. It puts a strong veto on W+jets production which gets reduced by 97.32 % (97.27 %) in the electron (muon) channel in comparison to the initial preselection yield. The second cut on the number of b-tags further rejects 87.35 % (87.74 %) of the remaining W+jets events, as can be seen in Fig. 5.7.

The two dominant processes are now $\mathrm{t\bar{t}}$ and tW production. After the top-tag requirement, tW contributes with 5.41 % (5.17 %) and, after additionally requiring b-tags, with 5.48 % (5.20 %). As can be concluded from these numbers, the b-tag requirement does not increase the fraction of

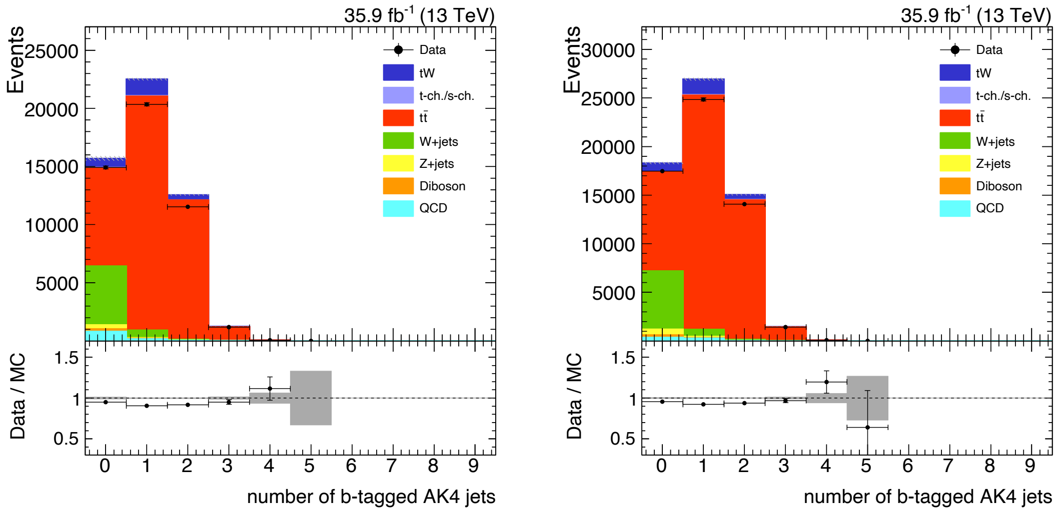

(a) e+jets **(b)** μ+jets

Figure 5.7.: Events sorted by the number of b-tagged AK4 jets after the requirement for the presence of exactly one top-tagged HOTVR jet. Distributions for both the electron (left) and the muon (right) channel are shown. Requiring the presence of at least one b-tag reduces the W+jets contamination significantly. Uncertainties on the model prediction represent MC statistics only.

tW production and its significance[1] actually slightly drops from 11.72 (12.23) to 9.99 (10.40). However, the presence of b-tagged AK4 jets allows for the definition of variables with strong discrimination power between tW and $t\bar{t}$ production as can be seen in the next chapter.

The now defined phase space is divided into two categories: The `1t1b` category, including events with exactly one b-tagged AK4 jet, and the `1t2b+` category, including events with two or more b-tagged AK4 jets. This categorization aids in the performance optimization of the boosted decision trees which are to be trained in the next chapter. Control distributions of the top-jet transverse momentum, which is the target variable of the differential cross-section measurements which are to be performed, are shown in Fig. 5.8 for all four phase spaces.

[1]The signal significance is defined as $S/\sqrt{S+B}$ where S represents the absolute number of signal events and B the absolute number of all background events which are leftover according to the simulated prediction.

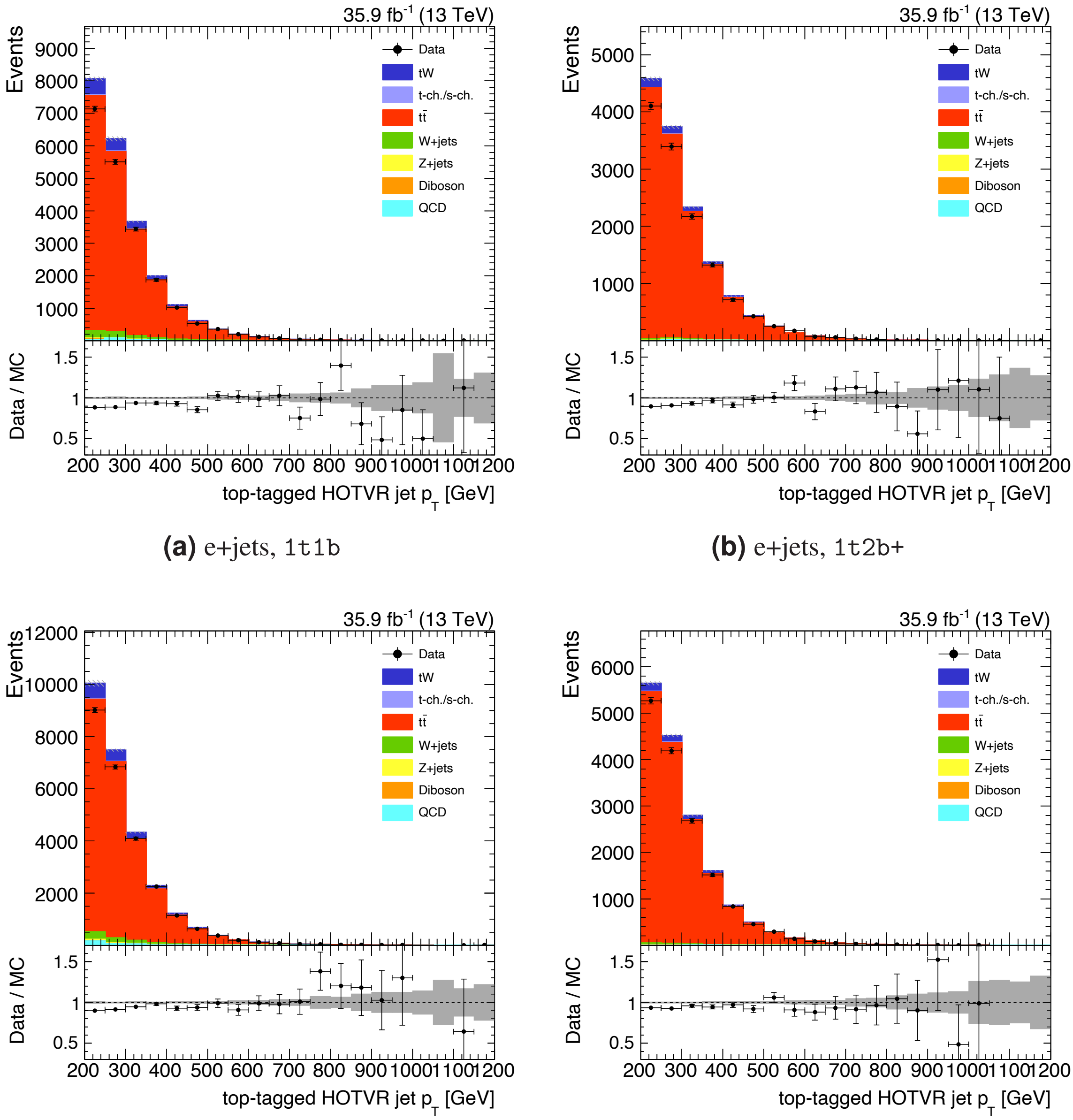

(a) e+jets, `1t1b` **(b)** e+jets, `1t2b+`

(c) μ+jets, `1t1b` **(d)** μ+jets, `1t2b+`

Figure 5.8.: Distributions of the transverse momentum of the top-tagged HOTVR jet in all four phase spaces as defined in Sect. 5.4.3. Uncertainties on the model prediction represent MC statistics only. As mentioned in Sect. 5.4.2, no top-tagging scale factors are applied what results in a slight offset between data and simulation.

5.5 Signal Event Reconstruction

In the following chapter, certain variables are used in the training of multivariate algorithms. A few of these are based on the kinematics of the neutrino emerging from the decay of the associated W boson of tW events. Since the neutrino cannot be detected and, hence, its kinematics cannot be measured, it must be reconstructed indirectly from other event information. In order to reconstruct the four-momentum $p_\mu(\nu)$ of the neutrino, the missing transverse energy $\not{E}_\mathrm{T}$ and the kinematics of the charged lepton are exploited.

It is assumed that the only source of missing transverse energy is given by the neutrino escaping the detector. Thus, the relation

$$p_\mathrm{T}(\nu) = \not{E}_\mathrm{T} \tag{5.5}$$

holds where $p_\mathrm{T}(\nu) = \sqrt{p_x^2(\nu) + p_y^2(\nu)}$. Both transverse components $p_x(\nu)$ and $p_y(\nu)$ of the neutrino momentum are known from the missing transverse energy. It is further assumed that the W boson, which the neutrino emerged from, was on-shell. Thus, the relation

$$p_\mu^2(\mathrm{W}) = M_\mathrm{W}^2 = \left(p_\mu(\ell) + p_\mu(\nu)\right)^2 \tag{5.6}$$

holds as well. The longitudinal component $p_z(\nu)$ of the neutrino momentum can be expressed by a quadratic equation which has the following solutions:

$$p_z^\pm(\nu) = \frac{\alpha p_z(\ell)}{p_\mathrm{T}^2(\ell)} \pm \sqrt{\frac{\alpha^2 p_z^2(\ell)}{p_\mathrm{T}^4(\ell)} - \frac{E^2(\ell)\,p_\mathrm{T}^2(\nu) - \alpha^2}{p_\mathrm{T}^2(\ell)}} \tag{5.7}$$

where $\alpha = M_\mathrm{W}^2/2 + p_\mathrm{T}(\ell)\,p_\mathrm{T}(\nu)\cos\angle(\ell,\nu)$. In these equations, $p_\mu(\ell)$ and $p_\mu(\nu)$ are the four-momenta of the lepton and the neutrino, respectively. Expr. 5.7 can have zero, one, or two real solutions for $p_z(\nu)$. If the solution is complex, its real part is taken as value of $p_z(\nu)$.

6 Multivariate Analysis: Training and Testing of Boosted Decision Trees

After applying the event selection, which has been presented in Chapter 5, the data set is still contaminated with a large $t\bar{t}$ background. The ratio between the single-top signal and its background is much larger than in a comparable $t\bar{t}$ measurement [68]. In order to increase this ratio and the statistical significance of the signal process tW, a multivariate algorithm (MVA) is used. MVA methods which are commonly used in high-energy physics are artificial neural networks (ANN), likelihood functions (LF), and boosted decision trees (BDT) [125]. All of these represent different approaches of machine learning. In this thesis, the BDT method is chosen which is known for its "out-of-the-box" functionality and its fairly simple working principle compared to some other methods while still providing high performance.

In Sect. 6.1, an introduction to the working principle behind BDTs is given. In Sect. 6.2, the training procedure in this analysis is documented and the trained BDTs are validated. Estimations of the best cut values on the BDT response distributions w. r. t. an optimization of the signal significance are performed in Sect. 6.3. The implementation of BDTs into this analysis has been done with the *Toolkit for Multivariate Analysis* (TMVA) [126].

6.1 Introduction to Boosted Decision Trees

In Sect. 6.1.1, the working principle of BDTs is explained and the associated terminology is introduced. In Sect. 6.1.2, the principle of *overtraining* is introduced which represents a major concern in machine learning and requires special care.

6.1.1 General Description

A decision tree is a tree-structured classifier, represented as a sequence of binary decisions. An example for such a tree is given in Fig. 6.1. Repeated boolean decisions (true/false) are taken on one specific input variable at a time until a stop criterion is fulfilled: Starting from the root node, the tree grows successive layers of further binary nodes. At each node, a variable is selected and a corresponding cut value is applied which is required to maximize the separation between signal and background events. To obtain these optimal values, the decision tree has to be trained in the first place, using distinct samples which are marked as definite signal and background.

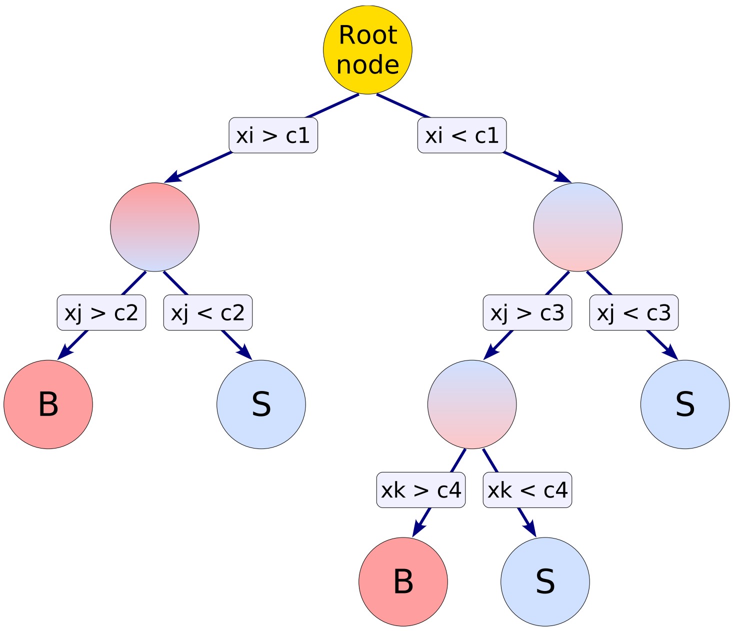

Figure 6.1.: Schematic view of a decision tree. Starting from the root node, consecutive binary decisions are performed, using the boolean response of certain variables $x_{i,j,k}$ w. r. t. associated cut values $c_n, n \in \{1,2,3,\dots\}$. These cut values must be obtained from a training procedure in the first place in which they are required to provide the best separation between signal and background events. The same variable may be used in several nodes while others might not be used at all. The bottom nodes (leaves) are classified as signal-like (S) or background-like (B) depending on the majority of events which end up in each of them. Taken from Ref. 126.

The entire phase space spanned by all considered variables is ultimately split up into multiple regions (hypercubes) which correspond to the final nodes (*leaves*). Depending on the majority of training events from the signal samples which end up in the individual regions, each region is eventually classified as either signal-like or background-like. After this training procedure, the decision tree may be applied to real data events which then are classified as either signal or background depending on the individual outcome.

In this respect, decision trees are similar to rectangular cuts. However, simple cut-based analysis methods are able to select only one hypercube out of the complete phase space whereas a decision tree is able to split up the entire phase space into multiple hypercubes, each of which is classified as either signal-like or background-like.

Since a single decision tree is very limited in its discrimination power compared to other MVA methods and is thus considered as a weak classifier, several single trees can be combined to a *forest* to achieve better performance. This extension of the above presented concept leads to a significantly stronger classifier. The growing of such an advantageous forest, which may consist of hundreds of individual trees, is called *boosting*. The trees in a forest are trained sequentially. When generating a new tree, training events are assigned with a larger weight if they had been misclassified previously. In addition, each tree is assigned a boosting weight. In the end, a BDT assigns a classification score to each event which is calculated as the weighted average of each tree outcome, using the boosting weights: Each tree classifies an event as either signal-like $(+1)$ or background-like (-1), leading to a score in the interval $[-1, +1]$. The score corresponds to the likelihood of being signal or background.

6.1.2 Overtraining

One of the major concerns for any multivariate algorithm is an effect known as *overfitting* or *overtraining*. It appears when the algorithm does not generalize during the training procedure. I. e., instead of learning to discriminate between signal and background according to a general boundary that applies across all randomly composed sub-samples of the same phase space, the algorithm begins to learn from statistical fluctuations which appear in the specific training samples chosen. When applied to other samples which are statistically independent from the training samples, the overtrained algorithm systematically misclassifies signal events as background and vice versa within the phase-space regions around the optimal boundary. A visualization of overtraining is provided in Fig. 6.2.

BDTs are known to be relatively robust w. r. t. possible overtraining. However, one cannot choose their configurations carelessly. In order to estimate overtraining effects after the training procedure with certain configuration settings, the BDT response in the training sample is compared to the BDT response of a statistically independent testing sample. There are several ways to quantify the agreement between the responses of two samples. One approach, which is used in this analysis, is the modified *Kolmogorov-Smirnov* (KS) test [127] which is a goodness-of-fit test similar to a χ^2-test. The KS test returns a test statistic which is expected to be evenly distributed between 0 and 1 in case of good agreement between both response distributions. If the KS test returns a value very close to 0 or very close to 1, overtraining might be present.

6.2 Training and Testing

The BDTs are trained on the MC samples of tW production as signal sample and of $\mathrm{t\bar{t}}$ production as background sample to achieve the best $\mathrm{t\bar{t}}$ rejection efficiency. In fact, only half of all MC events from both tW and $\mathrm{t\bar{t}}$ samples are utilized as training events. The respective other half is reserved as statistically independent testing sample.

The presence of b-tagged AK4 jets allows for the definition of some highly discriminating variables between tW and $\mathrm{t\bar{t}}$ production. The choice of these variables is optimized for the case that there are at least two b-tags present in the event. However, those variables can also be used in case that there is only one b-tag while still achieving good discrimination power. In order to optimize the training for the phase space in which at least two b-tags are present, the phase-space division into the `1t1b` and `1t2b+` category, as introduced in Sect. 5.4.3, with individually trained BDTs stands to reason. In the training and testing, no distinction between electron and muon channel is made since the input variables described in Sect. 6.2.1 are independent from

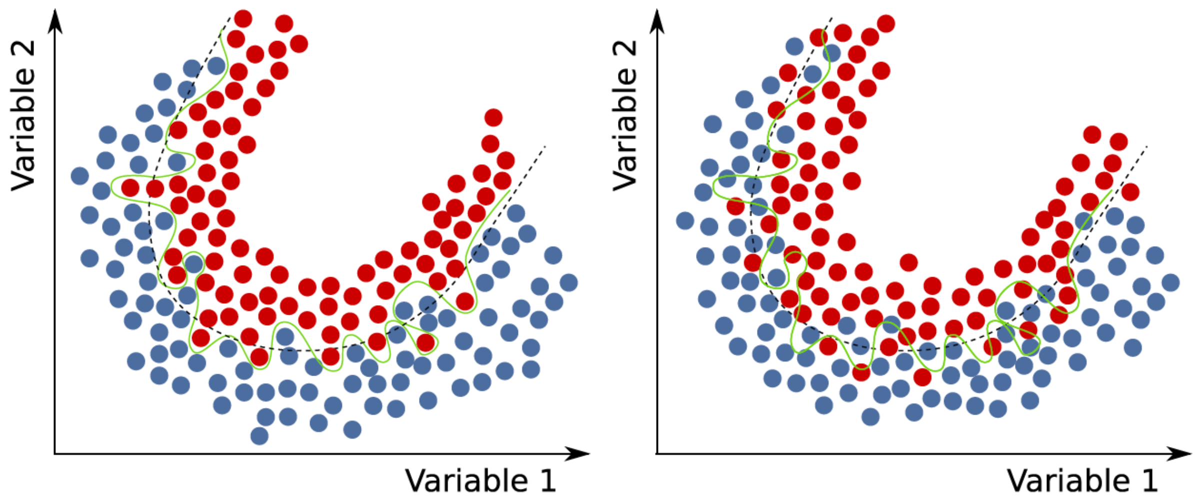

Figure 6.2.: Visualization of overtraining. Two statistically independent distributions of signal (red) and background (blue) events in a 2D diagram spanned by two input variables are shown. The left diagram represents the training sample, the right diagram represents the testing sample. The dashed line represents the optimal decision boundary which ignores statistical fluctuations in the transition region between signal-dominated and background-dominated areas. The green solid line represents an overtrained decision boundary obtained from the training sample. When this boundary is applied to the testing sample, signal events in the transition region are systematically misclassified as background and vice versa. Taken from Ref. 58.

lepton flavour and no differences between the electron and muon channel are motivated by the underlying physics. Small differences due to different reconstruction of electrons and muons are ignored. Therefore, a total number of two BDTs is trained.

The configuration options (*hyperparameters*) for the BDT training are given in Sect. 6.2.2. In Sect. 6.2.3, the results of the training procedures are presented and the resulting BDTs are validated. In Sect. 6.2.4, BDTs are applied to control regions as cross check.

6.2.1 Selection of Input Variables

In this study, many possible variables have been tested for their discrimination power. Some of them exploit the presence of b jets what has motivated the phase-space definition in Sect. 5.4.3. NLO tW processes may likely feature additional b quarks with the most prominent examples given in Fig. 2.7. The b jet arising from it is likely found in the forward region. In contrast, the b jet arising from the b quark from the leptonically decaying second top quark in $t\bar{t}$ events is basically restricted to be found in the hemisphere opposite to the hadronically decaying top quark. A visualization comparing boosted $t\bar{t}$ and tW event topologies with two b quarks/jets is shown in Fig. 6.3. For both $t\bar{t}$ and tW, another b-tagged AK4 jet may likely be found within the top-tagged HOTVR jet. In the `1t2b+` category, tW events likely are such NLO processes with two final-state b quarks. In order to identify the b jet which corresponds to the additional b quark in case of tW or to the b quark from the leptonically decaying top quark in case of $t\bar{t}$, all b-tagged AK4 jets within an event are considered and the one with the largest R-distance to

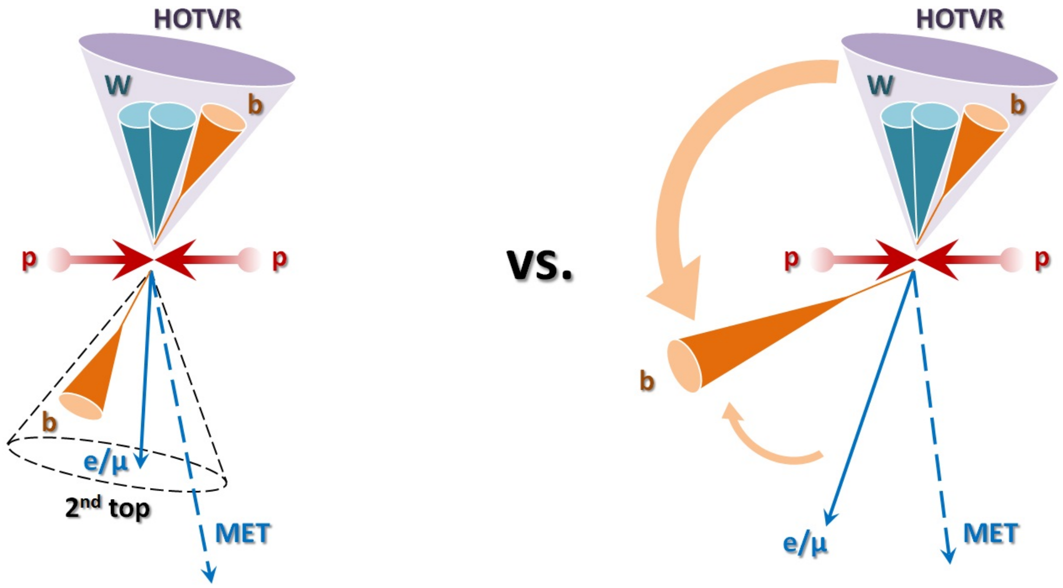

Figure 6.3.: Visualization of boosted LO $t\bar{t}$ (left) versus boosted NLO tW (right) events.

the jet axis of the top-tagged HOTVR jet is chosen; this b jet is referred to as the *identified* b jet in the following.

The input variables used for the BDT training are:

- $\Delta\phi(\ell, \mathrm{b})$: Azimuthal distance between the lepton and the jet axis of the identified b jet.
- $\Delta\phi(\mathrm{t}, \mathrm{b})$: Azimuthal distance between the jet axes of the top-tagged HOTVR jet and the identified b jet.
- $\Delta\phi(\ell, \mathrm{jet})$: Azimuthal distance between the lepton and the jet axis of the closest AK4 jet, regardless of being tagged or untagged. The closest AK4 jet is identified to be the one with the smallest R-distance to the lepton.
- $\eta(\ell)$: The pseudorapidity of the lepton.
- $p_{\mathrm{T}}(\ell)$: The transverse momentum of the lepton.
- $m_{\ell\nu\mathrm{b}}$: The invariant mass of the lepton, the reconstructed neutrino (cf. Sect. 5.5), and the identified b jet. For $t\bar{t}$, a sharp peak at the top-quark mass is expected since $m_{\ell\nu\mathrm{b}}$ likely represents the mass of the leptonically decaying top quark. For the `1t2b+` category, this peak is definite whereas, for the `1t1b` category, a combinatorial background generates a shoulder to slightly higher values. For tW, no mass peak is expected.
- $p_{\mathrm{T}}(\mathrm{W})$: The transverse momentum of the W boson reconstructed from the lepton and the neutrino.
- p_{T} balance: The balance between the transverse momenta of the top-tagged HOTVR jet,

$p_{\mathrm{T}}(\mathrm{t})$, and of the (associated) W boson, $p_{\mathrm{T}}(\mathrm{W})$. The p_{T} balance is defined as

$$\frac{p_{\mathrm{T}}(\mathrm{W}) - p_{\mathrm{T}}(\mathrm{t})}{p_{\mathrm{T}}(\mathrm{t})}. \tag{6.1}$$

For tW, values are expected to peak close to zero due to momentum conservation in the back-to-back system of top quark and associated W boson. For $\mathrm{t\bar{t}}$, this system is imbalanced due to the fact that the reconstructed W boson is not produced in association with the hadronically decaying top quark but comes from the decay of the second top quark. Thus, the p_{T} balance of $\mathrm{t\bar{t}}$ events shows a slight shift to negative values.

- For the `1t2b+` category, the number of b-tags is also considered as input variable.

The distributions of all input variables in the tW signal and $\mathrm{t\bar{t}}$ background training samples are shown in Fig. 6.4 and Fig. 6.5 for the `1t1b` and `1t2b+` category, respectively. Some of these variables obviously have high correlations as, for instance, $p_{\mathrm{T}}(\ell)$, $p_{\mathrm{T}}(\mathrm{W})$, and the p_{T} balance. Also, $\Delta\phi(\ell,\mathrm{b})$ and $\Delta\phi(\mathrm{t},\mathrm{b})$ are significantly anti-correlated. However, BDTs are able to handle highly correlated input variables and usually do not overtrain due to those. Linear correlations between all input variables are shown in Fig. 6.6 for both the `1t1b` and the `1t2b+` category, split up into correlations within the signal training sample and the background training sample, respectively.

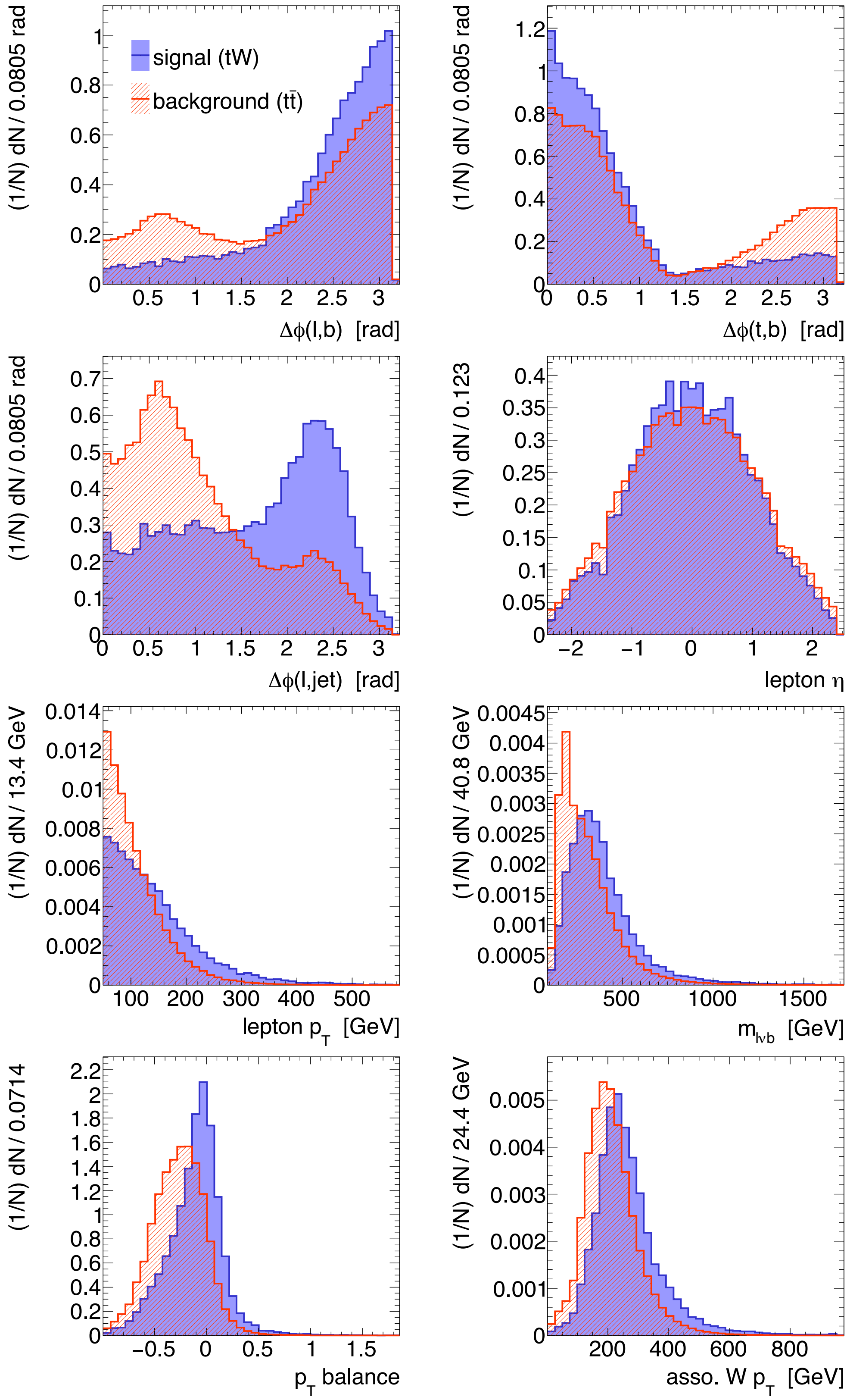

Figure 6.4.: Input variables for the BDT training in the `1t1b` category. The e+jets and μ+jets training samples are stacked together. The superimposed distributions of tW signal (blue) and $t\bar{t}$ background (red) samples are normalized by their respective integral.

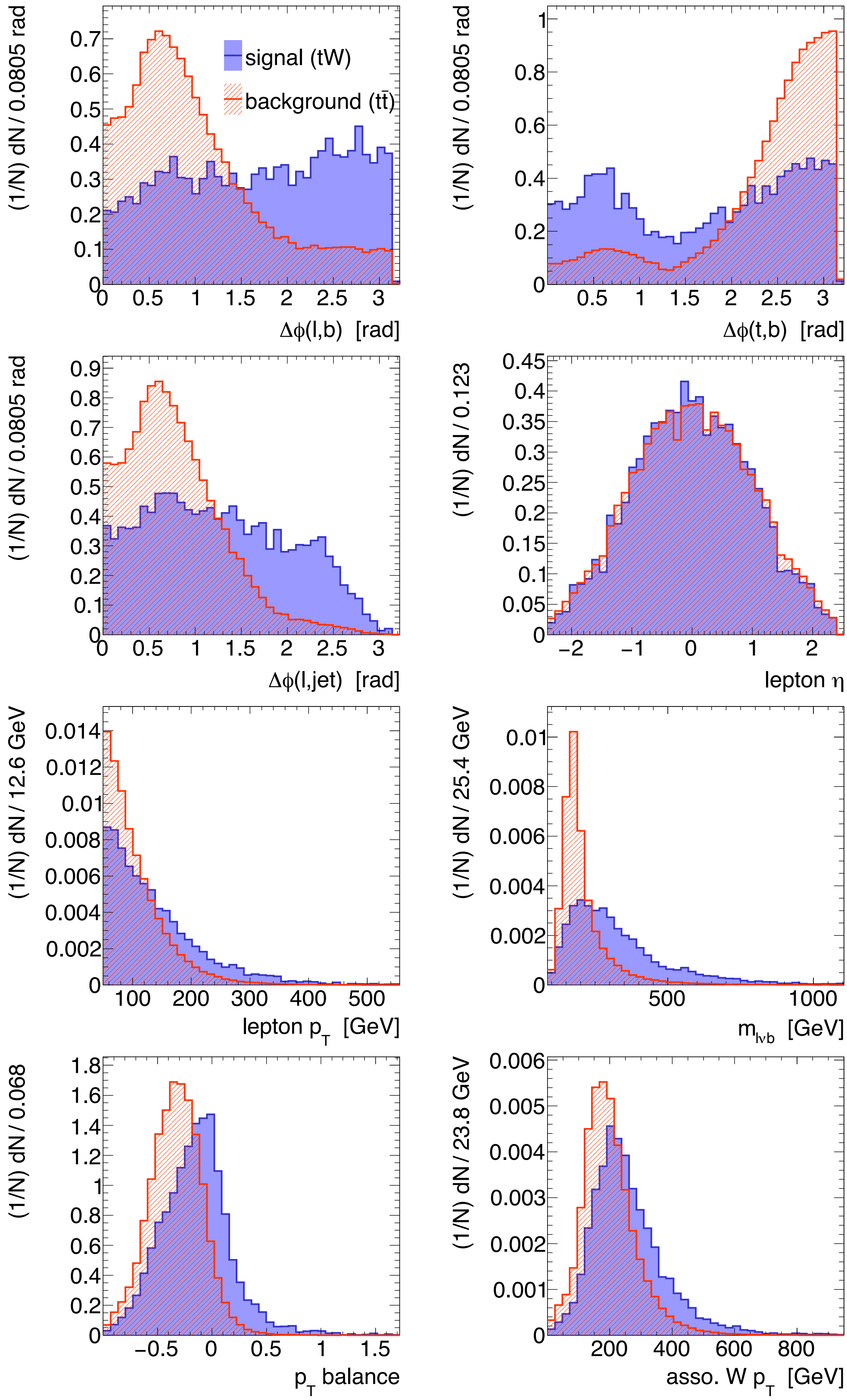

Figure 6.5.: Input variables for the BDT training in the `1t2b+` category. The e+jets and μ+jets training samples are stacked together. The superimposed distributions of tW signal (blue) and $t\bar{t}$ background (red) samples are normalized by their respective integral. The only variable not shown is the number of b-tags which has no significant discrimination power, cf. Fig. 5.7.

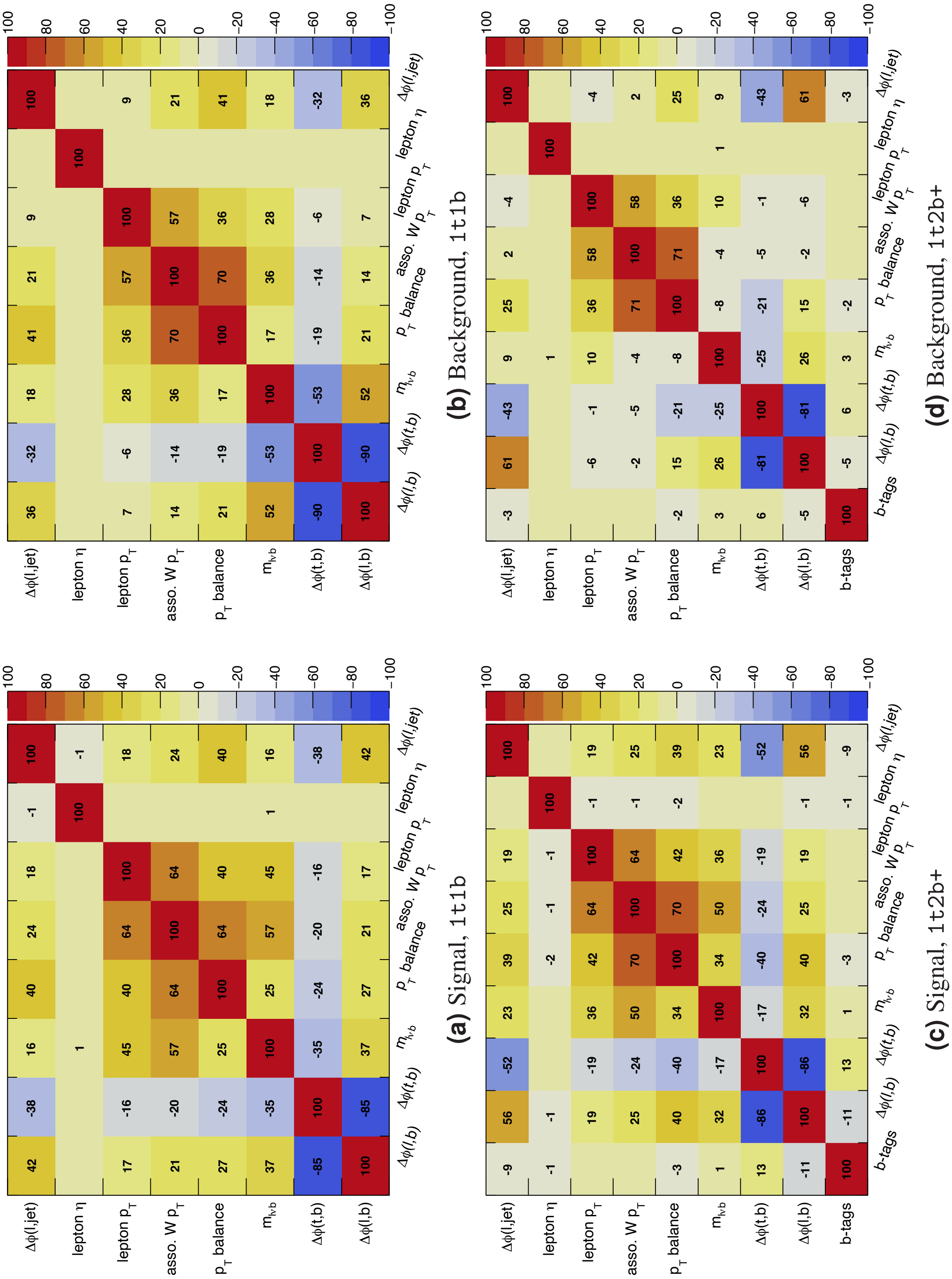

(a) Signal, 1t1b

(b) Background, 1t1b

(c) Signal, 1t2b+

(d) Background, 1t2b+

Figure 6.6.: Linear correlations between input variables in the BDT training as determined from the training samples, split up into signal (tW) and background ($t\bar{t}$) for each of the two categories 1t1b and 1t2b+. Values are given in percent.

6.2.2 Hyperparameters

A full list of possible configuration options for BDT training is given in the TMVA user guide, see Ref. 126, 128. Throughout this study, the effects of many configuration options have been tested. In the following, the most essential hyperparameters are listed and their settings, which have been chosen for the final training, are given. Most settings are equal for both categories.

- `NTrees`: The number of trees in the forest equals 100 (50) for the `1t1b` (`1t2b+`) category.
- `MaxDepth`: The maximum depth for each sequence of binary decisions (*branch*) is 3.
- `MinNodeSize`: The percentage of training events leftover in a leaf must not be lower than 2.5 %.
- `nCuts`: The number of grid points used in the scan for an optimal cut on a certain input variable is 10.
- `SeparationType`: An optimal cut on a certain input variable is defined by achieving the lowest *gini index* $p \cdot (1-p)$. Herein, p is either the signal or background purity.
- `BoostType`: Adaptive boosting is used. The boosting weight for previously misclassified events is defined as $\alpha = (1-\mathrm{err})/\mathrm{err}$ where err is the misclassification rate of the previous tree.
- `AdaBoostBeta`: The boosting weight is modified via $\alpha \to \alpha^{\beta}$ where β defines the learning rate of the adaptive boost algorithm. The `1t1b` (`1t2b+`) category uses $\beta = 0.1$ (0.5).
- `UseBaggedBoost`: Only a random sub-sample of the training sample is used for growing a tree in each iteration.
- `BaggedSampleFraction`: The fraction of the random sub-sample is 50 % (30 %) for the `1t1b` (`1t2b+`) category.
- `SigToBkgFraction`: The minimum fraction of signal events in a leaf is 10 %. This helps to keep overtraining under control.

Configuration options which are not listed here use default settings or the corresponding feature is deactivated.

6.2.3 Results

The receiver operating characteristic (ROC) curves of the two BDTs which have been trained with the configuration options of the previous section are shown in Fig. 6.7. They show background rejection versus signal efficiency. In addition, a dashed line indicates a critical boundary at which events would be classified randomly as either signal or background. The BDT of the

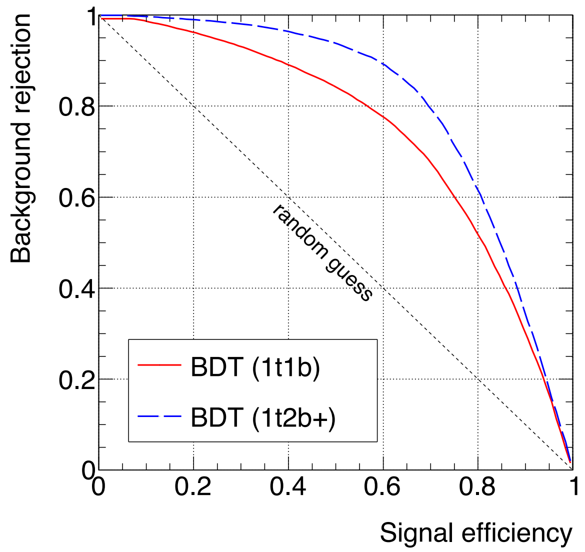

Figure 6.7.: Receiver operating characteristics (ROC) curves for the trained BDTs.

`1t2b+` category shows considerably better performance than the one of the `1t1b` category. This is reasoned by the already given argument that the selection of input variables is optimized for the former category. In this context, better performance means that, once a certain cut on the BDT response is selected which corresponds to a certain background rejection, more signal events are going to pass this cut than in the `1t1b` category.

The BDT response distributions for both categories are shown in Fig. 6.8. One can observe good agreement between training and testing samples of signal and background, respectively. The Kolmogorov-Smirnov (KS) tests return reasonable values; only the agreement between the background samples of the `1t1b` category seems to be poor according to its KS test, returning a value of 0.033. However, one can conclude from a simple shape comparison that overtraining is under control.

Tab. 6.1 shows the importance of each input variable, measured by the fraction of nodes in which they have been used during the training to achieve the best separation. The three most important discriminators are $\Delta\phi(\ell,\text{jet})$, $m_{\ell\nu\text{b}}$, and the p_{T} balance in each of the two BDTs. The least important ones are $\eta(\ell)$ and the number of b-tags.

Once applied to real data, the BDT response distributions in data and simulation are expected to be compatible with each other. This is the case as can be seen in the distributions presented in the next sections and the next chapter. A general offset between data and simulation with an average of 8 % can be observed due to missing top-tagging scale factors.

6.2.4 Cross Check in Control Regions

In order to further validate the functionality of the BDTs, they are also applied to control regions which cover a different phase space than the one considered for the measurement. The control regions are defined by the very same selection as given in Chapter 5 except that no top-

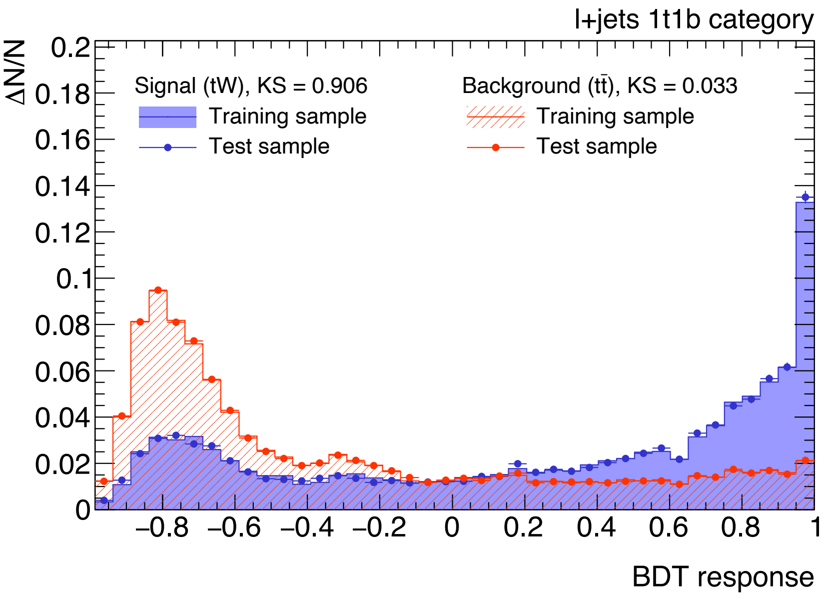

(a) `1t1b`

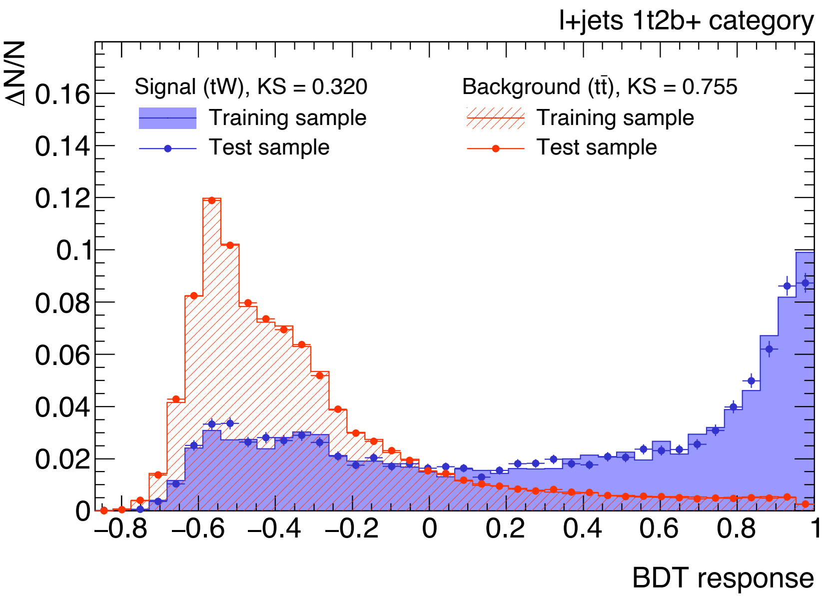

(b) `1t2b+`

Figure 6.8.: BDT response distributions for tW signal (blue) and $t\bar{t}$ background (red) samples for both the `1t1b` (upper plot) and `1t2b+` (lower plot) category. The response distributions are scaled to unit area and training (filled areas) and testing (dots) samples are superimposed for both signal and background. The agreement between training and testing samples is checked by Kolmogorov-Smirnov (KS) tests, respectively. Overtraining is under control.

Table 6.1.: Importance of input variables, measured by the amount of nodes which they are used in. For an explanation of the variable symbols, see Sect. 6.2.1. The three most often used variables are marked and ranked by asterisks.

Input variable	*1t1b*	*1t2b+*
$\Delta\phi(\ell, \mathrm{b})$	5.51 %	14.07 %
$\Delta\phi(\mathrm{t}, \mathrm{b})$	2.89 %	3.85 %
$\Delta\phi(\ell, \mathrm{jet})$	($\star\star\star$) 32.78 %	($\star$) 19.19 %
$\eta(\ell)$	2.59 %	3.67 %
$p_\mathrm{T}(\ell)$	($\star\star$) 30.18 %	6.18 %
$m_{\ell\nu\mathrm{b}}$	7.74 %	($\star\star\star$) 21.56 %
$p_\mathrm{T}(\mathrm{W})$	3.06 %	8.93 %
p_T balance	($\star$) 15.25 %	($\star\star$) 21.23 %
b-tags	N/A	1.32 %

tagged HOTVR jets must be present in the event. The input variables, which have initially been calculated by using information from the top-tagged HOTVR jet, now use the corresponding information from the leading untagged HOTVR jet. Fig. 6.9 exemplarily shows the response of the `1t2b+` BDT in the `0t2b+` category of the muon channel. In this example and all analogous control regions, good agreement between data and simulation is observed.

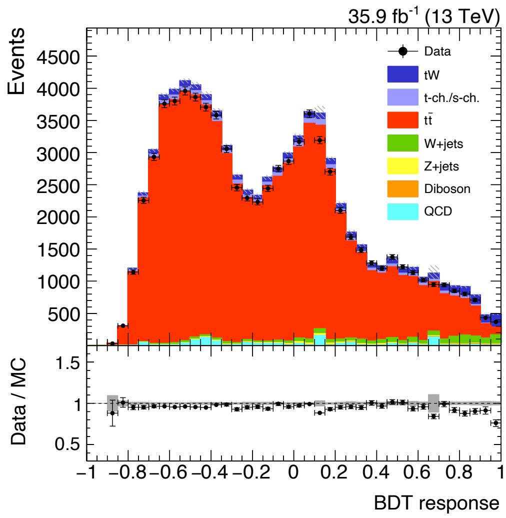

Figure 6.9.: BDT response in the `0t2b+` control region of the muon channel.

Fig. 6.9 shows a similar $\mathrm{t\bar{t}}$ accumulation from −0.3 to −0.7 like in the `1t2b+` BDT response in Fig. 6.8, validating the background rejection efficiency. In addition, a broad peak around 0.0 is observed which indicates that many events cannot be identified to be signal or background at all. This is as expected: Events in the control regions are less likely to have signal-like or background-like properties since they did not pass the top-tagging requirement in the first place. This is also reflected by the almost even distribution of tW production across the response except for a slight enrichment in the signal-like region close to $+1$. Interestingly, W+jets production shows a clear trend to be identified as signal-like.

6.3 Phase-Space Optimization

In order to get signal-enriched data sets, a cut on the BDT response in each of the four measurement phase spaces, as defined in Sect. 5.4.3, is applied. The best cut value is defined as the one that results into the highest statistical significance ($S/\sqrt{S+B}$) of the signal, estimated from its contribution according to the predicted model. The BDT response is scanned in steps of 0.05 individually in each of the four phase spaces, see Fig. 6.10a, Fig. 6.10b, Fig. 6.11a, and Fig. 6.11b. The resulting top-jet p_{T} spectra are shown in Fig. 6.10c, Fig. 6.10d, Fig. 6.11c, and Fig. 6.11d, respectively.

In addition, the resulting jet-mass spectra of the top-jet are shown in Fig. 6.10e, Fig. 6.10f, Fig. 6.11e, and Fig. 6.11f, respectively. It demonstrates that an optimized future analysis might be able to perform a differential measurement of the top-jet mass in highly boosted single-top-quark events. Since the top-jet mass is sensitive to the top-quark mass, an extraction of the top-quark mass is then possible as well. A similar measurement has been performed before, using highly boosted $\mathrm{t\bar{t}}$ events [129].

As a final sanity check, the distributions of the input variables have been investigated again after the application of those cuts on the BDT responses. The variables show no more significant separation power between $\mathrm{t\bar{t}}$ and tW. This is as expected since, in the ideal case, a multivariate algorithm is supposed to “absorb” the separation power of its input variables completely. This further validates the functionality of the BDTs.

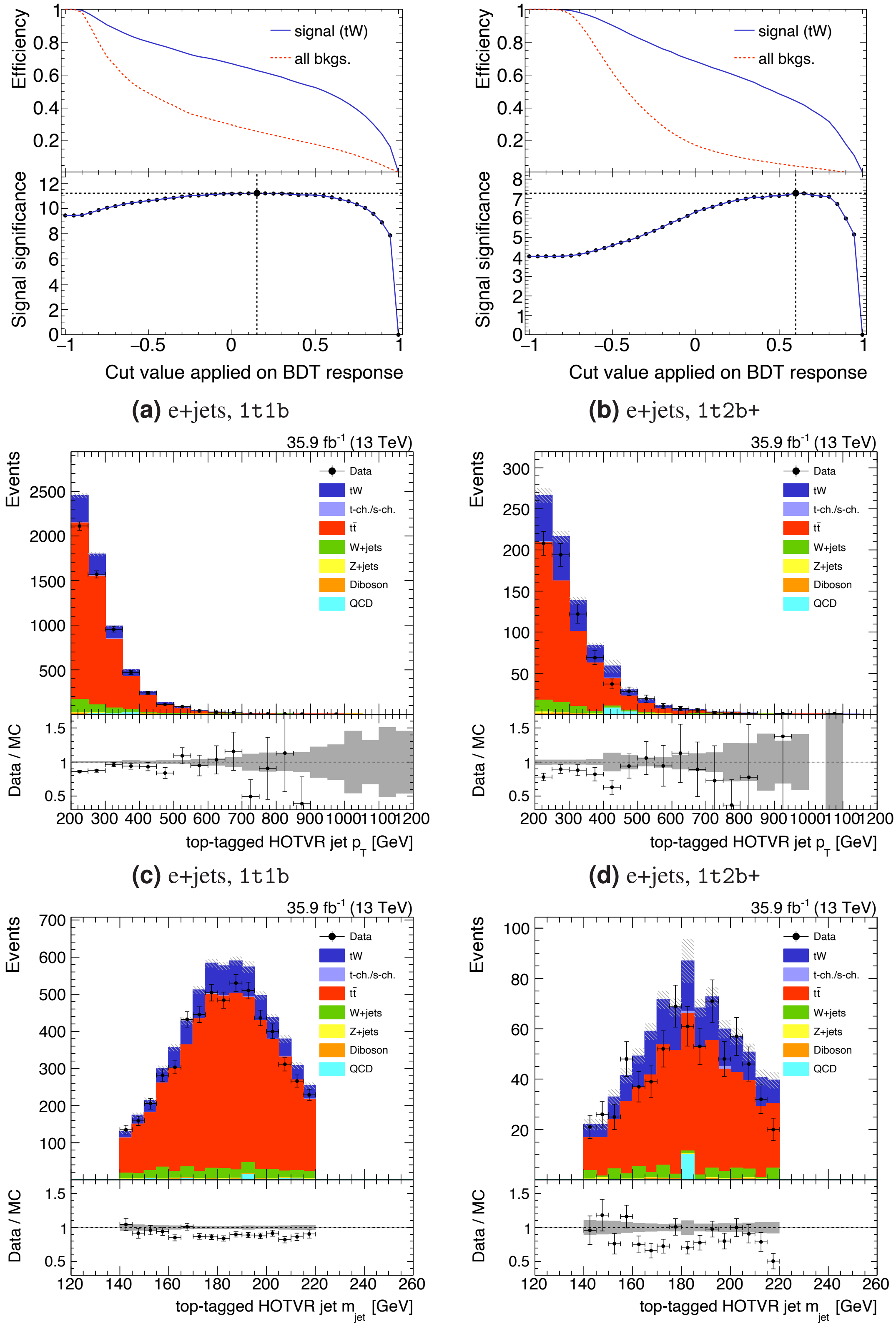

(a) e+jets, `1t1b` **(b)** e+jets, `1t2b+`

(c) e+jets, `1t1b` **(d)** e+jets, `1t2b+`

(e) e+jets, `1t1b` **(f)** e+jets, `1t2b+`

Figure 6.10.: A scan of the signal significance ($S/\sqrt{S+B}$) versus possible cuts on the BDT response in steps of 0.05 is shown in **(a)** and **(b)** in the `1t1b` and `1t2b+` category, respectively, for the **electron channel**. Optimal cuts are determined to be at 0.15 and 0.60, respectively. Figure **(c)** and **(d)** show the top-jet p_{T} after applying these BDT cuts in the respective phase space as defined in Sect. 5.4.3. Also, the top-jet mass after these cuts is shown in **(e)** and **(f)**.

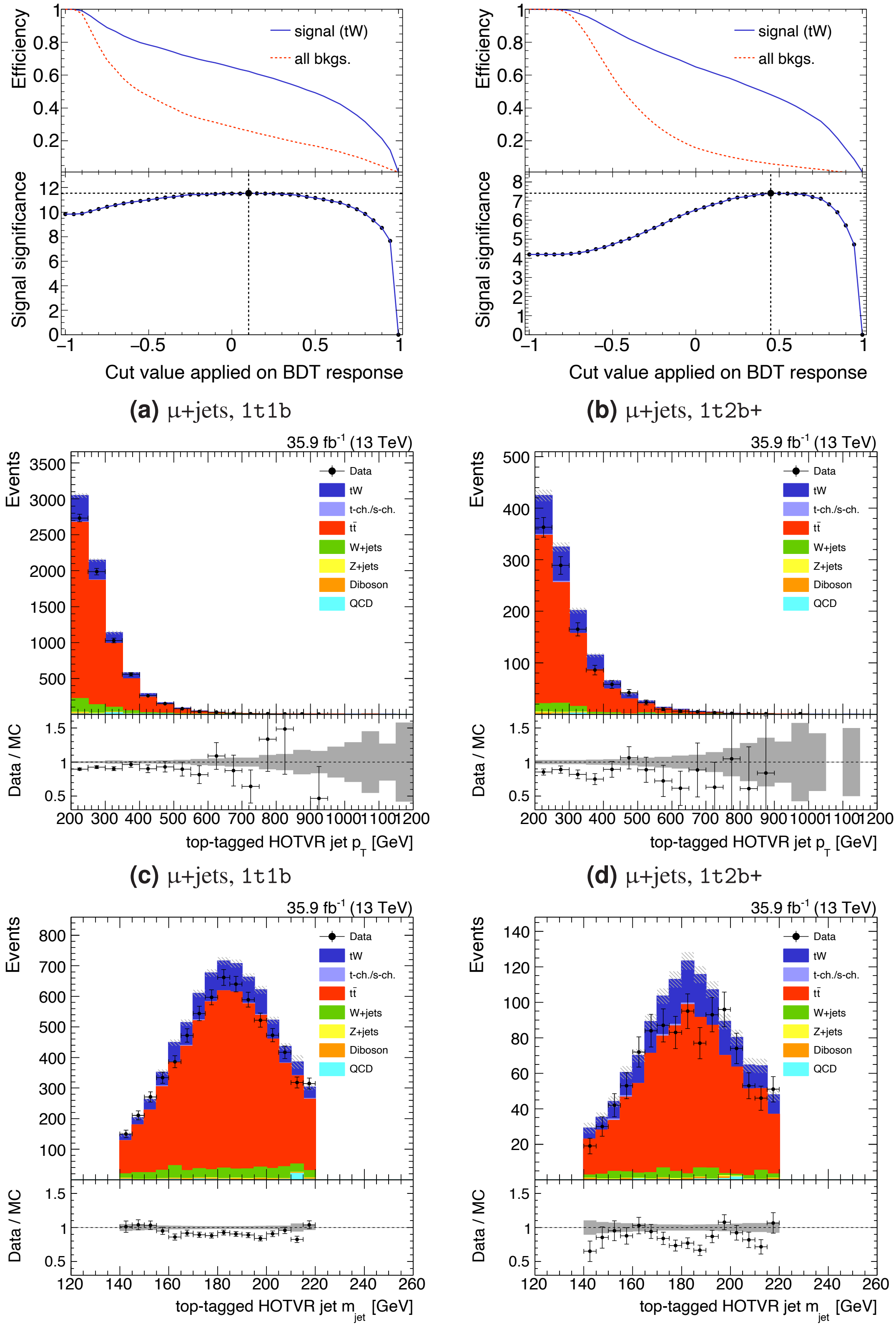

(a) μ+jets, `1t1b` **(b)** μ+jets, `1t2b+`

(c) μ+jets, `1t1b` **(d)** μ+jets, `1t2b+`

(e) μ+jets, `1t1b` **(f)** μ+jets, `1t2b+`

Figure 6.11.: A scan of the signal significance ($S/\sqrt{S+B}$) versus possible cuts on the BDT response in steps of 0.05 is shown in **(a)** and **(b)** in the `1t1b` and `1t2b+` category, respectively, for the **muon channel**. Optimal cuts are determined to be at 0.10 and 0.45, respectively. Figure **(c)** and **(d)** show the top-jet p_T after applying these BDT cuts in the respective phase space as defined in Sect. 5.4.3. Also, the top-jet mass after these cuts is shown in **(e)** and **(f)**.

7 Cross-Section Extraction

In this final analysis chapter, the differential cross-section measurements of W-associated single boosted top-quark production as function of the top-quark transverse momentum are performed. The top-jet p_{T} distributions in the electron and muon channel are respectively split up into the `1t1b` and `1t2b+` category and rebinned into four bins, as shown in Fig. 7.1. The bin widths are chosen such that there are still reasonable statistics provided in the higher p_{T} bins. In Sect. 7.1, the set of systematic uncertainties considered for the measurements is presented. In order to estimate the contribution of each physical process within each of the four bins of each top-jet p_{T} distribution, likelihood fits are performed on BDT response distributions. These are obtained by applying the BDT of the respective category trained in Chapter 6 on the phase space defined by that top-jet p_{T} bin. The cut values which have been estimated beforehand in Sect. 6.3 are not applied. Since the discrimination between signal and background processes is more optimized for the BDT distributions than for any other observable considered in this analysis, it stands to reason to use these as templates for the fitting procedure which is described in Sect. 7.2. In order to obtain cross sections as function of the top-quark p_{T}, the top-jet p_{T} distributions are unfolded in Sect. 7.3. The final results are presented in Sect. 7.4.

7.1 Estimation of Systematic Uncertainties

Aside from statistical uncertainties, several systematic effects have to be considered. The BDT distributions and the top-jet p_{T} spectrum can be affected by the detector resolution, object reconstruction efficiencies, and theoretical modelling uncertainties for signal and background processes. Some systematic uncertainties may only affect the normalization whereas others may affect the shape of distributions. The different sources of systematic uncertainties which have been considered for the final results of this analysis are listed in the following:

- The overall uncertainty on the measurement of the integrated luminosity of the 2016 data set, which the MC samples have been scaled to according to Expr. 5.1, is estimated to be ± 2.5 % [130]. This uncertainty is added after the unfolding procedure.

- Uncertainties on the production cross sections of the backgrounds, which the corresponding MC samples have been scaled to, have to be taken into account as well. They are:
  - Single-top t- and s-channel: 10 % [131]
  - $\mathrm{t\bar{t}}$: 20 % [125]

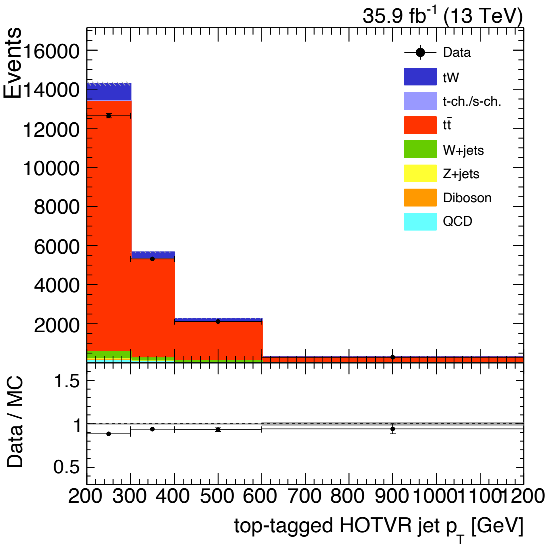

(a) e+jets, `1t1b`

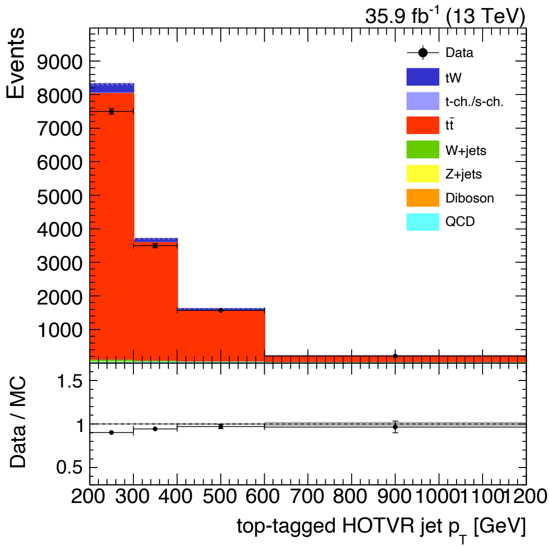

(b) e+jets, `1t2b+`

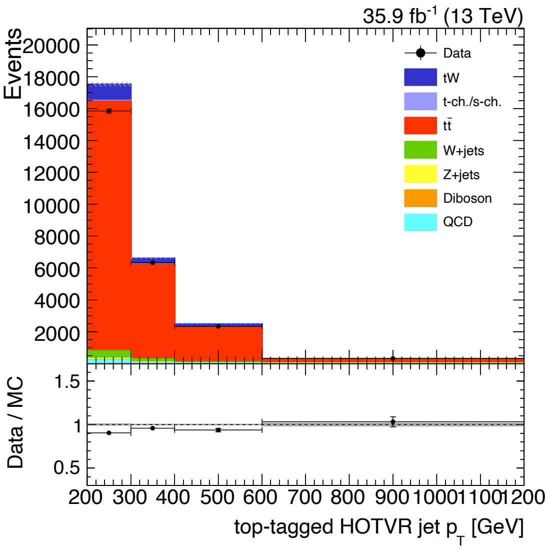

(c) μ+jets, `1t1b`

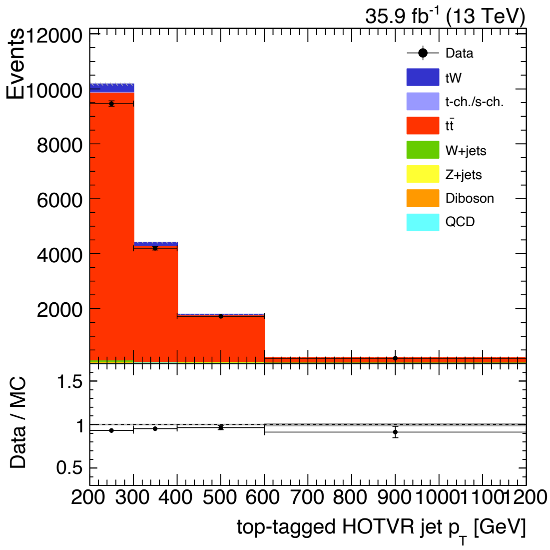

(d) μ+jets, `1t2b+`

Figure 7.1.: Re-binned pre-fit p_{T} distributions of the top-tagged HOTVR jet in the different measurement phase spaces. For a more refined binning, see Fig. 5.8. Uncertainties on the model prediction represent MC statistics only. For the fitting, the QCD background is removed due to its low MC statistics and negligible contribution.

  - W+jets and Z+jets: 10 % [132]
  - Diboson: 20 % [133–135]
  - QCD is removed from the model due to its negligible contribution and too low MC statistics. Thus, no uncertainty on its production cross section has to be considered.

- Uncertainty on the jet energy scale (JES). In this analysis, jet energy corrections (JEC) have been applied to AK4 jets and HOTVR sub-jets, cf. Sect. 4.5.4. These corrections are varied up and down by one standard deviation, respectively, and the resulting variations in the BDT response distribution is considered as systematic uncertainty.

- The jet energy resolution (JER) of AK4 jets and HOTVR sub-jets is, similar to the treatment of the JES uncertainty, varied up and down by one standard deviation and the resulting variations in the BDT response distribution is considered as systematic uncertainty.

- Uncertainty on b-tagging scale factors. The tagging efficiencies are varied up and down within one standard deviation of their statistical uncertainties. The tagging efficiencies of jets originating from b and c quarks are taken as fully correlated. The tagging efficiency of jets originating from light quarks and gluons is taken as uncorrelated to the b- and c-tagging efficiencies. Consequently, two distinct systematic uncertainties are considered:
  - Uncertainty on the b- and c-tagging efficiency.
  - Uncertainty on the tagging efficiency of light-quark and gluon jets.

- Uncertainty on the minimum-bias cross section of 69.2 mb which is used for the calculation of the pile-up re-weighting scale factors. This cross section is varied up and down by 5 % and the resulting variation in the BDT response distribution is taken as systematic uncertainty.

- Uncertainties on the renormalization scale μ_{R} and factorization scale μ_{F}, cf. Sect. 2.1. In each MC sample in Tab. 5.1, except for the POWHEG tW samples, individual weights are provided for each generated event which correspond to different choices of μ_{R} and μ_{F}, respectively. In order to estimate the uncertainty on these scales, they are independently varied up and down by a factor of 0.5 and 2, respectively. The envelope in the BDT response distributions which arises from these independent variations is taken as systematic uncertainty. The fact that these variations are not provided for the signal process needs to be fixed in the future.

- Uncertainties on the scale factors which correct for differences in data and simulation w. r. t. lepton trigger and identification efficiencies. In order to account for these, a normalization uncertainty of 2 % is applied after the unfolding.

This list includes only a subset of all systematic uncertainties which must be considered for a thorough estimation of systematic effects. Other possible sources, which have to be considered in the future, are for instance: The choice of the PDF sets for the model prediction; uncertainties on top-tagging scale factors once they are applied; uncertainties on the top-p_{T} re-weighting in $\mathrm{t\bar{t}}$ simulation; uncertainties on the $\not{E}_{\mathrm{T}}$ measurement; uncertainties on the overall jet energy scale of HOTVR jets.

7.2 Maximum-Likelihood Template Fits

In total, sixteen individual maximum-likelihood fits are performed, one in each of the top-jet p_{T} bins shown in Fig. 7.1, using the BDT response distribution in the phase space defined by the corresponding top-jet p_{T} interval. In particular, the method of *binned* maximum-likelihood fitting is employed and will therefore be described in Sect. 7.2.1, based on a brief summary given in Ref. 136. A more detailed review on this method can be found in Ref. 12. The implementation of this method into this analysis has been done with the THETA framework [137]. The post-fit results are presented and discussed in Sect. 7.2.2.

7.2.1 Mathematical Description

The method of maximum likelihood (ML) is a statistical tool to estimate the true values of the parameters of a given model $\vec{\theta} = \{\theta_1, \ldots, \theta_n\}$, based on a set of measured data $\vec{x} = \{x_1, \ldots, x_N\}$. Usually, x_i represents the data yield measured in a specific bin i of an observable divided into N bins; in this particular case, this observable is the BDT response. The maximum-likelihood method is based on a likelihood function which is defined as

$$L\left(\vec{x}|\vec{\theta}\right) = \prod_{i=1}^{N} f\left(x_i|\vec{\theta}\right) \tag{7.1}$$

where $f(x_i|\vec{\theta})$ is a probability density function (p. d. f.), describing the probability of observing the measured data x_i in bin i under the assumption that the model $\vec{\theta}$ is correct.

A priori, it can be assumed that the number of events in a certain bin i is independent from the number of events in another bin $j \neq i$. Moreover, the number of events x_i can be assumed to be Poisson-distributed such that each p. d. f. can be written as

$$f\left(x_i|\lambda_i\left(\vec{\theta}\right)\right) = \frac{\lambda_i\left(\vec{\theta}\right)^{x_i}}{x_i!} \cdot \exp\left(-\lambda_i\left(\vec{\theta}\right)\right) \tag{7.2}$$

where λ_i is the expected number of events in bin i, dependent on the parameters of the model. The true parameter values θ_i are estimated by finding solutions to the likelihood equations

$$\frac{\partial \log L\left(\vec{x}|\vec{\theta}\right)}{\partial \theta_i} = 0, \qquad \text{where } i \in \left\{1, \ldots, n\right\}, \tag{7.3}$$

what in most cases must be done numerically. The solutions to these equations maximize the likelihood function, giving this statistical method its name.

In order to incorporate systematic uncertainties into the fitting procedure, the likelihood function is expanded, using the following ansatz:

$$L\left(\vec{x}|\vec{\theta}(\vec{\nu}),\vec{\nu}\right) = \prod_{i=1}^{N} f\left(x_i|\vec{\theta}(\vec{\nu})\right) D(\vec{\nu}) = \prod_{i=1}^{N}\prod_{j=1}^{M} f\left(x_i|\vec{\theta}(\nu_j)\right)\cdot d\left(\nu_j|\hat{\nu}_j,\sigma_{\nu_j}\right). \tag{7.4}$$

Herein, $\vec{\nu} = \{\nu_1,\ldots,\nu_M\}$ denotes the vector of *nuisance parameters* of the M different sources of systematic uncertainties which are considered. The additionally introduced terms

$$D(\vec{\nu}) = \prod_{j=1}^{M} d\left(\nu_j|\hat{\nu}_j,\sigma_{\nu_j}\right) \tag{7.5}$$

are given by probability distributions d which are defined by a certain mean value $\hat{\nu}_j$ and the associated width σ_{ν_j}. The values ν_j of the nuisance parameters can freely be varied such that the maximization of the likelihood function can be achieved. They influence the model parameters $\vec{\theta}(\vec{\nu})$ according to a certain *response function*. Usually, this response function is parametrized in such a way that its mean value is $\hat{\nu}_j = 0$ and its standard deviation is $\sigma_{\nu_j} = 1$. Hence, the nominal values of the model parameters $\vec{\theta}$ correspond to $\vec{\nu} = 0$ and the margins of one standard deviation of a specific model parameter, i. e. systematic uncertainty, j correspond to $\nu_j = \pm 1$.

One has to distinguish between two types of systematic uncertainties: Firstly, *rate uncertainties* which just affect the overall normalization of a physical process but not the shape of its distribution within the considered observable. And, secondly, *shape uncertainties* which affect the shape on the one hand and, contingently but not necessarily, the normalization on the other hand. In Expr. 7.5, rate uncertainties are implemented as log-normal probability distributions whereas shape uncertainties are implemented as Gaussian distributions.

The theoretical model is generated using Monte-Carlo techniques, resulting into finite sample sizes. Therefore, there is additionally a *statistical uncertainty* besides the systematic uncertainties. Statistical uncertainties are given for each individual bin of the observable distribution each of which is modelled by a Poisson distribution with a mean value corresponding to the number of generated MC events in that bin. In general, statistical uncertainties are treated in the same way as systematic uncertainties. However, the difference is that there is an individual nuisance parameter ν_j for each observable bin instead of just a single one across all bins. This is reasoned by the fact that statistical fluctuations are assumed to be uncorrelated across bins whereas the effects of a specific systematic uncertainty are usually correlated throughout all bins.[1]

The above mentioned response function for rate uncertainties can be derived in a relatively

[1] A detailed description of this implementation of MC statistical uncertainties into likelihood-based fitting, called *Barlow-Beeston lite* method, can be found in Ref. 138, 139.

trivial way since variations of the corresponding nuisance parameters ν_j just correspond to normalization shifts correlated across all bins of the observable distribution as described before. In contrast, shape uncertainties require another treatment known as *vertical template morphing*, using the up and down variations of the corresponding systematic uncertainty, as described in Sect. 7.1. Herein, these variations define the margins of one standard deviation given by $\nu_j = \pm 1$. The response functions are approximated by interpolating between $\nu_j = -1$, $\nu_j = 0$, and $\nu_j = +1$ using a cubic function and by extrapolating beyond $\nu_j = \pm 1$ using a linear ansatz.

7.2.2 Fitting Procedure and Discussion of Results

The nominal MC samples as well as all systematic uncertainties described in Sect. 7.1 except for the luminosity, lepton trigger, and lepton identification uncertainties are used as input for non-simultaneous maximum-likelihood fits in the sixteen BDT response distributions. In addition, a cross-section normalization (rate) uncertainty of 100 % is assumed for the tW sample since this is the process which is to be measured. Accordingly, the tW rate and its uncertainty have to be constrained by the fits. The binning of the BDT distributions has been optimized by choosing a decreasing number of equally sized bins with increasing top-jet p_{T} so that the behaviour of the fits is not dominated by MC statistics in the high-p_{T} bins:

- $p_{\mathrm{T}} \in (200, 300]$ GeV: 20 bins,
- $p_{\mathrm{T}} \in (300, 400]$ GeV: 10 bins,
- $p_{\mathrm{T}} \in (400, 600]$ GeV: 5 bins, and
- $p_{\mathrm{T}} \in (600, 1200]$ GeV: 4 bins.

Appendix B provides plots of all pre- and post-fit BDT distributions, of all post-fit values of nuisance parameters, and of correlation matrices describing the linear correlations between nuisance parameters within each fit. It is observed that all fits converge, i. e. each likelihood-function maximization procedure succeeds. The post-fit values of all nuisance parameters of systematic uncertainties remain within a band of two standard deviations of their corresponding prior uncertainty. In general, shifts within one or two standard deviations are as expected whereas larger shifts, which are not observed, would indicate a fundamental problem with the modelling.

In almost all fits, high linear correlations between the nuisance parameters of the $\mathrm{t\bar{t}}$ production rate and certain systematic uncertainties are observed, predominantly renormalization/factorization scale (correlations ranging between +58 % and +96 %) but also jet energy corrections (mostly anti-correlations ranging up to −41 %) and b-tagging scale factors (anti-correlations up to −35 %). Since $\mathrm{t\bar{t}}$ production is the dominant process of the predicted model, these correlations are expected. The very high correlations between the renormalization/factorization scale uncertainty and the $\mathrm{t\bar{t}}$ rate uncertainty is explained by the fact that the

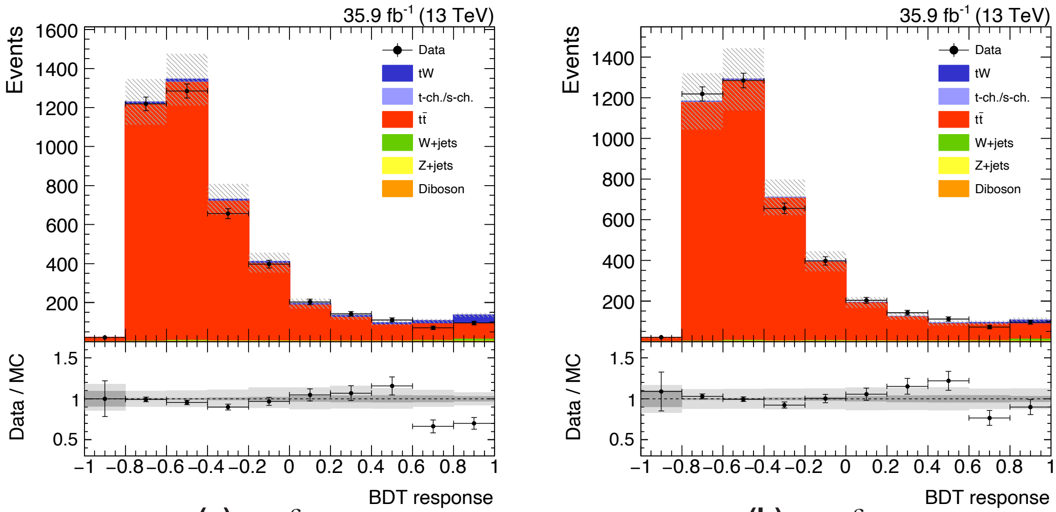

(a) pre-fit **(b)** post-fit

Figure 7.2.: Pre-fit (left) vs. post-fit (right) BDT response distributions in the `1t2b+` category of the muon channel for top-jet $p_T \in (300, 400]$ GeV. A significant down shift of the tW signal is observed, reasoned by the poor agreement between data and pre-fit model in the signal-enriched region of the response. The BDT distributions in all other phase spaces are given in Appendix B.

second-most contributing process, tW production, has no such uncertainty applied since there are no corresponding variations available for the MC sample as mentioned before. Of course, this has to be fixed in the future. Correlations between other nuisance parameters can be seen as coincidental in the respective cases.

A general tendency towards a significant downshift of the tW rate is observed. The most extreme case for this behaviour is found in the second bin (top-jet $p_T \in (300, 400]$ GeV) in the `1t2b+` category of the muon channel. The pre- and post-fit BDT distributions of this bin are shown in Fig. 7.2. The post-fit rate of tW drops to around 40 % of its prior value in this case. This behaviour of the fit is explained by the poor agreement between data and predicted model in the signal-enriched region of the pre-fit BDT response between 0.6 and 1.0. The same phenomenon is observed in several other BDT distributions. Possible explanations for this behaviour are, on the one hand, missing scale factors or, on the other hand, the fact that the BDTs have been trained on the entire phase space $p_T \in (200, 1200]$ GeV such that they learned predominantly from the low-p_T region. The latter argument would at least explain deviations in the higher p_T bins since the BDTs are optimized for the lowest p_T bin. Further, it is also conceivable that the kinematics of tW production in the boosted sector are not well enough described by the simulated model. Moreover, a possible incompatibility between the used $t\bar{t}$ and tW MC samples in terms of their handling of NLO interferences (cf. the diagram removal and diagram subtraction methods described in Sect. 2.2.2) needs to be checked for in the future.

7.3 Simplified Bin-By-Bin Unfolding Procedure

The kinematic distributions presented so far in this thesis include detector effects, like finite detector resolution or limited acceptance. In other words, the original physical properties on parton level, which one is interested in, are folded with the detector response which, for MC samples, has been simulated in detail for each event. In order to measure differential cross sections as function of the true top-quark p_T rather than the top-jet p_T on detector level, the kinematic distribution needs to be unfolded to parton level. In general, one has to consider migrations between bins of a certain kinematic distribution for each event. In this particular case, the measured top-jet p_T is most certainly not equal to the true top-quark p_T since a jet contains also information from the detector as set out above. Usually, a method called *regularized unfolding* is employed which accounts for these effects via a so-called migration matrix, see e. g. Ref. 140. However, this approach lies beyond the scope of this thesis and, thus, a simplified unfolding procedure is employed which is described in the following. The results of this method, which still are able to give relatively reliable estimates for a future analysis, are discussed subsequently in Sect. 7.4.

Assuming that migration effects are negligible, it is postulated that each bin of the measured distribution can be corrected by a simple multiplicative factor which has to be determined from simulation. This correction factor is defined as

$$f_i^{\mathrm{corr}} = \frac{x_i^{\mathrm{rec}}}{y_i^{\mathrm{gen}}} \tag{7.6}$$

where x_i^{rec} represents the MC signal yield in bin i of the top-jet p_T distribution after applying the event selection on reconstruction level and y_i^{gen} represents the MC signal yield in bin i of the true top-quark p_T distribution after applying an independent selection on generator level, here parton level. In this analysis, the cuts which define the generator-level selection applied on the full tW signal sample are:

- Require the hadronic decay of the top quark and the leptonic decay of the associated W boson ($W \rightarrow e\nu$ for the electron channel or $W \rightarrow \mu\nu$ for the muon channel).
- Require the top quark to fulfil $p_T > 200$ GeV and $|\eta| < 2.5$ similar to the requirements on the top-jet candidate as included in the reconstruction-level event selection.

The correction factors are determined for the `1t1b` and `1t2b+` category of the electron and muon channel, respectively. The obtained corrections factors for each bin are shown in Fig. 7.3.

In order to obtain cross sections of tW production as function of the true top-quark p_T, the post-fit yield of the tW sample in each bin i, which from now on is interpreted as the tW yield taken from data ($y_i^{\mathrm{data,\,tW}}$ with uncertainty $\delta y_i^{\mathrm{data,\,tW}}$), has to be adjusted using the corresponding determined correction factor f_i^{corr}. The event yield x_i^{BBB} and its uncertainty $\delta x_i^{\mathrm{BBB}}$ after this

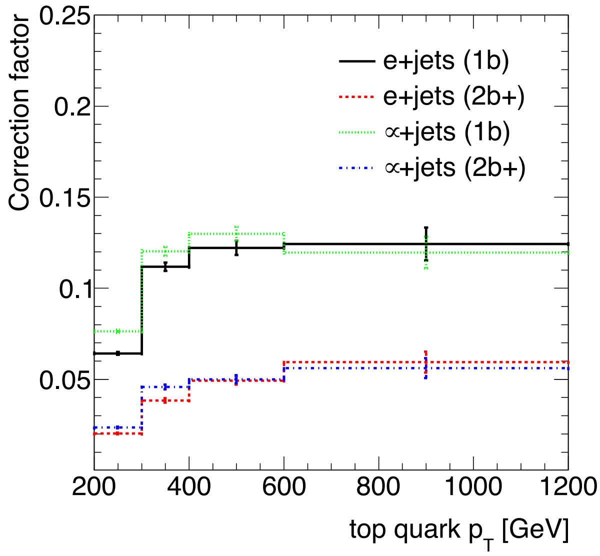

Figure 7.3.: Correction factors for the simplified bin-by-bin unfolding procedure. The shown error bars are calculated from MC statistical uncertainties of the underlying generator-level and reconstruction-level distributions, assuming 100 % covariance.

bin-by-bin (BBB) unfolding are calculated to be

$$x_i^{\text{BBB}} = \frac{1}{f_i^{\text{corr}}} y_i^{\text{data, tW}}, \qquad \delta x_i^{\text{BBB}} = \frac{1}{f_i^{\text{corr}}} \delta y_i^{\text{data, tW}}. \tag{7.7}$$

The event yields are then translated into actual cross sections by dividing through the integrated luminosity of the data set, corresponding to $L_{\text{int}} = 35.87\ \text{fb}^{-1}$.

7.4 Results and Combination of Channels

The results of the differential cross-section measurement of tW production as function of the top-quark p_{T} in the electron and muon channel, each divided into the `1t1b` and `1t2b+` category, are given in Fig. 7.4. The constrained rate uncertainty of tW is interpreted as statistical uncertainty since, as a normalization uncertainty, it is expected to be sensitive to the statistical uncertainty of data during the fitting procedure. Since both the `1t1b` and `1t2b+` category in the electron (muon) channel measure the same differential cross sections but in different phase spaces, they are combined. The combination for the electron (muon) channel is shown in Fig. 7.5a (Fig. 7.5b). In each bin, the weighted average of the results in the two categories is taken as result for the combination. In each case, the inverse of the square of the corresponding total uncertainty (the variance) is taken as weight. Systematic uncertainties are propagated assuming 100 % covariance between the two measurement phase spaces. Statistical uncertainties are propagated without covariance since the two phase spaces are statistically independent. In a last step, the results of these combinations are added to obtain differential cross sections in the combined ℓ+jets[2] channel, see Fig. 7.6. Uncertainties are propagated like before. All results are also summarized in Tab. 7.1.

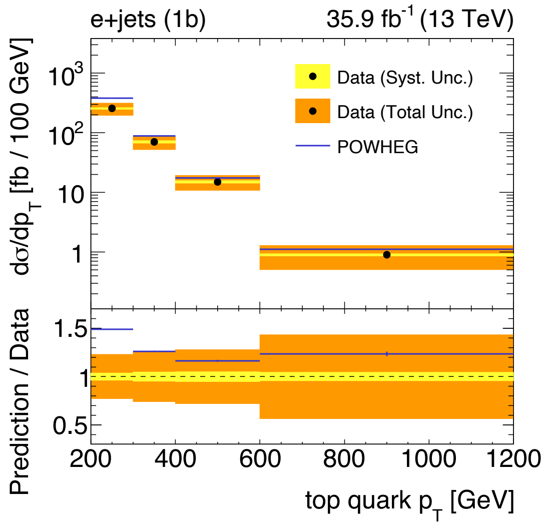

(a) e+jets, 1t1b

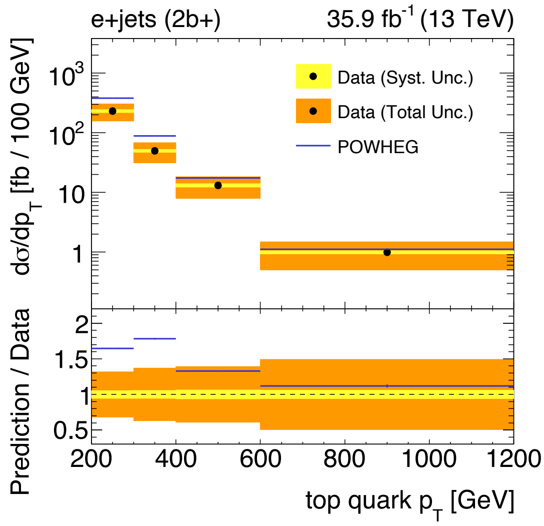

(b) e+jets, 1t2b+

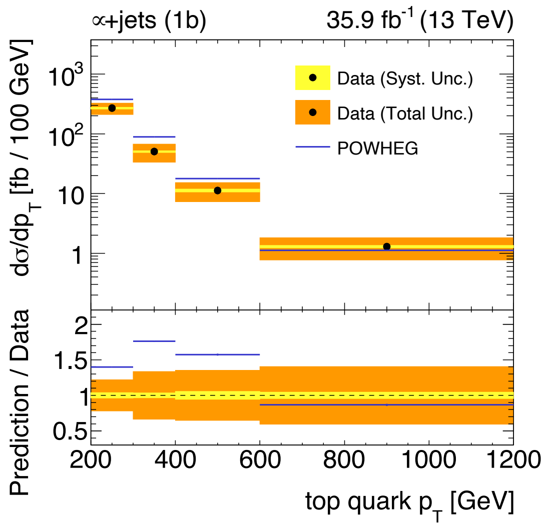

(c) μ+jets, 1t1b

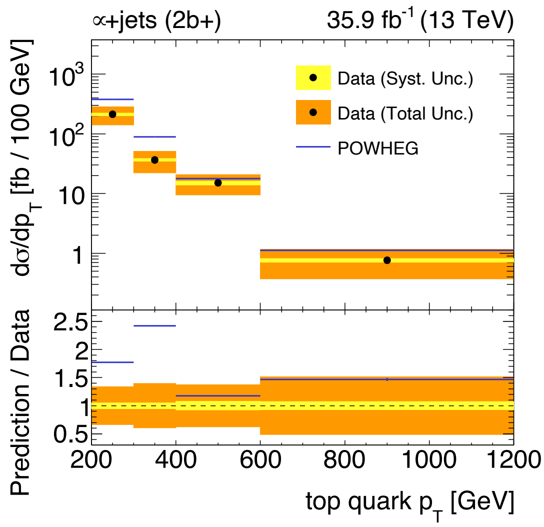

(d) μ+jets, 1t2b+

Figure 7.4.: Results for the cross-section measurements in electron and muon channel. The theory prediction derived from the POWHEG MC tW sample with the corresponding generator-level cuts applied is shown in comparison to the measured differential cross sections. Uncertainties on the prediction depict MC statistics. The results are also summarized in Tab. 7.1.

[2] Of course, this only refers to the final state in which the top quark decays hadronically and the associated W boson decays leptonically.

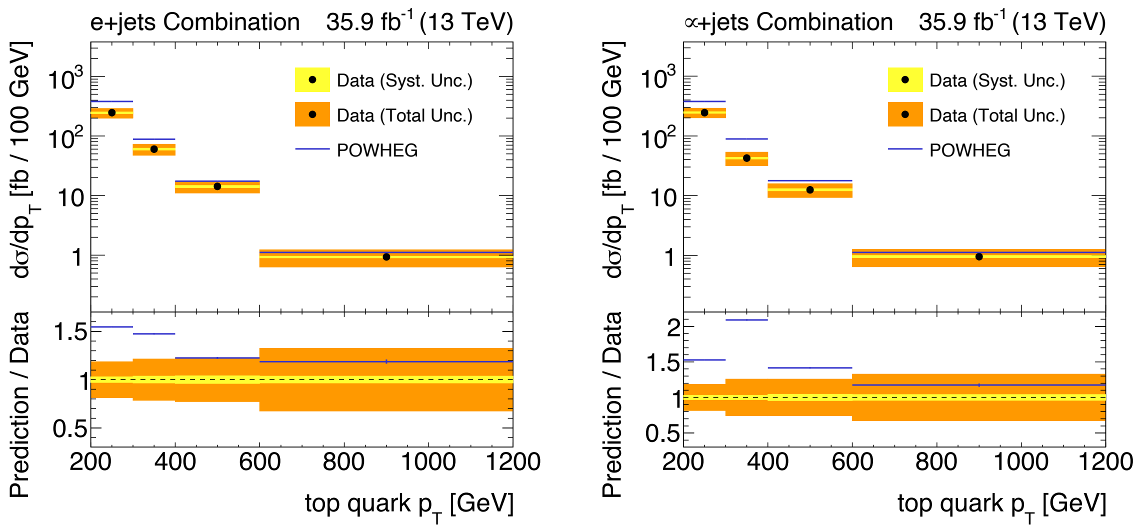

(a) e+jets combination **(b)** μ+jets combination

Figure 7.5.: Results for the combinations of measured differential cross sections in the `1t1b` and `1t2b+` categories for electron (left) and muon (right) channel. The theory prediction derived from the POWHEG MC tW sample with the corresponding generator-level cuts applied is shown in comparison to the measured differential cross sections. Uncertainties on the prediction depict MC statistics. The results are also summarized in Tab. 7.1.

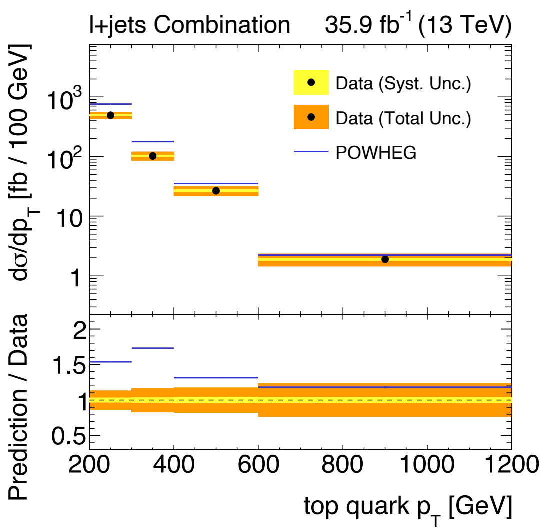

Figure 7.6.: Results for the ℓ+jets combination of differential cross-section measurements in the electron and muon channel. The theory prediction derived from the POWHEG MC tW sample with the corresponding generator-level cuts applied is shown in comparison to the measured cross sections. Uncertainties on the prediction depict MC statistics. The results are also summarized in Tab. 7.1.

Table 7.1.: Final results of the differential cross-section measurements as function of the top-quark p_T. Cross sections are given in **fb / 100 GeV**. Uncertainties are given in percent and are divided into statistical and systematic uncertainties, in that order. Corresponding diagrams visualizing the results are found in Fig. 7.4, Fig. 7.5, and Fig. 7.6.

Category	$p_T \in$ *(200, 300] GeV*	$p_T \in$ *(300, 400] GeV*	$p_T \in$ *(400, 600] GeV*	$p_T \in$ *(600, 1200] GeV*
e+jets, 1t1b	255.2 ± 22.6% ± 3.6%	70.2 ± 25.5% ± 4.7%	15.0 ± 27.4% ± 5.1%	0.90 ± 43.2% ± 4.4%
e+jets, 1t2b+	230.8 ± 31.2% ± 5.4%	49.7 ± 36.7% ± 5.6%	13.1 ± 38.6% ± 6.4%	0.99 ± 48.8% ± 6.1%
e+jets combination	245.7 ± 18.3% ± 3.0%	60.1 ± 21.3% ± 3.6%	14.2 ± 22.4% ± 4.0%	0.93 ± 32.4% ± 3.6%
μ+jets, 1t1b	268.9 ± 21.6% ± 3.8%	50.4 ± 33.3% ± 3.6%	11.3 ± 34.8% ± 5.8%	1.29 ± 40.3% ± 4.5%
μ+jets, 1t2b+	212.5 ± 33.4% ± 5.2%	36.6 ± 39.1% ± 5.4%	15.1 ± 36.8% ± 7.7%	0.76 ± 50.9% ± 7.2%
μ+jets combination	246.2 ± 18.3% ± 3.1%	42.5 ± 25.7% ± 3.2%	12.5 ± 25.6% ± 4.6%	0.95 ± 32.6% ± 4.3%
ℓ+jets combination	491.9 ± 12.9% ± 3.1%	102.6 ± 16.4% ± 3.4%	26.8 ± 16.9% ± 4.3%	1.89 ± 23.0% ± 3.9%

8 Summary and Outlook

The first measurement of single top-quark production in the highly Lorentz-boosted kinematic regime has been presented in this thesis. The utilized data set is based on proton-proton collisions at a center-of-mass energy of 13 TeV. Differential cross sections were measured as function of the top-quark transverse momentum in the W-associated production channel of single top quarks, ranging from 200 GeV to 1200 GeV. The electron+jets and muon+jets final states were considered for this analysis, presuming that the top quark decays hadronically. The top quark was reconstructed as one collimated large jet, using the HOTVR jet clustering algorithm. Top-tagging requirements were applied to top-jet candidates. The dominant background in the measurement phase space was top-quark pair production. In order to discriminate between this background and the single-top signal, a multivariate algorithm was used. Boosted decision trees were trained for two distinct phase-space categories, defined by the number of b-tagged jets. A maximum-likelihood method was used to fit the theory prediction to data in different intervals of the top-jet transverse momentum, using the response distributions of the previously trained BDTs. Cross sections on parton level were extracted, using a simplified unfolding method.

The uncertainties on the measured cross sections are dominated by statistics. However, not all systematic uncertainties which have to be considered were implemented. The measured cross sections are significantly smaller than the ones predicted by the POWHEG MC samples of W-associated single-top production, especially in the bins of lower transverse momentum. This results from a significant downshift of the signal rate in the maximum-likelihood fits. This downshift is due to disagreement between simulation and data in the signal-enriched region of the fitted BDT response distributions. Possible explanations for this behaviour were discussed. A future analysis needs to investigate possible solutions. Nevertheless, this thesis demonstrates that differential cross-section measurements of single boosted top-quark production are in the range of feasibility.

A future analysis based on the work in this thesis might profit from the following additions or changes:

- A re-optimization of the measurement phase space by re-evaluating selection cuts.
- Background estimations from data, e. g. for the QCD multi-jet background whose samples got removed in the final steps of this analysis due to limited MC statistics. This was however acceptable due to its negligible contribution to the background model.
- Re-evaluating the choice of the multivariate algorithm used for the discrimination be-

tween tW and $t\bar{t}$ production. Neural networks might be able to achieve better performance than BDTs. In addition, a data-driven training procedure is possible: Since W+jets and tW events have a similar event topology, multivariate algorithms can be trained on heavy-flavour W+jets events where the associated b jet fills the role of the top-quark jet. In order to achieve this, a W+jets region with high purity needs to be defined in the first place.

- Implementation of all systematic uncertainties not yet considered.
- Application of top-tagging scale factors and jet energy corrections for HOTVR (instead of just sub-jet corrections).
- Changing the unfolding method. In this analysis, bin-by-bin unfolding was employed which ignores migrations between bins of the measured observable. However, these migrations must not be ignored in a thorough analysis. A more sophisticated unfolding approach is regularized unfolding as mentioned before.

Beyond improvements of this specific analysis, one can look forward to performing other possible studies on boosted single top-quark production, for instance:

- Measurements of other observables than the transverse momentum of the top quark. As mentioned and demonstrated in Sect. 6.3, measurements of the jet-mass distribution in single boosted top-quark events might be feasible after an optimization of the phase space. Then, an extraction of the top-quark mass would be possible.
- Measurements in other production channels of single top quarks than in the W-associated production channel. Sophisticated differential cross-section measurements in s-channel production are not feasible yet, even in the non-boosted regime. However, there are several differential measurements in the t-channel that might be extended to the boosted kinematic regime.

Appendix

Control Distributions for the Electron Channel

A

In this appendix, control distributions for the electron channel after the preselection and after HOTVR top-tagging are presented, respectively. Equivalent distributions have been shown in Chapter 5 exclusively for the muon channel. In Fig. A.1e and Fig. A.1f, certain trends in the ratio between data and simulation in the electron transverse momentum and relative isolation are observed. It stands to reason that this discrepancy might originate from a certain scale factor which has not been taken into consideration and is thus not applied.

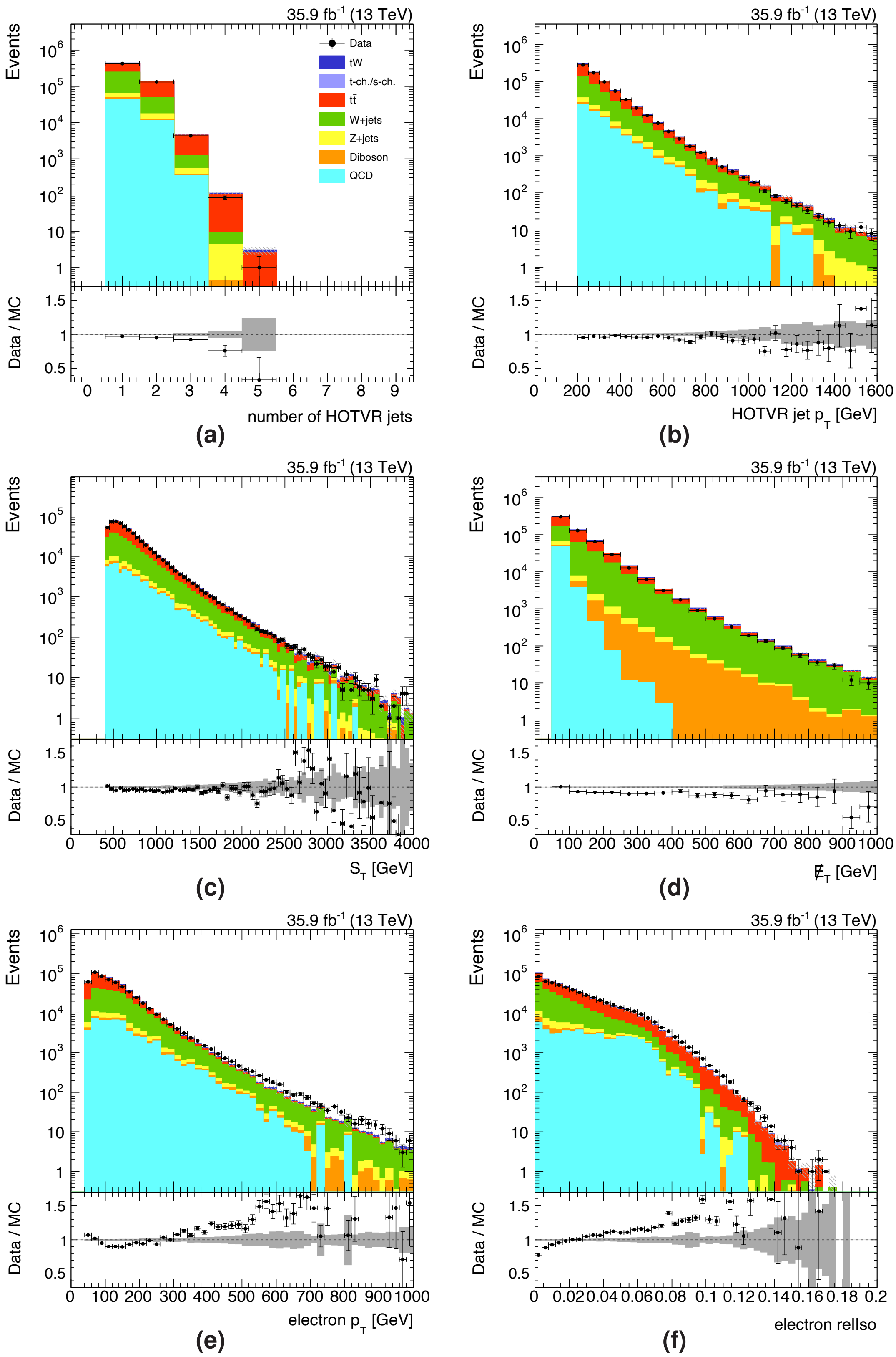

Figure A.1.: Control distributions of the electron channel after the preselection described in Sect. 5.4.1. The **(a)** number of HOTVR jets, the **(b)** transverse momenta of all HOTVR jets, the **(c)** transverse activity, the **(d)** missing transverse energy, the **(e)** transverse momentum of the electron, and the **(f)** relative isolation of the electron are shown. Analogous distributions for the muon channel can be found in Fig. 5.4. Uncertainties on the model prediction represent MC statistics only. The tW signal and other single-top processes are at the top of the histogram stack and, due to the logarithmic scale, barely visible.

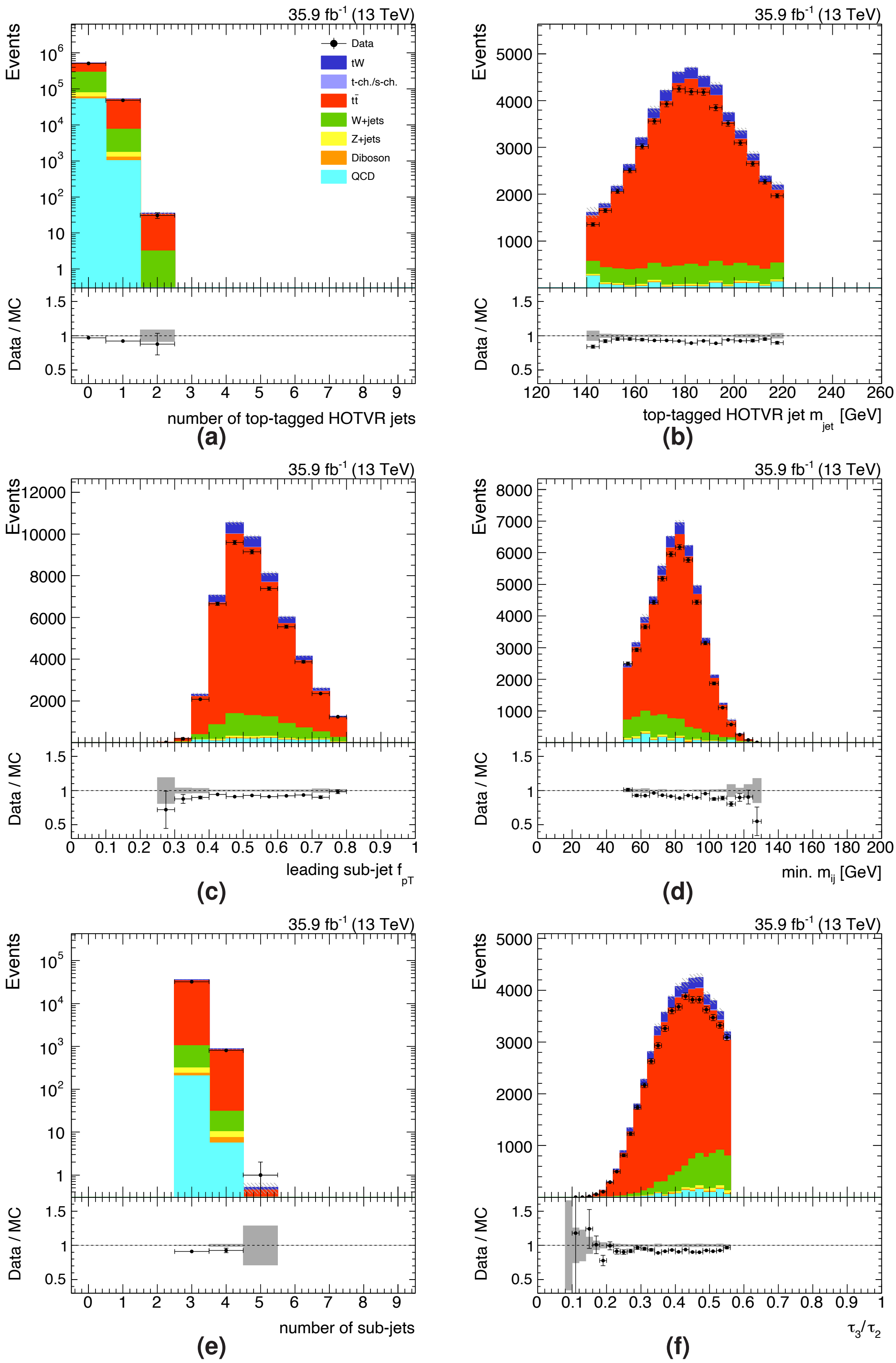

Figure A.2.: Control distributions of top-tagging variables in the muon channel as introduced in Sect. 5.4.2. The **(a)** number of top-tagged HOTVR jets is shown for all events passing the preselection. For events with exactly one top-tag, the following variables of the top-tagged HOTVR jet are shown: The **(b)** jet mass, the **(c)** p_{T} fraction of the leading sub-jet, the **(d)** minimum pairwise invariant mass of the three leading sub-jets, the **(e)** number of sub-jets, and the **(f)** N-subjettiness ratio. Analogous distributions for the muon channel can be found in Fig. 5.6. Uncertainties on the model prediction represent MC statistics only.

Maximum-Likelihood Fit Results B

In this appendix, the results of all sixteen maximum-likelihood template fits, as described in Sect. 7.2, are presented. For the discussion of the results, see Sect. 7.2.2.

The pre-fit BDT response distributions, which are shown for comparison to their post-fit variants, include MC statistical uncertainties (inner dark grey band within the data/MC ratio plots) and all systematic uncertainties described in Sect. 7.1, excluding luminosity, lepton trigger, lepton identification, and all cross-section normalization uncertainties. The post-fit BDT distributions include the constrained uncertainties of the same sources as the pre-fit distributions, however including the constrained cross-section normalization uncertainties. Total uncertainties of the predicted model are depicted as light grey error band within the data/MC ratio plot and as hatched area on the histogram stack. Error bars on data points indicate their associated statistical uncertainties.

In addition, the post-fit values of the nuisance parameters of the prediction models and their constrained uncertainties are shown. Post-fit values are given as deviations from their respective pre-fit values, given in units of the prior uncertainty. The band of one (two) standard deviation(s) of the pre-fit values is depicted as green (yellow) area.

Linear correlation matrices for all nuisance parameters included in each fit are shown as well. Correlations are given in percent, ranging between $+100$ % (fully correlated) and -100 % (fully anti-correlated). A value of zero (or in these plots rather an empty bin) implies that these two nuisance parameters are found to have no correlation in the fit.

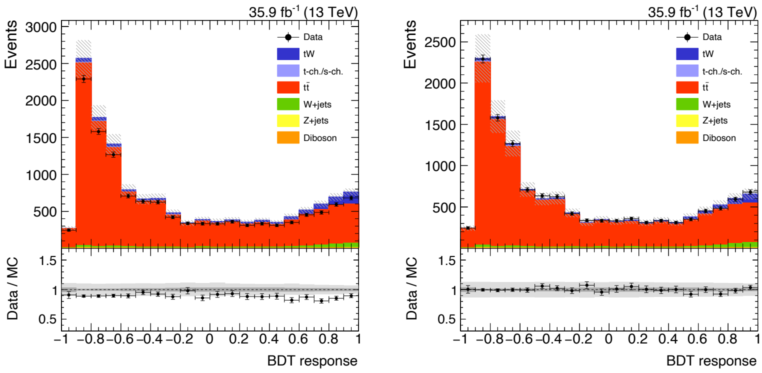

(a) top-jet $p_{\mathrm{T}} \in (200, 300]$ GeV

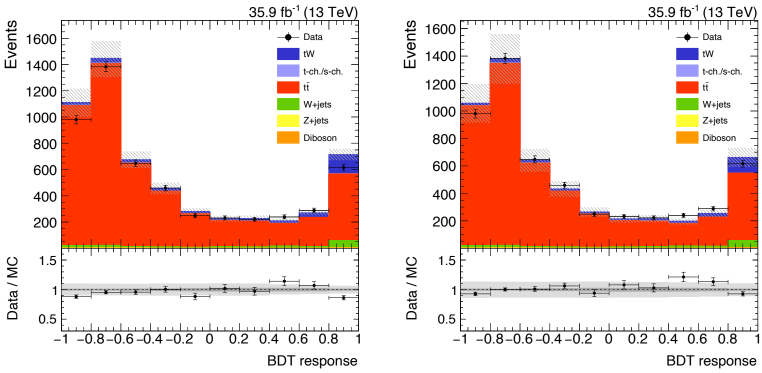

(b) top-jet $p_{\mathrm{T}} \in (300, 400]$ GeV

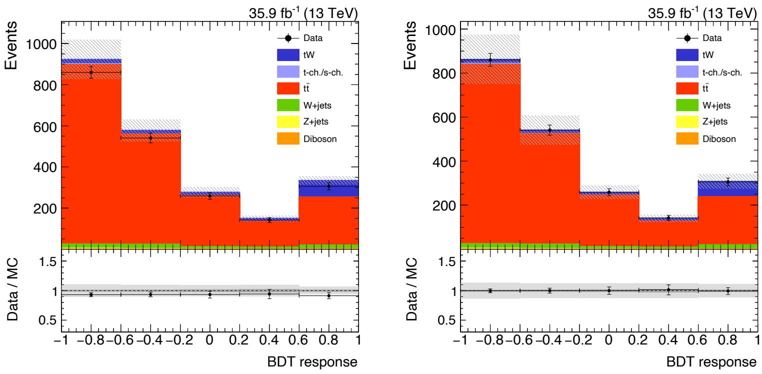

(c) top-jet $p_{\mathrm{T}} \in (400, 600]$ GeV

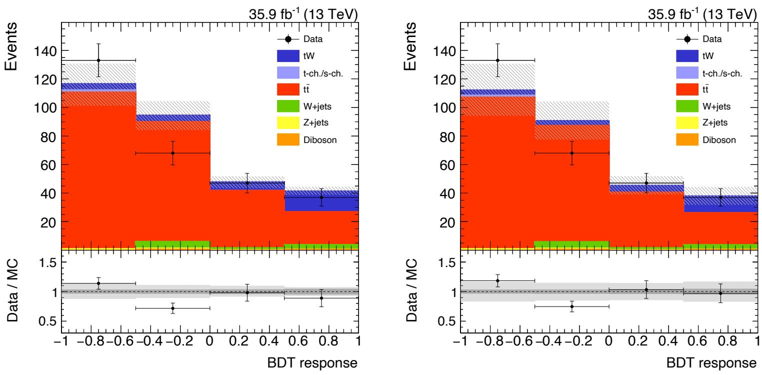

(d) top-jet $p_{\mathrm{T}} \in (600, 1200]$ GeV

Figure B.1.: Pre-fit (left) vs. post-fit (right) BDT outputs, **electron** channel, `1t1b` category.

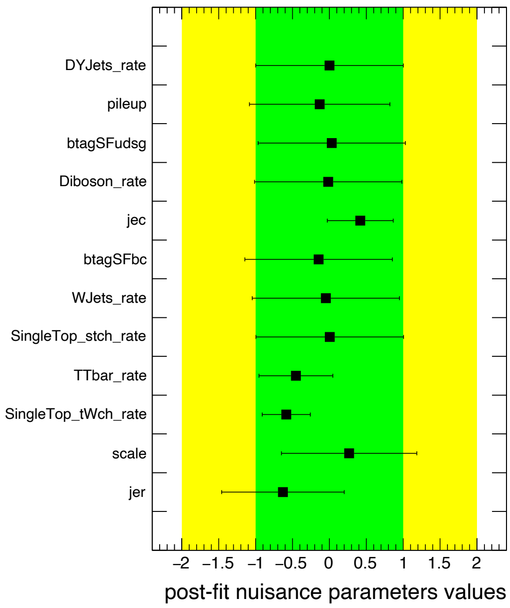

(a) top-jet $p_{\mathrm{T}} \in (200, 300]$ GeV

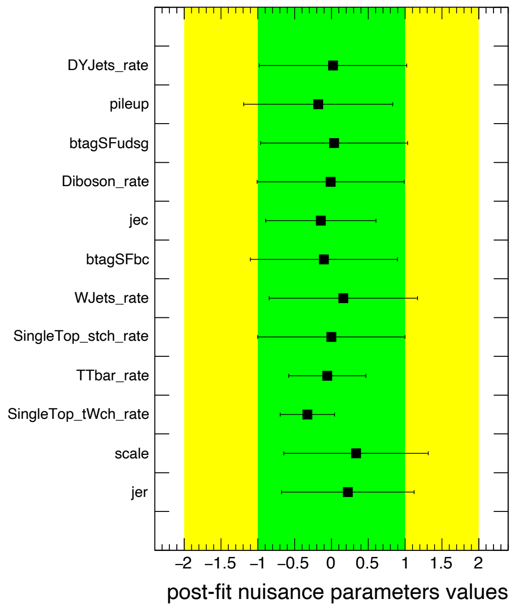

(b) top-jet $p_{\mathrm{T}} \in (300, 400]$ GeV

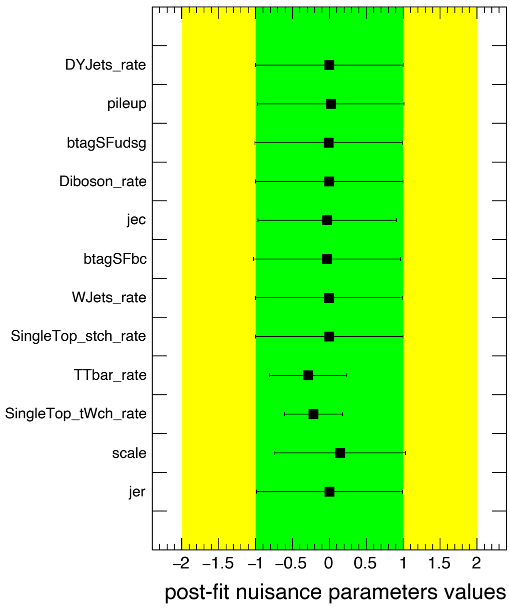

(c) top-jet $p_{\mathrm{T}} \in (400, 600]$ GeV

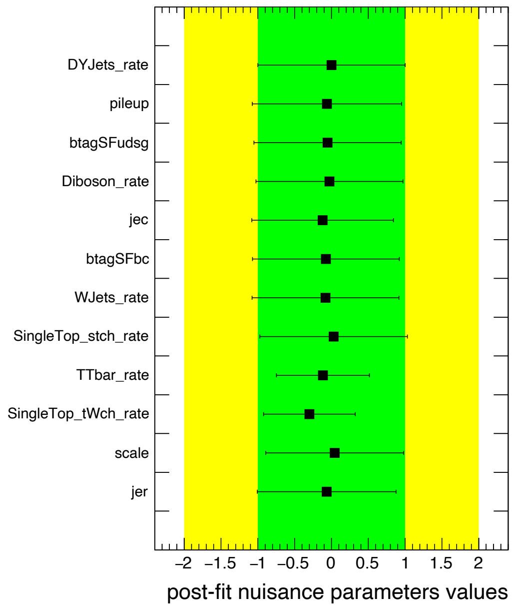

(d) top-jet $p_{\mathrm{T}} \in (600, 1200]$ GeV

Figure B.2.: Post-fit values of nuisance parameters, **electron** channel, `1t1b` category.

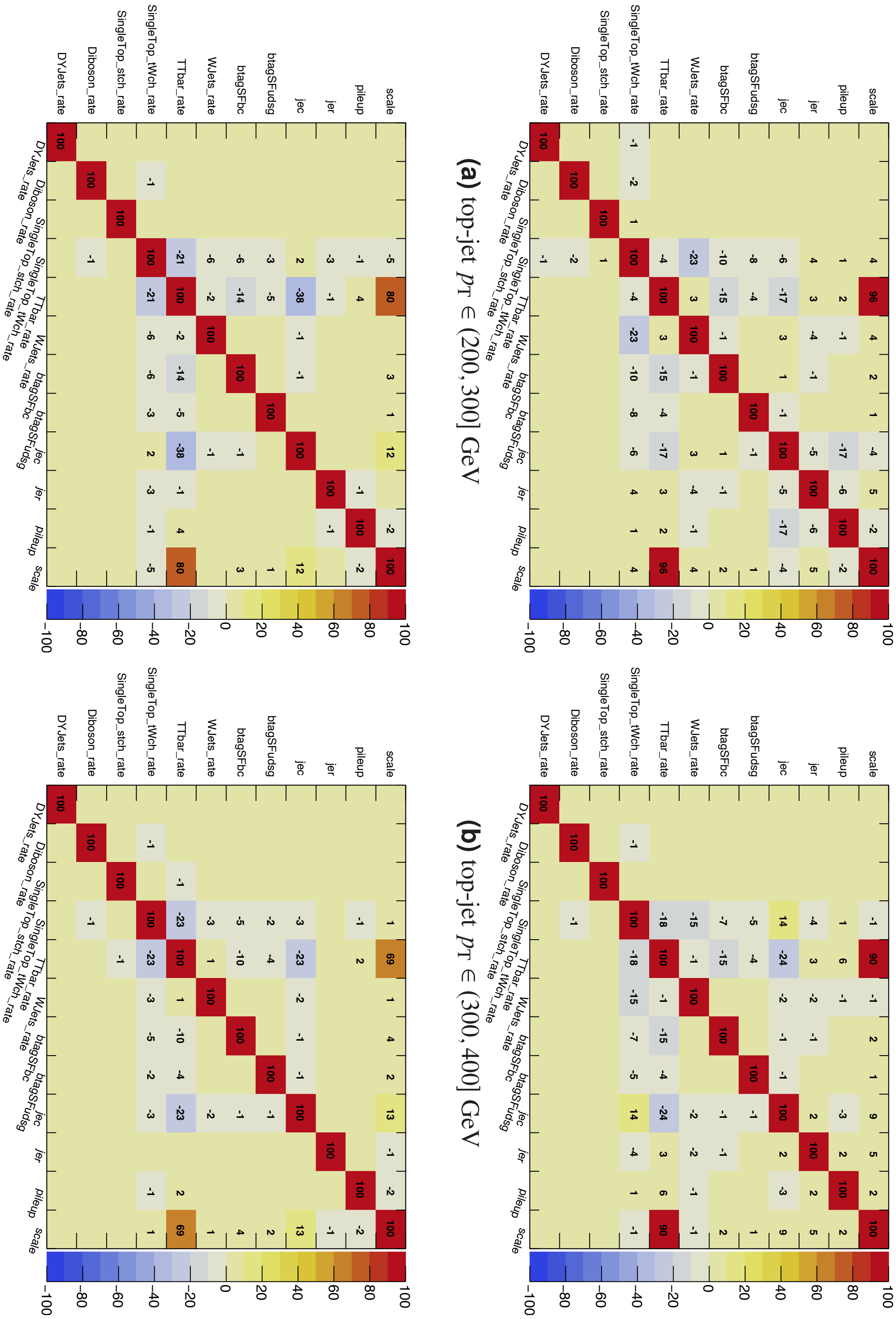

(a) top-jet $p_T \in (200, 300]$ GeV

(b) top-jet $p_T \in (300, 400]$ GeV

(c) top-jet $p_T \in (400, 600]$ GeV

(d) top-jet $p_T \in (600, 1200]$ GeV

Figure B.3.: Linear correlations between nuisance parameters in the **electron** channel, 1t+1b category. Values are given in percent.

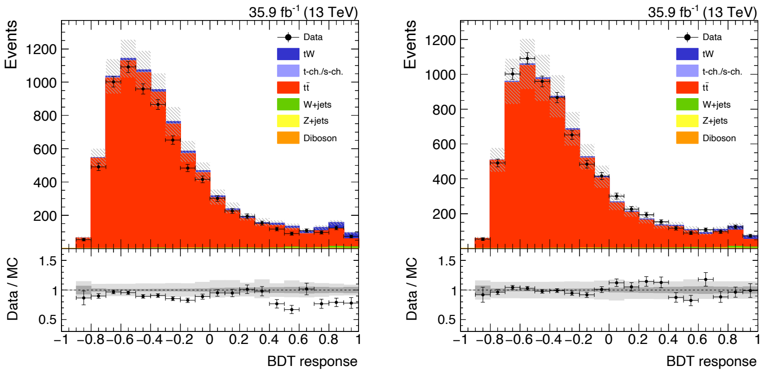

(a) top-jet $p_{\mathrm{T}} \in (200, 300]$ GeV

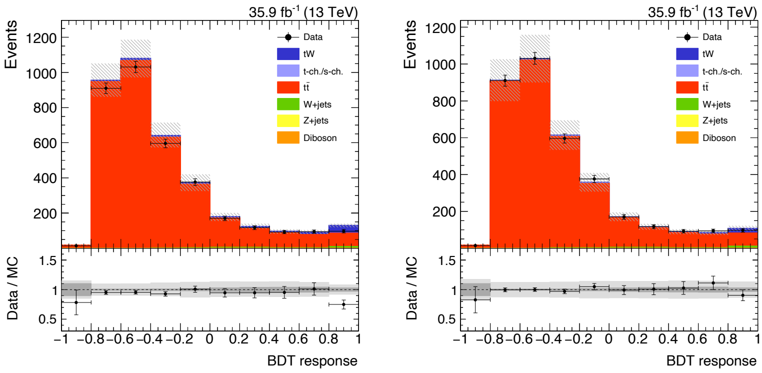

(b) top-jet $p_{\mathrm{T}} \in (300, 400]$ GeV

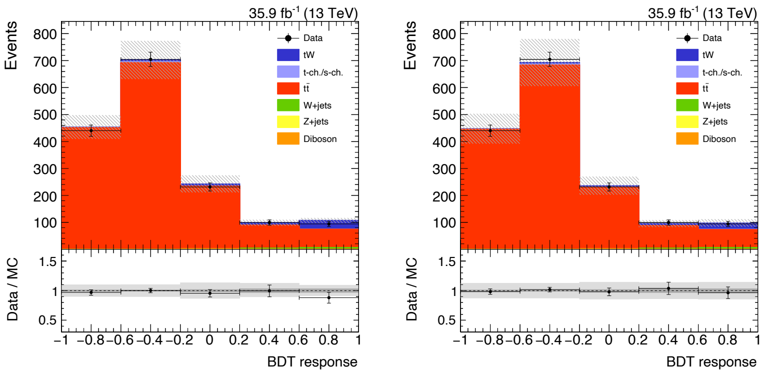

(c) top-jet $p_{\mathrm{T}} \in (400, 600]$ GeV

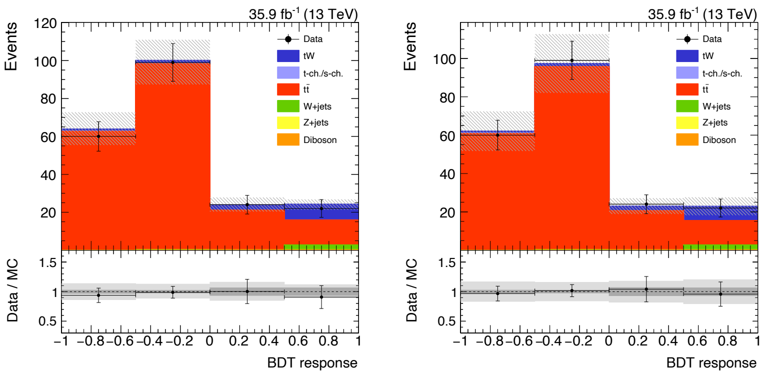

(d) top-jet $p_{\mathrm{T}} \in (600, 1200]$ GeV

Figure B.4.: Pre-fit (left) vs. post-fit (right) BDT outputs, **electron** channel, `1t2b+` category.

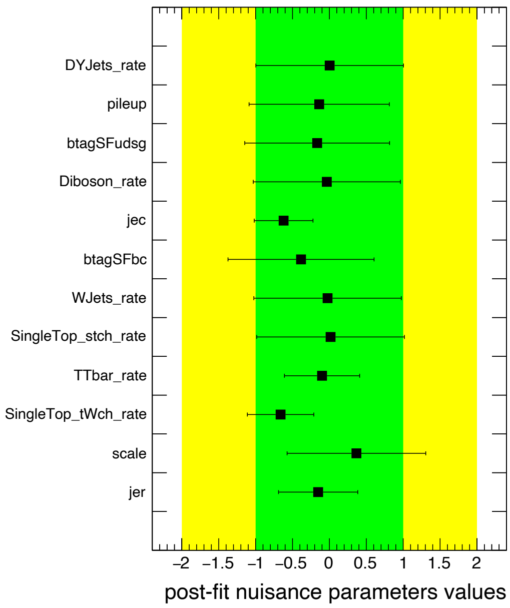

(a) top-jet $p_{\mathrm{T}} \in (200, 300]$ GeV

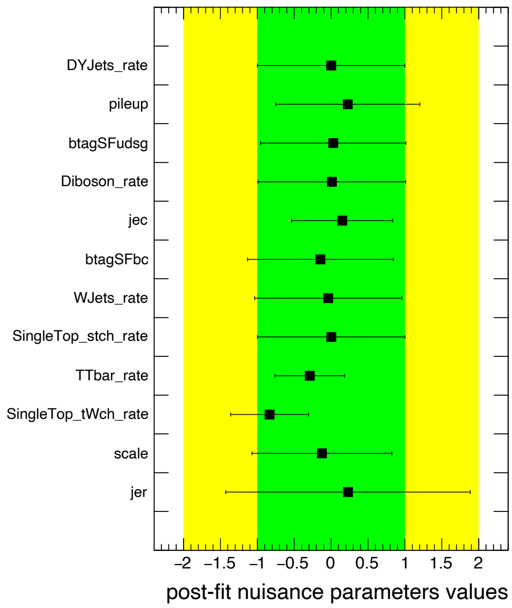

(b) top-jet $p_{\mathrm{T}} \in (300, 400]$ GeV

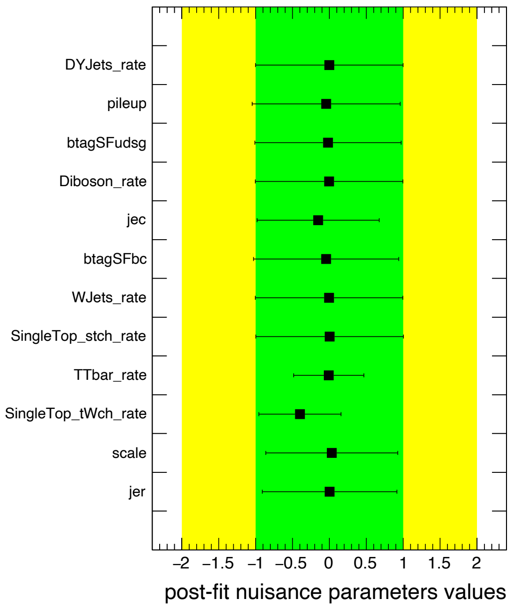

(c) top-jet $p_{\mathrm{T}} \in (400, 600]$ GeV

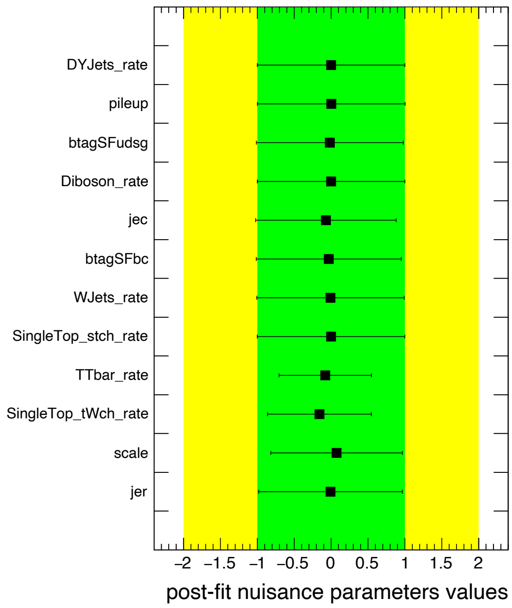

(d) top-jet $p_{\mathrm{T}} \in (600, 1200]$ GeV

Figure B.5.: Post-fit values of nuisance parameters, **electron** channel, `1t2b+` category.

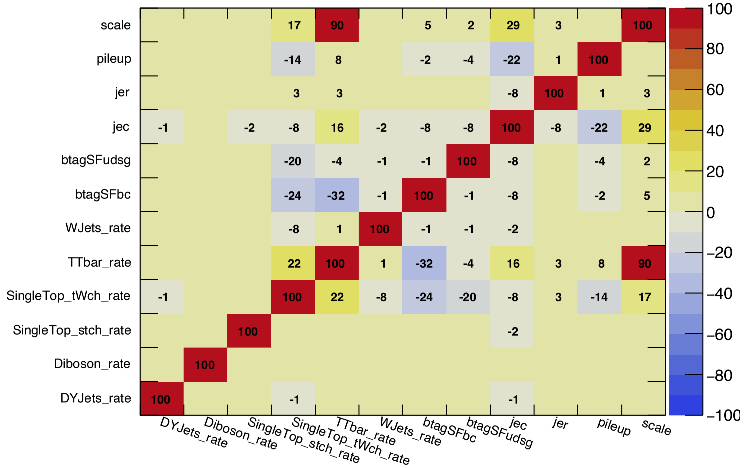

(a) top-jet $p_T \in (200, 300]$ GeV

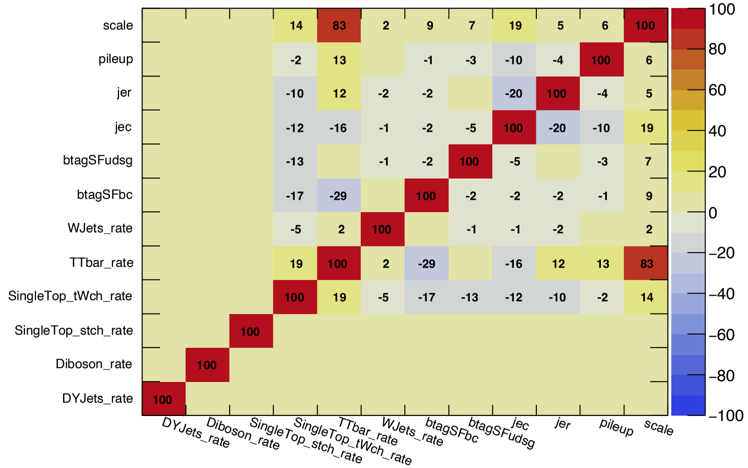

(b) top-jet $p_T \in (300, 400]$ GeV

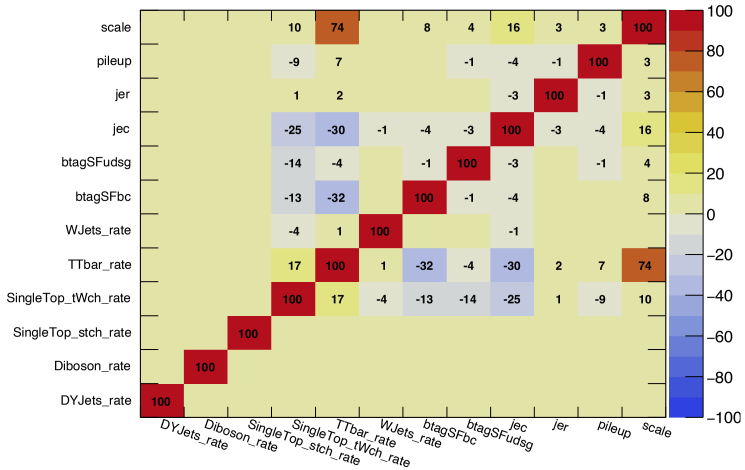

(c) top-jet $p_T \in (400, 600]$ GeV

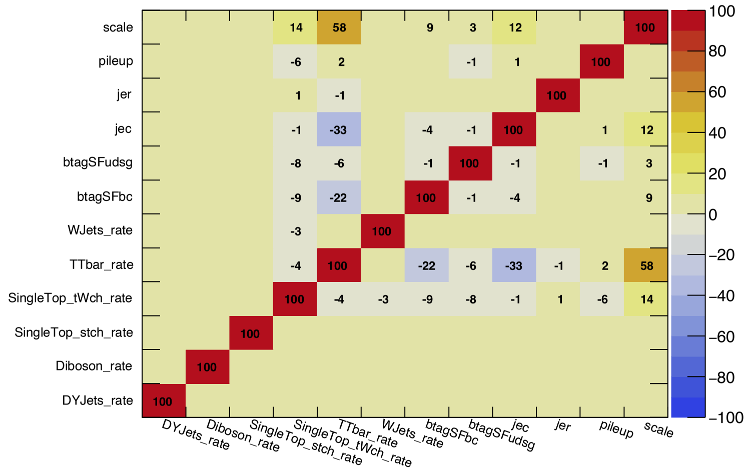

(d) top-jet $p_T \in (600, 1200]$ GeV

Figure B.6.: Linear correlations between nuisance parameters in the **electron** channel, 1t2b+ category. Values are given in percent.

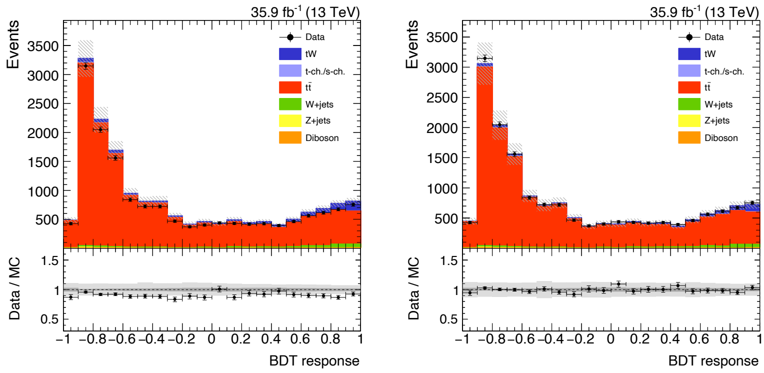

(a) top-jet $p_T \in (200, 300]$ GeV

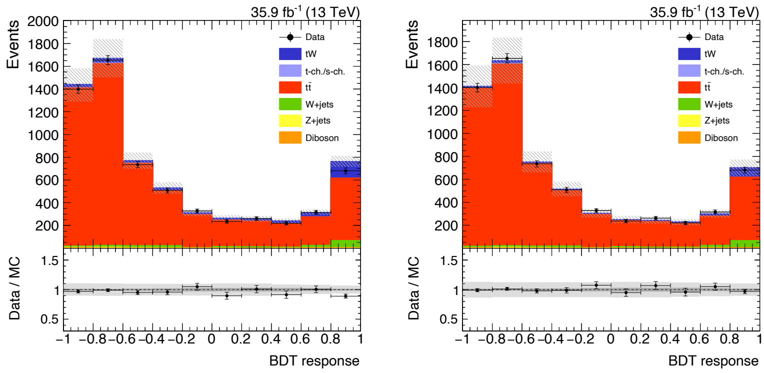

(b) top-jet $p_T \in (300, 400]$ GeV

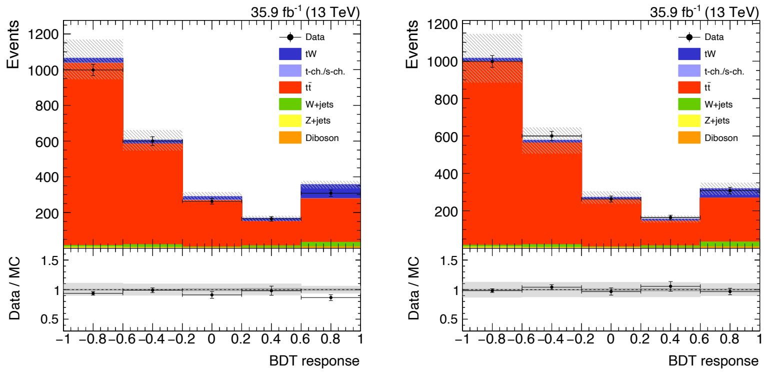

(c) top-jet $p_T \in (400, 600]$ GeV

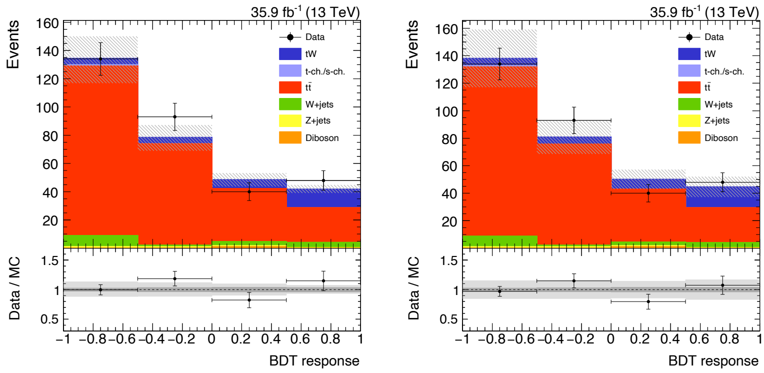

(d) top-jet $p_T \in (600, 1200]$ GeV

Figure B.7.: Pre-fit (left) vs. post-fit (right) BDT outputs, **muon** channel, `1t1b` category.

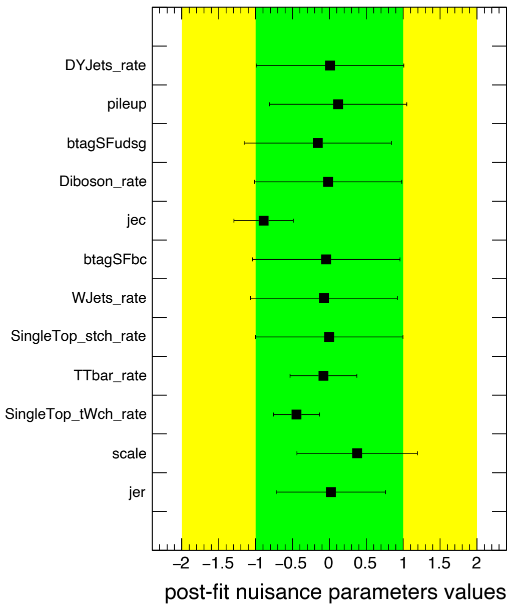

(a) top-jet $p_{\mathrm{T}} \in (200, 300]$ GeV

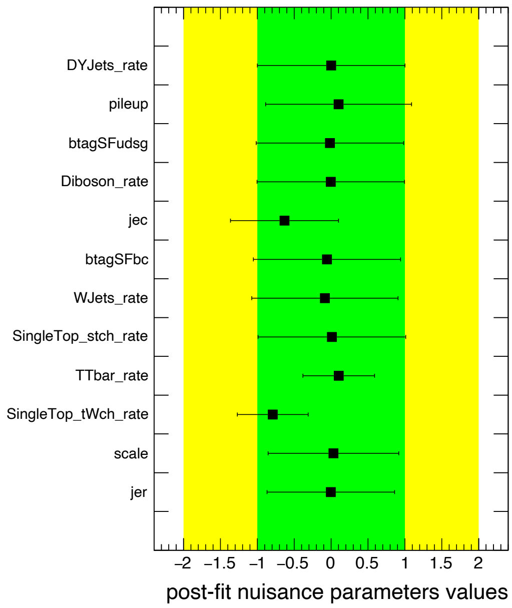

(b) top-jet $p_{\mathrm{T}} \in (300, 400]$ GeV

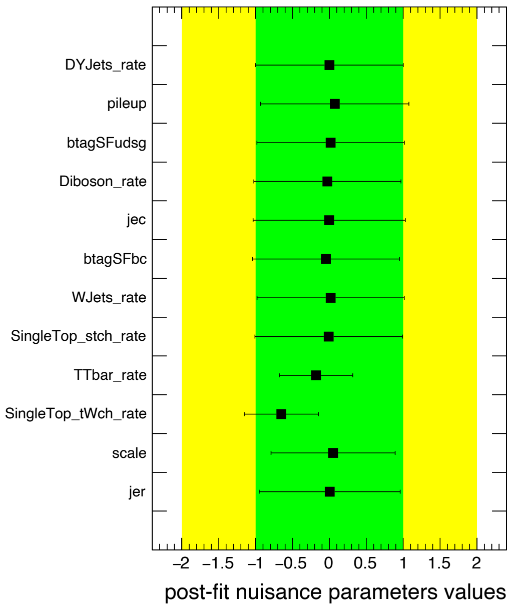

(c) top-jet $p_{\mathrm{T}} \in (400, 600]$ GeV

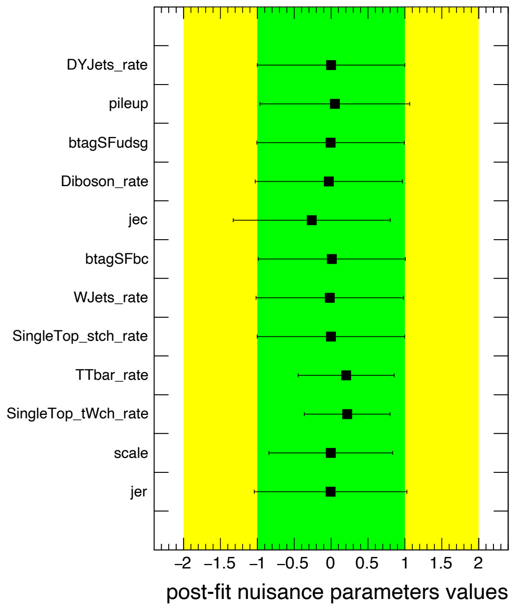

(d) top-jet $p_{\mathrm{T}} \in (600, 1200]$ GeV

Figure B.8.: Post-fit values of nuisance parameters, **muon** channel, `1t1b` category.

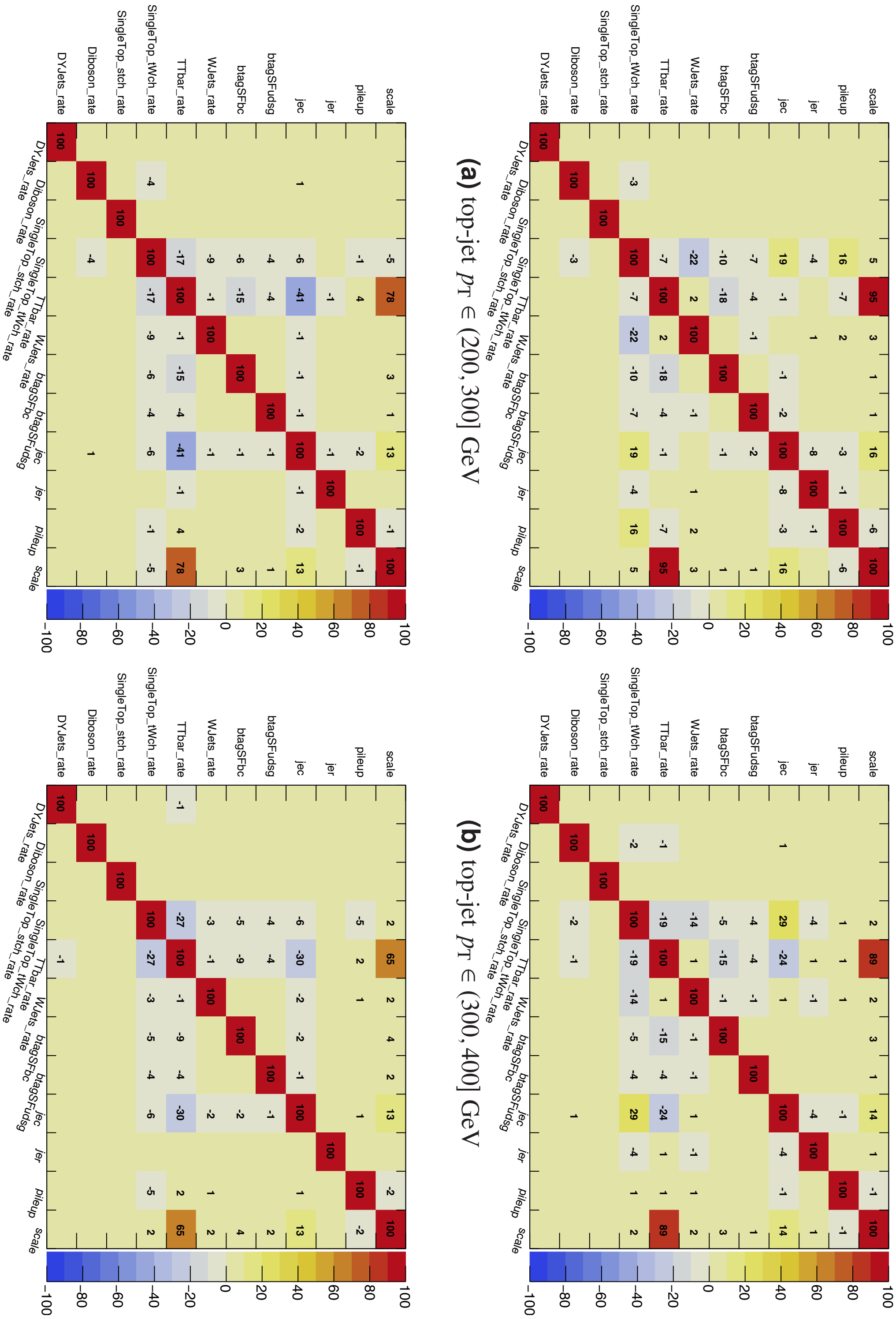

(a) top-jet $p_T \in (200, 300]$ GeV

(b) top-jet $p_T \in (300, 400]$ GeV

(c) top-jet $p_T \in (400, 600]$ GeV

(d) top-jet $p_T \in (600, 1200]$ GeV

Figure B.9.: Linear correlations between nuisance parameters in the **muon** channel, 1t+1b category. Values are given in percent.

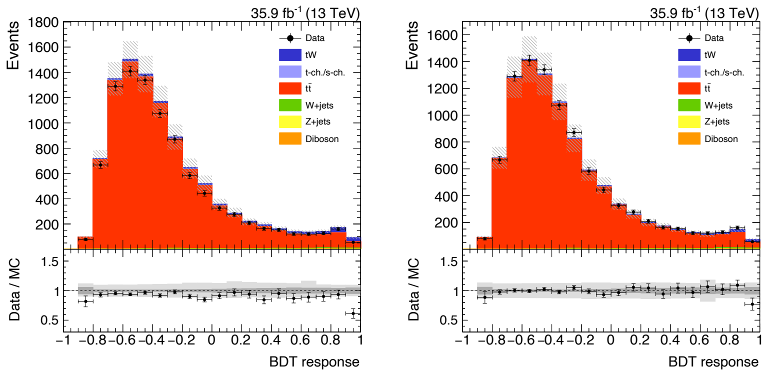

(a) top-jet $p_{\mathrm{T}} \in (200, 300]$ GeV

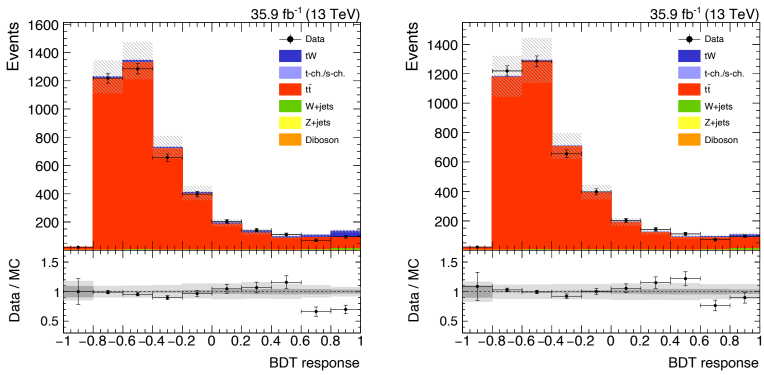

(b) top-jet $p_{\mathrm{T}} \in (300, 400]$ GeV

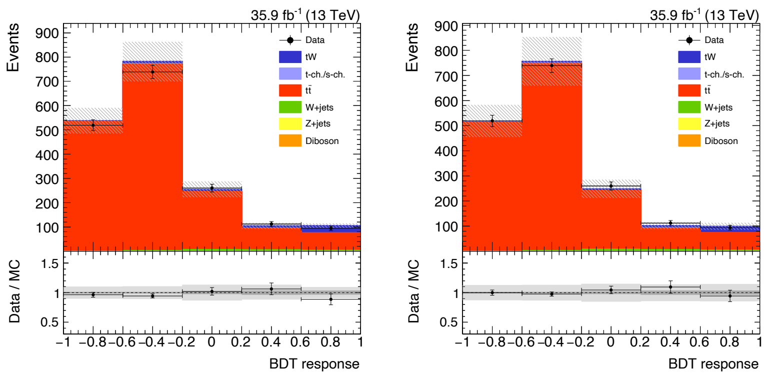

(c) top-jet $p_{\mathrm{T}} \in (400, 600]$ GeV

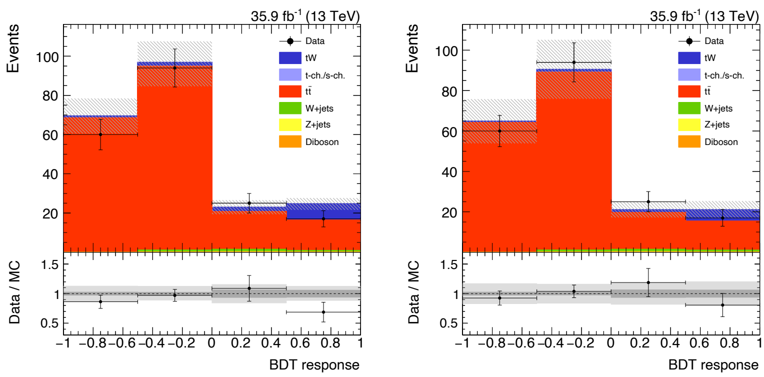

(d) top-jet $p_{\mathrm{T}} \in (600, 1200]$ GeV

Figure B.10.: Pre-fit (left) vs. post-fit (right) BDT outputs, **muon** channel, `1t2b+` category.

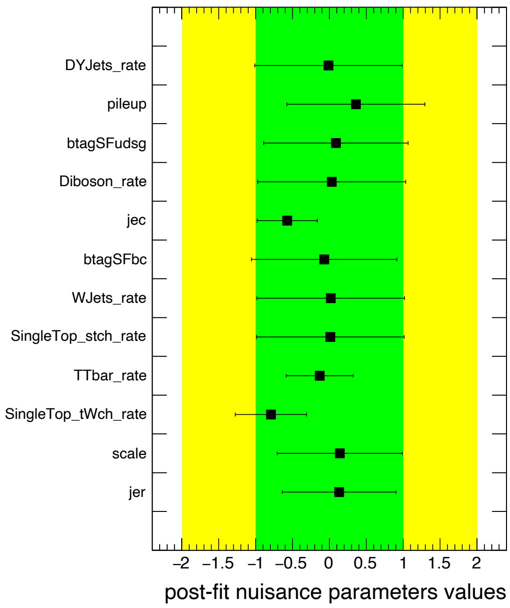

(a) top-jet $p_T \in (200, 300]$ GeV

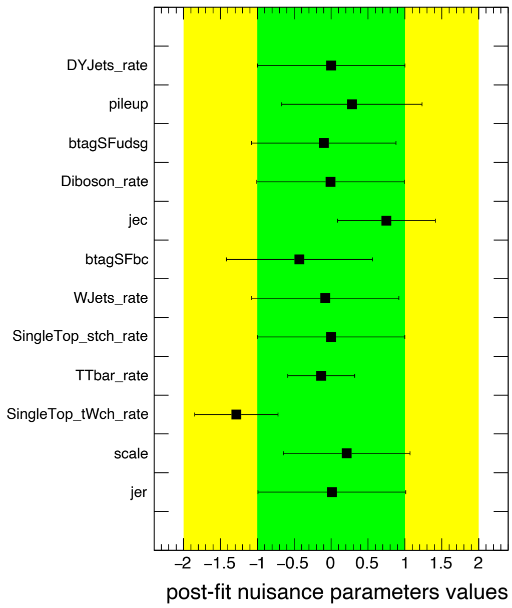

(b) top-jet $p_T \in (300, 400]$ GeV

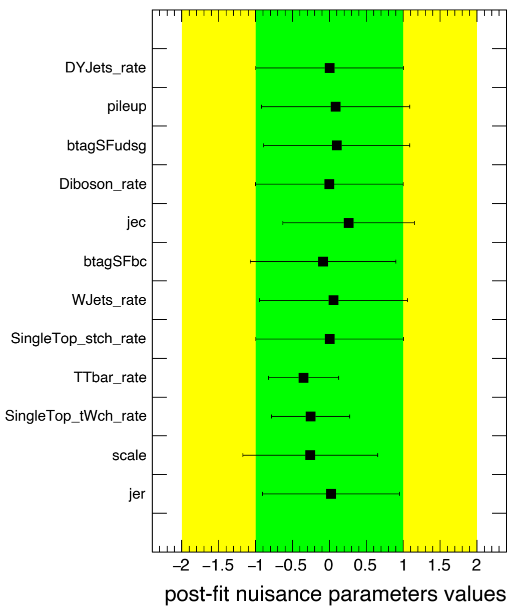

(c) top-jet $p_T \in (400, 600]$ GeV

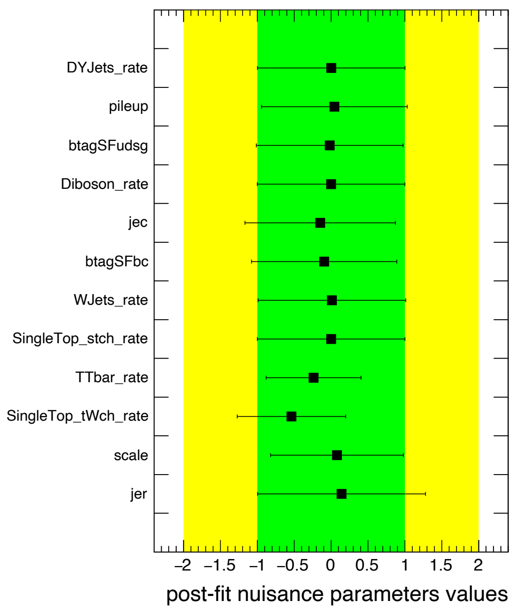

(d) top-jet $p_T \in (600, 1200]$ GeV

Figure B.11.: Post-fit values of nuisance parameters, **muon** channel, `1t2b+` category.

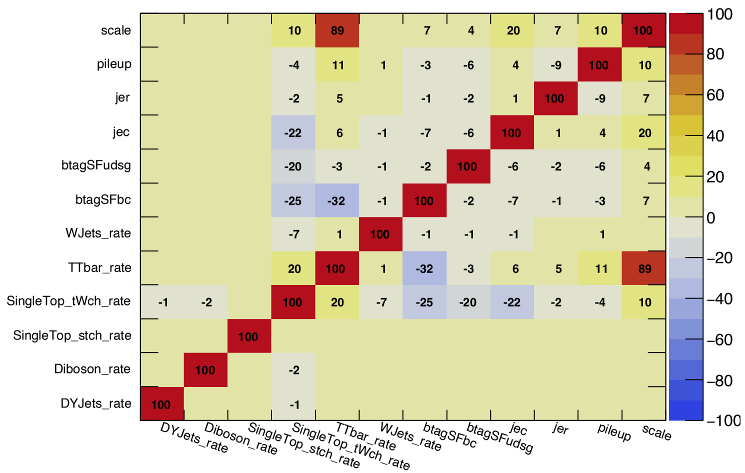

(a) top-jet $p_{\mathrm{T}} \in (200, 300]$ GeV

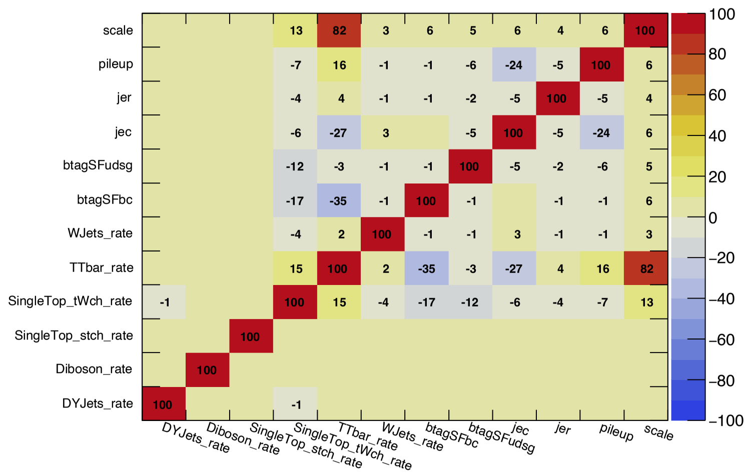

(b) top-jet $p_{\mathrm{T}} \in (300, 400]$ GeV

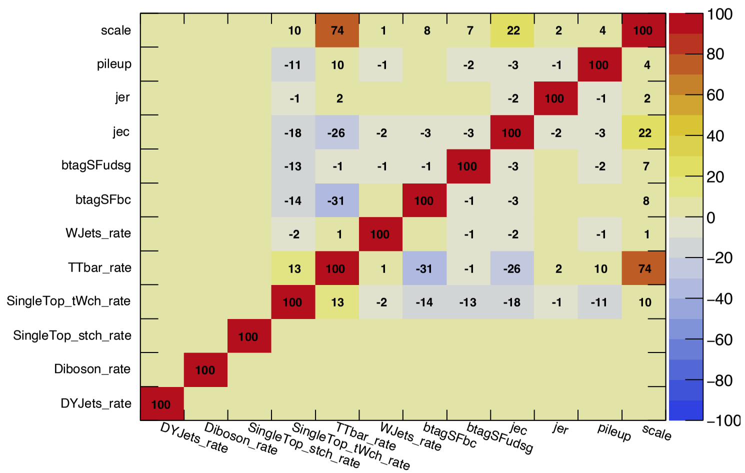

(c) top-jet $p_{\mathrm{T}} \in (400, 600]$ GeV

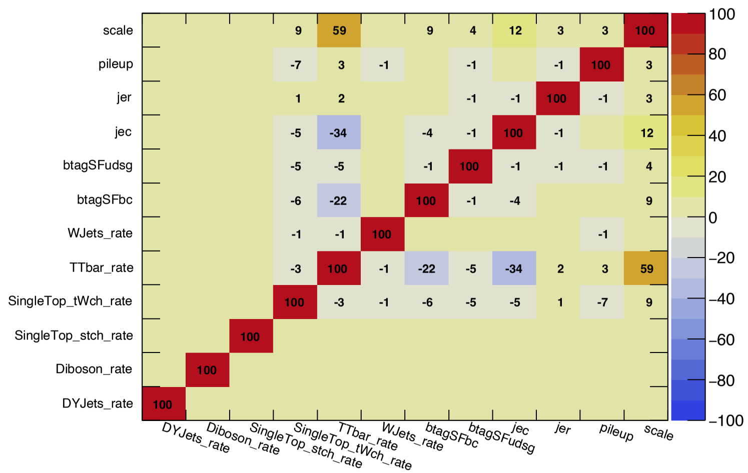

(d) top-jet $p_{\mathrm{T}} \in (600, 1200]$ GeV

Figure B.12.: Linear correlations between nuisance parameters in the **muon** channel, `1t2b+` category. Values are given in percent.

Bibliography

[1] **CDF** Collaboration, "Observation of Top Quark Production in $\bar{p}p$ Collisions", *Phys. Rev. Lett.* **74** (1995) 2626–2631, doi:10.1103/PhysRevLett.74.2626, `arXiv:hep-ex/9503002`.

[2] **D0** Collaboration, "Observation of the Top Quark", *Phys. Rev. Lett.* **74** (1995) 2632–2637, doi:10.1103/PhysRevLett.74.2632, `arXiv:hep-ex/9503003`.

[3] M. Kobayashi and T. Maskawa, "CP-Violation in the Renormalizable Theory of Weak Interaction", *Progress of Theoretical Physics* **49** no. 2, (1973) 652–657, doi:10.1143/PTP.49.652.

[4] J. H. Christenson, J. W. Cronin, V. L. Fitch, and R. Turlay, "Evidence for the 2π Decay of the K_2^0 Meson", *Phys. Rev. Lett.* **13** (1964) 138–140, doi:10.1103/PhysRevLett.13.138.

[5] C. P. Burgess and G. D. Moore, *The Standard Model: A Primer*. Cambridge University Press, 2007.

[6] M. E. Peskin and D. V. Schroeder, *An Introduction to Quantum Field Theory*. Westview, Boulder, CO, 1995. `https://cds.cern.ch/record/257493`. Includes exercises.

[7] G. 't Hooft, "The Evolution of Quantum Field Theory, From QED to Grand Unification", *Adv. Ser. Direct. High Energy Phys.* **26** (2016) 1–27, doi:10.1142/9789814733519_0001, `arXiv:1503.05007`.

[8] **ATLAS** Collaboration, "Observation of a new particle in the search for the Standard Model Higgs boson with the ATLAS detector at the LHC", *Phys. Lett.* **B716** (2012) 1–29, doi:10.1016/j.physletb.2012.08.020, `arXiv:1207.7214`.

[9] **CMS** Collaboration, "Observation of a new boson at a mass of 125 GeV with the CMS experiment at the LHC", *Phys. Lett.* **B716** (2012) 30–61, doi:10.1016/j.physletb.2012.08.021, `arXiv:1207.7235`.

[10] G. 't Hooft and M. J. G. Veltman, "Regularization and Renormalization of Gauge Fields", *Nucl. Phys.* **B44** (1972) 189–213, doi:10.1016/0550-3213(72)90279-9.

[11] A. Einstein, “Die Grundlage der allgemeinen Relativitätstheorie”, *Annalen der Physik* **354** no. 7, (1916) 769–822, doi:10.1002/andp.19163540702.

[12] **Particle Data Group** Collaboration, “Review of Particle Physics”, *Chin. Phys.* **C40** no. 10, (2016) 100001, doi:10.1088/1674-1137/40/10/100001.

[13] **CMS** Collaboration, “Measurement of the top quark mass using proton-proton data at $\sqrt{s} = 7$ and 8 TeV”, *Phys. Rev.* **D93** no. 7, (2016) 072004, doi:10.1103/PhysRevD.93.072004, `arXiv:1509.04044`.

[14] M. Lindner, T. Ohlsson, and G. Seidl, “Seesaw mechanisms for Dirac and Majorana neutrino masses”, *Phys. Rev.* **D65** (2002) 053014, doi:10.1103/PhysRevD.65.053014, `arXiv:hep-ph/0109264`.

[15] `https://commons.wikimedia.org/wiki/File:Elementary_particle_interactions.svg` [accessed: 2018-11-29].

[16] **LHCb** Collaboration, “Observation of $J/\psi\phi$ structures consistent with exotic states from amplitude analysis of $B^+ \to J/\psi\phi K^+$ decays”, *Phys. Rev. Lett.* **118** no. 2, (2017) 022003, doi:10.1103/PhysRevLett.118.022003, `arXiv:1606.07895`.

[17] **LHCb** Collaboration, “Observation of $J/\psi p$ Resonances Consistent with Pentaquark States in $\Lambda_b^0 \to J/\psi K^- p$ Decays”, *Phys. Rev. Lett.* **115** (2015) 072001, doi:10.1103/PhysRevLett.115.072001, `arXiv:1507.03414`.

[18] D. Chakraborty, J. Konigsberg, and D. L. Rainwater, “Review of top quark physics”, *Ann. Rev. Nucl. Part. Sci.* **53** (2003) 301–351, doi:10.1146/annurev.nucl.53.041002.110601, `arXiv:hep-ph/0303092`.

[19] U. Husemann, “Top-Quark Physics: Status and Prospects”, *Prog. Part. Nucl. Phys.* **95** (2017) 48–97, doi:10.1016/j.ppnp.2017.03.002, `arXiv:1704.01356`.

[20] **DELPHI, OPAL, ALEPH, LEP Electroweak Working Group, L3** Collaboration, “Combined preliminary data on Z parameters from the LEP experiments and constraints on the Standard Model”, in *27th International Conference on High-energy Physics (ICHEP 94) Glasgow, Scotland, July 20-27, 1994*. 1994.

[21] J. Haller, A. Hoecker, R. Kogler, K. Mönig, T. Peiffer, and J. Stelzer, “Update of the global electroweak fit and constraints on two-Higgs-doublet models”, *Eur. Phys. J.* **C78** no. 8, (2018) 675, doi:10.1140/epjc/s10052-018-6131-3, `arXiv:1803.01853`.

[22] C. Csáki and P. Tanedo, “Beyond the Standard Model”, in *Proceedings, 2013 European School of High-Energy Physics (ESHEP 2013): Paradfurdo, Hungary, June 5-18, 2013*, pp. 169–268. 2015. `arXiv:1602.04228`.

[23] A. Djouadi and A. Lenz, "Sealing the fate of a fourth generation of fermions", *Phys. Lett.* **B715** (2012) 310–314, doi:10.1016/j.physletb.2012.07.060, arXiv:1204.1252.

[24] O. Eberhardt, G. Herbert, H. Lacker, A. Lenz, A. Menzel, U. Nierste, and M. Wiebusch, "Impact of a Higgs boson at a mass of 126 GeV on the standard model with three and four fermion generations", *Phys. Rev. Lett.* **109** (2012) 241802, doi:10.1103/PhysRevLett.109.241802, arXiv:1209.1101.

[25] J. Alwall, R. Frederix, J. M. Gerard, A. Giammanco, M. Herquet, S. Kalinin, E. Kou, V. Lemaitre, and F. Maltoni, "Is $V_{\mathrm{tb}} \simeq 1$?", *Eur. Phys. J.* **C49** (2007) 791–801, doi:10.1140/epjc/s10052-006-0137-y, arXiv:hep-ph/0607115.

[26] **D0** Collaboration, "Observation of Single Top Quark Production", *Phys. Rev. Lett.* **103** (2009) 092001, doi:10.1103/PhysRevLett.103.092001, arXiv:0903.0850.

[27] **CDF** Collaboration, "First Observation of Electroweak Single Top Quark Production", *Phys. Rev. Lett.* **103** (2009) 092002, doi:10.1103/PhysRevLett.103.092002, arXiv:0903.0885.

[28] **D0** Collaboration, "Evidence for production of single top quarks and first direct measurement of $|V_{\mathrm{tb}}|$", *Phys. Rev. Lett.* **98** (2007) 181802, doi:10.1103/PhysRevLett.98.181802, arXiv:hep-ex/0612052.

[29] R. K. Ellis, W. J. Stirling, and B. R. Webber, *QCD and Collider Physics*. Cambridge monographs on particle physics, nuclear physics, and cosmology. Cambridge University Press, Cambridge, 2003. https://cds.cern.ch/record/318585. Photography by S. Vascotto.

[30] A. D. Martin, W. J. Stirling, R. S. Thorne, and G. Watt, "Parton distributions for the LHC", *Eur. Phys. J.* **C63** (2009) 189–285, doi:10.1140/epjc/s10052-009-1072-5, arXiv:0901.0002.

[31] **CMS** Collaboration, "Measurement of the differential cross section and charge asymmetry for inclusive $\mathrm{pp} \rightarrow \mathrm{W}^{\pm} + X$ production at $\sqrt{s} = 8$ TeV", *Eur. Phys. J.* **C76** no. 8, (2016) 469, doi:10.1140/epjc/s10052-016-4293-4, arXiv:1603.01803.

[32] H.-W. Lin *et al.*, "Parton distributions and lattice QCD calculations: a community white paper", *Prog. Part. Nucl. Phys.* **100** (2018) 107–160, doi:10.1016/j.ppnp.2018.01.007, arXiv:1711.07916.

[33] **TOTEM** Collaboration, "First measurement of elastic, inelastic and total cross-section at $\sqrt{s} = 13$ TeV by TOTEM and overview of cross-section data at LHC energies", arXiv:1712.06153.

[34] **ATLAS** Collaboration, "Observation of top-quark pair production in association with a photon and measurement of the $t\bar{t}\gamma$ production cross section in pp collisions at $\sqrt{s} = 7$ TeV using the ATLAS detector", *Phys. Rev.* **D91** no. 7, (2015) 072007, doi:10.1103/PhysRevD.91.072007, `arXiv:1502.00586`.

[35] **CMS** Collaboration, "Measurement of the cross section for top quark pair production in association with a W or Z boson in proton-proton collisions at $\sqrt{s} = 13$ TeV", *JHEP* **08** (2018) 011, doi:10.1007/JHEP08(2018)011, `arXiv:1711.02547`.

[36] **CMS** Collaboration, "Search for standard model production of four top quarks in proton-proton collisions at $\sqrt{s} = 13$ TeV", *Phys. Lett.* **B772** (2017) 336–358, doi:10.1016/j.physletb.2017.06.064, `arXiv:1702.06164`.

[37] **CMS** Collaboration, "Observation of $t\bar{t}$H production", *Phys. Rev. Lett.* **120** no. 23, (2018) 231801, doi:10.1103/PhysRevLett.120.231801, 10.1130/PhysRevLett.120.231801, `arXiv:1804.02610`.

[38] **ATLAS** Collaboration, "Observation of Higgs boson production in association with a top quark pair at the LHC with the ATLAS detector", *Phys. Lett.* **B784** (2018) 173–191, doi:10.1016/j.physletb.2018.07.035, `arXiv:1806.00425`.

[39] `https://twiki.cern.ch/twiki/bin/view/LHCPhysics/TtbarNNLO` [accessed: 2018-11-29].

[40] M. Czakon and A. Mitov, "Top++: A Program for the Calculation of the Top-Pair Cross-Section at Hadron Colliders", *Comput. Phys. Commun.* **185** (2014) 2930, doi:10.1016/j.cpc.2014.06.021, `arXiv:1112.5675`.

[41] M. Botje *et al.*, "The PDF4LHC Working Group Interim Recommendations", `arXiv:1101.0538`.

[42] A. D. Martin, W. J. Stirling, R. S. Thorne, and G. Watt, "Uncertainties on α_s in global PDF analyses and implications for predicted hadronic cross sections", *Eur. Phys. J.* **C64** (2009) 653–680, doi:10.1140/epjc/s10052-009-1164-2, `arXiv:0905.3531`.

[43] J. Gao, M. Guzzi, J. Huston, H.-L. Lai, Z. Li, P. Nadolsky, J. Pumplin, D. Stump, and C. P. Yuan, "CT10 next-to-next-to-leading order global analysis of QCD", *Phys. Rev.* **D89** no. 3, (2014) 033009, doi:10.1103/PhysRevD.89.033009, `arXiv:1302.6246`.

[44] R. D. Ball *et al.*, "Parton distributions with LHC data", *Nucl. Phys.* **B867** (2013) 244–289, doi:10.1016/j.nuclphysb.2012.10.003, `arXiv:1207.1303`.

[45] E. Boos and L. Dudko, "The Single Top Quark Physics", *Int. J. Mod. Phys.* **A27** (2012) 1230026, doi:10.1142/S0217751X12300268, `arXiv:1211.7146`.

[46] S. S. D. Willenbrock and D. A. Dicus, “Production of heavy quarks from W-gluon fusion”, *Phys. Rev. D* **34** (Jul, 1986) 155–161, doi:10.1103/PhysRevD.34.155.

[47] **CMS** Collaboration, “Measurement of the associated production of a single top quark and a Z boson in pp collisions at $\sqrt{s} = 13$ TeV”, *Phys. Lett.* **B779** (2018) 358–384, doi:10.1016/j.physletb.2018.02.025, `arXiv:1712.02825`.

[48] **ATLAS** Collaboration, “Measurement of the production cross-section of a single top quark in association with a Z boson in proton–proton collisions at 13 TeV with the ATLAS detector”, *Phys. Lett.* **B780** (2018) 557–577, doi:10.1016/j.physletb.2018.03.023, `arXiv:1710.03659`.

[49] A. Giammanco and R. Schwienhorst, “Single top-quark production at the Tevatron and the LHC”, *Rev. Mod. Phys.* **90** no. 3, (2018) 035001, doi:10.1103/RevModPhys.90.035001, `arXiv:1710.10699`.

[50] N. Kidonakis, “NNLL resummation for s-channel single top quark production”, *Phys. Rev.* **D81** (2010) 054028, doi:10.1103/PhysRevD.81.054028, `arXiv:1001.5034`.

[51] N. Kidonakis, “Two-loop soft anomalous dimensions for single top quark associated production with a W^- or H^-”, *Phys. Rev.* **D82** (2010) 054018, doi:10.1103/PhysRevD.82.054018, `arXiv:1005.4451`.

[52] N. Kidonakis, “Next-to-next-to-leading-order collinear and soft gluon corrections for t-channel single top quark production”, *Phys. Rev.* **D83** (2011) 091503, doi:10.1103/PhysRevD.83.091503, `arXiv:1103.2792`.

[53] J. Alwall, R. Frederix, S. Frixione, V. Hirschi, F. Maltoni, O. Mattelaer, H. S. Shao, T. Stelzer, P. Torrielli, and M. Zaro, “The automated computation of tree-level and next-to-leading order differential cross sections, and their matching to parton shower simulations”, *JHEP* **07** (2014) 079, doi:10.1007/JHEP07(2014)079, `arXiv:1405.0301`.

[54] `https://twiki.cern.ch/twiki/bin/view/LHCPhysics/SingleTopRefXsec` [accessed: 2018-11-29].

[55] M. Aliev, H. Lacker, U. Langenfeld, S. Moch, P. Uwer, and M. Wiedermann, “HATHOR: HAdronic Top and Heavy quarks crOss section calculatoR”, *Comput. Phys. Commun.* **182** (2011) 1034–1046, doi:10.1016/j.cpc.2010.12.040, `arXiv:1007.1327`.

[56] P. Kant, O. M. Kind, T. Kintscher, T. Lohse, T. Martini, S. Mölbitz, P. Rieck, and P. Uwer, “HATHOR for single top-quark production: Updated predictions and uncertainty estimates for single top-quark production in hadronic collisions”, *Comput. Phys. Commun.* **191** (2015) 74–89, doi:10.1016/j.cpc.2015.02.001, `arXiv:1406.4403`.

[57] N. Kidonakis, "Top Quark Production", in *Proceedings, Helmholtz International Summer School on Physics of Heavy Quarks and Hadrons (HQ 2013): JINR, Dubna, Russia, July 15-28, 2013*, pp. 139–168. 2014. `arXiv:1311.0283`.

[58] S. Röcker, *Differential measurements of the single top quark cross section in the t-channel with the CMS experiment at $\sqrt{s} = 8$ TeV*. PhD thesis, KIT, 2015. `https://ekp-invenio.physik.uni-karlsruhe.de/record/48723`.

[59] **CMS** Collaboration, "Observation of the associated production of a single top quark and a W boson in pp collisions at $\sqrt{s} = 8$ TeV", *Phys. Rev. Lett.* **112** no. 23, (2014) 231802, doi:10.1103/PhysRevLett.112.231802, `arXiv:1401.2942`.

[60] C. D. White, S. Frixione, E. Laenen, and F. Maltoni, "Isolating Wt production at the LHC", *JHEP* **11** (2009) 074, doi:10.1088/1126-6708/2009/11/074, `arXiv:0908.0631`.

[61] M. Jezabek and J. H. Kuhn, "QCD Corrections to Semileptonic Decays of Heavy Quarks", *Nucl. Phys.* **B314** (1989) 1–6, doi:10.1016/0550-3213(89)90108-9.

[62] `https://commons.wikimedia.org/wiki/File:Ttbar_decay_channels.png` [accessed: 2018-10-05].

[63] **ATLAS, CDF, CMS, D0, LHCb** Collaboration, "Top-quark production measurements", in *Proceedings, 27th International Symposium on Lepton Photon Interactions at High Energy (LP15): Ljubljana, Slovenia, August 17-22, 2015*, SISSA. SISSA, 2016. `arXiv:1511.04200`.

[64] **CMS** Collaboration, "Single top t-channel differential cross section at 8 TeV", Tech. Rep. CMS-PAS-TOP-14-004, CERN, Geneva, 2014. `https://cds.cern.ch/record/1956681`.

[65] **CMS** Collaboration, "Measurement of the differential cross section for t-channel single-top-quark production at $\sqrt{s} = 13$ TeV", Tech. Rep. CMS-PAS-TOP-16-004, CERN, Geneva, 2016. `https://cds.cern.ch/record/2151074`.

[66] **ATLAS** Collaboration, "Fiducial, total and differential cross-section measurements of t-channel single top-quark production in pp collisions at 8 TeV using data collected by the ATLAS detector", *Eur. Phys. J.* **C77** no. 8, (2017) 531, doi:10.1140/epjc/s10052-017-5061-9, `arXiv:1702.02859`.

[67] **ATLAS** Collaboration, "Measurement of differential cross-sections of a single top quark produced in association with a W boson at $\sqrt{s} = 13$ TeV with ATLAS", *Eur. Phys. J.* **C78** no. 3, (2018) 186, doi:10.1140/epjc/s10052-018-5649-8, `arXiv:1712.01602`.

[68] **ATLAS** Collaboration, "Measurements of $t\bar{t}$ differential cross-sections of highly boosted top quarks decaying to all-hadronic final states in pp collisions at $\sqrt{s} = 13$ TeV using the ATLAS detector", *Phys. Rev.* **D98** no. 1, (2018) 012003, doi:10.1103/PhysRevD.98.012003, arXiv:1801.02052.

[69] M. Dobbs and J. B. Hansen, "The HepMC C++ Monte Carlo event record for High Energy Physics", *Comput. Phys. Commun.* **134** (2001) 41–46, doi:10.1016/S0010-4655(00)00189-2.

[70] P. Nason, "A New method for combining NLO QCD with shower Monte Carlo algorithms", *JHEP* **11** (2004) 040, doi:10.1088/1126-6708/2004/11/040, arXiv:hep-ph/0409146.

[71] S. Frixione, P. Nason, and C. Oleari, "Matching NLO QCD computations with Parton Shower simulations: the POWHEG method", *JHEP* **11** (2007) 070, doi:10.1088/1126-6708/2007/11/070, arXiv:0709.2092.

[72] S. Frixione, P. Nason, and G. Ridolfi, "A Positive-weight next-to-leading-order Monte Carlo for heavy flavour hadroproduction", *JHEP* **09** (2007) 126, doi:10.1088/1126-6708/2007/09/126, arXiv:0707.3088.

[73] E. Re, "Single-top Wt-channel production matched with parton showers using the POWHEG method", *Eur. Phys. J.* **C71** (2011) 1547, doi:10.1140/epjc/s10052-011-1547-z, arXiv:1009.2450.

[74] S. Alioli, P. Nason, C. Oleari, and E. Re, "A general framework for implementing NLO calculations in shower Monte Carlo programs: the POWHEG BOX", *JHEP* **06** (2010) 043, doi:10.1007/JHEP06(2010)043, arXiv:1002.2581.

[75] J. Alwall, M. Herquet, F. Maltoni, O. Mattelaer, and T. Stelzer, "MadGraph 5: Going Beyond", *JHEP* **06** (2011) 128, doi:10.1007/JHEP06(2011)128, arXiv:1106.0522.

[76] T. Sjöstrand, S. Ask, J. R. Christiansen, R. Corke, N. Desai, P. Ilten, S. Mrenna, S. Prestel, C. O. Rasmussen, and P. Z. Skands, "An Introduction to PYTHIA 8.2", *Comput. Phys. Commun.* **191** (2015) 159–177, doi:10.1016/j.cpc.2015.01.024, arXiv:1410.3012.

[77] B. Andersson, G. Gustafson, G. Ingelman, and T. Sjostrand, "Parton Fragmentation and String Dynamics", *Phys. Rept.* **97** (1983) 31–145, doi:10.1016/0370-1573(83)90080-7.

[78] **GEANT4** Collaboration, "GEANT4 – A Simulation Toolkit", *Nuclear Instruments and Methods in Physics Research Section A: Accelerators, Spectrometers, Detectors and Associated Equipment* **506** no. 3, (2003) 250–303, doi:10.1016/S0168-9002(03)01368-8.

[79] L. Evans and P. Bryant, "LHC Machine", *JINST* **3** (2008) S08001, doi:10.1088/1748-0221/3/08/S08001.

[80] **ATLAS** Collaboration, "The ATLAS Experiment at the CERN Large Hadron Collider", *JINST* **3** (2008) S08003, doi:10.1088/1748-0221/3/08/S08003.

[81] **CMS** Collaboration, "The CMS Experiment at the CERN LHC", *JINST* **3** (2008) S08004, doi:10.1088/1748-0221/3/08/S08004.

[82] **LHCb** Collaboration, "The LHCb Detector at the LHC", *JINST* **3** (2008) S08005, doi:10.1088/1748-0221/3/08/S08005.

[83] **ALICE** Collaboration, "The ALICE experiment at the CERN LHC", *JINST* **3** (2008) S08002, doi:10.1088/1748-0221/3/08/S08002.

[84] **LHCf** Collaboration, "The LHCf detector at the CERN Large Hadron Collider", *JINST* **3** (2008) S08006, doi:10.1088/1748-0221/3/08/S08006.

[85] **TOTEM** Collaboration, "The TOTEM experiment at the CERN Large Hadron Collider", *JINST* **3** (2008) S08007, doi:10.1088/1748-0221/3/08/S08007.

[86] **MoEDAL** Collaboration, "The MoEDAL experiment at the LHC: status and results", *J. Phys. Conf. Ser.* **873** no. 1, (2017) 012010, doi:10.1088/1742-6596/873/1/012010, `arXiv:1703.07141`.

[87] B. Schmidt, "The High-Luminosity upgrade of the LHC: Physics and Technology Challenges for the Accelerator and the Experiments", *Journal of Physics: Conference Series* **706** no. 2, (2016) 022002. `http://stacks.iop.org/1742-6596/706/i=2/a=022002`.

[88] J. Gruschke, *Observation of Top Quarks and First Measurement of the* $t\bar{t}$ *Production Cross Section at a Centre-Of-Mass Energy of 7 TeV with the CMS Experiment at the LHC*. PhD thesis, KIT, Karlsruhe, EKP, 2011. `http://inspirehep.net/record/914710/files/CERN-THESIS-2011-030.pdf`.

[89] S. Myers, *The LEP Collider, from design to approval and commissioning*. John Adams' Lecture. CERN, Geneva, 1991. `https://cds.cern.ch/record/226776`. Delivered at CERN, 26 Nov 1990.

[90] **CMS** Collaboration, "Absolute Calibration of Luminosity Measurement at CMS: Summer 2011 Update",.

[91] `https://twiki.cern.ch/twiki/bin/view/CMSPublic/LumiPublicResults` [accessed: 2018-11-13].

[92] T. Sakuma and T. McCauley, "Detector and Event Visualization with SketchUp at the CMS Experiment", *J. Phys. Conf. Ser.* **513** (2014) 022032, doi:10.1088/1742-6596/513/2/022032, `arXiv:1311.4942`.

[93] **CMS** Collaboration, "CMS Physics: Technical Design Report Volume 1: Detector Performance and Software",.

[94] **CMS** Collaboration, "Description and performance of track and primary-vertex reconstruction with the CMS tracker", *JINST* **9** no. 10, (2014) P10009, doi:10.1088/1748-0221/9/10/P10009, `arXiv:1405.6569`.

[95] P. Adzic *et al.*, "Energy resolution of the barrel of the CMS electromagnetic calorimeter", *JINST* **2** (2007) P04004, doi:10.1088/1748-0221/2/04/P04004.

[96] **CMS** Collaboration, "Energy Calibration and Resolution of the CMS Electromagnetic Calorimeter in pp Collisions at $\sqrt{s} = 7$ TeV", *JINST* **8** (2013) P09009, doi:10.1088/1748-0221/8/09/P09009, `arXiv:1306.2016`. [JINST8,9009(2013)].

[97] **CMS** Collaboration, "Performance of the CMS Hadron Calorimeter with Cosmic Ray Muons and LHC Beam Data", *JINST* **5** (2010) T03012, doi:10.1088/1748-0221/5/03/T03012, `arXiv:0911.4991`.

[98] **CMS** Collaboration, "Design, performance, and calibration of CMS hadron-barrel calorimeter wedges", *Eur. Phys. J.* **C55** no. 1, (2008) 159–171, doi:10.1140/epjc/s10052-008-0573-y.

[99] **CMS** Collaboration, "The performance of the CMS muon detector in proton-proton collisions at sqrt(s) = 7 TeV at the LHC", *JINST* **8** (2013) P11002, doi:10.1088/1748-0221/8/11/P11002, `arXiv:1306.6905`.

[100] **CMS** Collaboration, "Particle-flow reconstruction and global event description with the CMS detector", *JINST* **12** no. 10, (2017) P10003, doi:10.1088/1748-0221/12/10/P10003, `arXiv:1706.04965`.

[101] `https://github.com/cms-sw/cmssw` [accessed: 2018-10-24].

[102] `https://twiki.cern.ch/twiki/bin/view/CMSPublic/PhysicsResultsTOPEventDisplays` [accessed: 2018-10-17].

[103] `https://twiki.cern.ch/twiki/bin/viewauth/CMS/SWGuideMuonIdRun2` [accessed: 2018-10-22].

[104] **CMS** Collaboration, "Performance of the CMS muon detector and muon reconstruction with proton-proton collisions at $\sqrt{s} = 13$ TeV", *JINST* **13** no. 06, (2018) P06015, doi:10.1088/1748-0221/13/06/P06015, `arXiv:1804.04528`.

[105] https://twiki.cern.ch/twiki/bin/view/CMS/CutBasedElectronIdentificationRun2 [accessed: 2018-10-24].

[106] S. Catani, Y. L. Dokshitzer, M. H. Seymour, and B. R. Webber, "Longitudinally invariant k_T clustering algorithms for hadron-hadron collisions", *Nucl. Phys.* **B406** (1993) 187–224, doi:10.1016/0550-3213(93)90166-M.

[107] S. D. Ellis and D. E. Soper, "Successive combination jet algorithm for hadron collisions", *Phys. Rev.* **D48** (1993) 3160–3166, doi:10.1103/PhysRevD.48.3160, arXiv:hep-ph/9305266.

[108] Y. L. Dokshitzer, G. D. Leder, S. Moretti, and B. R. Webber, "Better jet clustering algorithms", *JHEP* **08** (1997) 001, doi:10.1088/1126-6708/1997/08/001, arXiv:hep-ph/9707323.

[109] M. Cacciari, G. P. Salam, and G. Soyez, "The anti-k_T jet clustering algorithm", *JHEP* **04** (2008) 063, doi:10.1088/1126-6708/2008/04/063, arXiv:0802.1189.

[110] https://twiki.cern.ch/twiki/bin/view/CMS/JetID13TeVRun2016 [accessed: 2018-11-28].

[111] T. Lapsien, R. Kogler, and J. Haller, "A new tagger for hadronically decaying heavy particles at the LHC", *Eur. Phys. J.* **C76** no. 11, (2016) 600, doi:10.1140/epjc/s10052-016-4443-8, arXiv:1606.04961.

[112] D. Bertolini, P. Harris, M. Low, and N. Tran, "Pileup Per Particle Identification", *JHEP* **10** (2014) 059, doi:10.1007/JHEP10(2014)059, arXiv:1407.6013.

[113] **ATLAS** Collaboration, "b-tagging in dense environments", Tech. Rep. ATL-PHYS-PUB-2014-014, CERN, Geneva, Aug, 2014. https://cds.cern.ch/record/1750682.

[114] **CMS** Collaboration, "Identification of b-quark jets with the CMS experiment", *JINST* **8** (2013) P04013, doi:10.1088/1748-0221/8/04/P04013, arXiv:1211.4462.

[115] **CMS** Collaboration, "Identification of b-quark jets at the CMS experiment in the LHC Run 2", Tech. Rep. CMS-PAS-BTV-15-001, CERN, Geneva, 2016. http://cds.cern.ch/record/2138504.

[116] https://twiki.cern.ch/twiki/bin/viewauth/CMS/BtagRecommendation [accessed: 2018-11-28].

[117] **CMS** Collaboration, "Determination of jet energy calibration and transverse momentum resolution in CMS", *Journal of Instrumentation* **6** no. 11, (2011) P11002. http://stacks.iop.org/1748-0221/6/i=11/a=P11002.

[118] **CMS** Collaboration, “Performance of missing transverse momentum in pp collisions at sqrt(s)=13 TeV using the CMS detector”, Tech. Rep. CMS-PAS-JME-17-001, CERN, Geneva, 2018. `http://cds.cern.ch/record/2628600`.

[119] A. Fröhlich, “Search for a Singly Produced Excited Bottom Quark Decaying to a Top Quark and W Boson at $\sqrt{s} = 13$ TeV with the CMS Experiment”, Master’s thesis, Universität Hamburg, 2017.

[120] **CMS** Collaboration, “Measurement of the differential cross section for $\mathrm{t\bar{t}}$ production in the dilepton final state at $\sqrt{s} = 13$ TeV”, Tech. Rep. CMS-PAS-TOP-16-011, CERN, Geneva, 2016. `https://cds.cern.ch/record/2140061`.

[121] **CMS** Collaboration, “Measurement of differential cross sections for top quark pair production using the lepton+jets final state in proton-proton collisions at 13 TeV”, *Phys. Rev.* **D95** no. 9, (2017) 092001, doi:10.1103/PhysRevD.95.092001, `arXiv:1610.04191`.

[122] **CMS** Collaboration, “Measurement of the differential cross section for top-quark-pair production in the dilepton channel at $\sqrt{s} = 13$ TeV with the CMS detector”, in *Proceedings, 9th International Workshop on Top Quark Physics (TOP 2016): Olomouc, Czech Republic, September 19-23, 2016*. 2016. `arXiv:1611.09657`.

[123] `https://twiki.cern.ch/twiki/bin/view/CMSPublic/PhysicsResultsTOPSummaryFigures` [accessed: 2018-12-08].

[124] J. Thaler and K. Van Tilburg, “Identifying Boosted Objects with N-subjettiness”, *JHEP* **03** (2011) 015, doi:10.1007/JHEP03(2011)015, `arXiv:1011.2268`.

[125] B. P. Roe, H.-J. Yang, J. Zhu, Y. Liu, I. Stancu, and G. McGregor, “Boosted decision trees, an alternative to artificial neural networks”, *Nucl. Instrum. Meth.* **A543** no. 2-3, (2005) 577–584, doi:10.1016/j.nima.2004.12.018, `arXiv:physics/0408124`.

[126] A. Hoecker, P. Speckmayer, J. Stelzer, J. Therhaag, E. von Toerne, and H. Voss, “TMVA: Toolkit for Multivariate Data Analysis”, *PoS* **ACAT** (2007) 040, `arXiv:physics/0703039`.

[127] F. E. James, *Statistical Methods in Experimental Physics; 2nd ed.* World Scientific, Singapore, 2006. `https://cds.cern.ch/record/1019859`.

[128] `https://root.cern.ch/download/doc/tmva/TMVAUsersGuide.pdf` [accessed: 2018-12-11].

[129] **CMS** Collaboration, “Measurement of the jet mass in highly boosted $\mathrm{t\bar{t}}$ events from pp collisions at $\sqrt{s} = 8$ TeV”, *Eur. Phys. J.* **C77** no. 7, (2017) 467, doi:10.1140/epjc/s10052-017-5030-3, `arXiv:1703.06330`.

[130] **CMS** Collaboration, “CMS Luminosity Measurements for the 2016 Data Taking Period”, Tech. Rep. CMS-PAS-LUM-17-001, CERN, Geneva, 2017. https://cds.cern.ch/record/2257069.

[131] **CMS** Collaboration, “Measurement of the inclusive cross section of single top quark production in the t channel at $\sqrt{s} = 13$ TeV”, Tech. Rep. CMS-PAS-TOP-16-003, CERN, Geneva, 2016. http://cds.cern.ch/record/2141577.

[132] **CMS** Collaboration, “Measurement of inclusive W and Z boson production cross sections in pp collisions at $\sqrt{s} = 13$ TeV”, Tech. Rep. CMS-PAS-SMP-15-004, CERN, Geneva, 2015. https://cds.cern.ch/record/2093537.

[133] **CMS** Collaboration, “Measurement of the ZZ production cross section and $Z \to \ell\ell\ell'\ell'$ branching fraction in pp collisions at $\sqrt{s} = 13$ TeV”, Tech. Rep. CMS-PAS-SMP-16-001, CERN, Geneva, 2016. https://cds.cern.ch/record/2148595.

[134] **CMS** Collaboration, “Measurement of the WZ production cross section in pp collisions at sqrt(s) = 13 TeV”, Tech. Rep. CMS-PAS-SMP-16-002, CERN, Geneva, 2016. http://cds.cern.ch/record/2144880.

[135] **CMS** Collaboration, “Measurement of the WW cross section pp collisions at sqrt(s)=13 TeV”, Tech. Rep. CMS-PAS-SMP-16-006, CERN, Geneva, 2016. https://cds.cern.ch/record/2160868.

[136] D. Nowatschin, *Search for vector-like quarks using jet substructure techniques with the CMS experiment*. PhD thesis, Universität Hamburg, Hamburg, 2017. http://bib-pubdb1.desy.de/record/330925.

[137] T. Müller, J. Ott, and J. Wagner-Kuhr, *theta – a framework for template-based modeling and inference*. http://www-ekp.physik.uni-karlsruhe.de/~ott/theta/theta.pdf.

[138] R. Barlow and C. Beeston, “Fitting using finite Monte Carlo samples”, *Comput. Phys. Commun.* **77** no. MAN-HEP-93-1. 2, (Jun, 1993) 219–228. https://cds.cern.ch/record/249779.

[139] J. S. Conway, “Incorporating Nuisance Parameters in Likelihoods for Multisource Spectra”, in *Proceedings, PHYSTAT 2011 Workshop on Statistical Issues Related to Discovery Claims in Search Experiments and Unfolding, CERN,Geneva, Switzerland 17-20 January 2011*, pp. 115–120. 2011. arXiv:1103.0354.

[140] V. Blobel, “An Unfolding method for high-energy physics experiments”, in *Advanced Statistical Techniques in Particle Physics. Proceedings, Conference, Durham, UK,*

March 18-22, 2002, pp. 258–267. 2002. arXiv:hep-ex/0208022. http://www.ippp.dur.ac.uk/Workshops/02/statistics/proceedings//blobel2.pdf.

Danksagung

[redacted]

[redacted]

[redacted]

[redacted]

[redacted]

[redacted]

[redacted]

[redacted]

[redacted]

Eidesstattliche Erklärung

Ich versichere, dass ich die beigefügte schriftliche Masterarbeit selbstständig angefertigt und keine anderen als die angegebenen Hilfsmittel benutzt habe. Alle Stellen, die dem Wortlaut oder dem Sinn nach anderen Werken entnommen sind, habe ich in jedem einzelnen Fall unter genauer Angabe der Quelle deutlich als Entlehnung kenntlich gemacht. Dies gilt auch für alle Informationen, die dem Internet oder anderer elektronischer Datensammlungen entnommen wurden. Ich erkläre ferner, dass die von mir angefertigte Masterarbeit in gleicher oder ähnlicher Fassung noch nicht Bestandteil einer Studien- oder Prüfungsleistung im Rahmen meines Studiums war. Die von mir eingereichte schriftliche Fassung entspricht jener auf dem elektronischen Speichermedium.

Ich bin damit einverstanden, dass die Masterarbeit veröffentlicht wird.

Ort, Datum	gez. Christopher Matthies